Model-Based Analysis of Cerebrovascular Diseases Combining 3D and 4D MRA Datasets

Kumulative Dissertation

zur Erlangung des akademischen Grades

Dr. rer. nat.

an der Fakultät für Mathematik, Informatik und Naturwissenschaften

der Universität Hamburg

eingereicht beim Fach-Promotionsausschuss Informatik von

Nils Daniel Forkert

aus Hamburg

Hamburg, 2012

Gutachter:
Prof. Dietmar Möller, Universität Hamburg
Prof. Heinz Handels, Universität zu Lübeck
Prof. Rolf-Rainer Grigat, Technische Universität Hamburg-Harburg
Prof. Stephan Olbrich, Universität Hamburg

Tag der Disputation: 16. April 2013

Abstract

Detailed knowledge about the vascular anatomy and blood flow at a macro- and microvascular level is often required for diagnosis, therapy decision, and intervention in case of cerebrovascular diseases. This knowledge can be obtained from high resolution 3D and time-resolved magnetic resonance imaging datasets. However, advanced computer-assisted image analysis methods are needed for an improved and faster diagnosis of patients with a cerebrovascular disease, due to the massive amount of acquired data. From a methodical perspective, an automatic cerebrovascular segmentation, hemodynamic analysis, and combined visualization of vascular structures together with the corresponding hemodynamic situation is required.

The multi-step segmentation framework presented in this work was developed to enable a sufficient delineation of all vessels, including small and malformed vessels, from high resolution 3D angiographies. The purpose of the first step of this segmentation framework is to extract the brain tissue using a graph-based approach to prevent leakage of the segmentation into non-brain tissue in the subsequent processing steps. After this, a non-linear combination of intensity and shape information using fuzzy logic is performed, in which the shape information is obtained from the vesselness filter. The resulting parameter image is then used for an automatic extraction of the cerebrovascular system employing a level-set segmentation approach with anisotropic energy weights. Finally, gaps in the resulting cerebrovascular segmentation are reduced applying a shortest path algorithm. The automatically segmented vessels can, for example, be used for a surface-based visualization, which enables an intuitive screening of the anatomy. However, this visualization includes no information about the blood flow. Therefore, time-resolved magnetic resonance angiographies have to be analyzed. The direct estimation of hemodynamic parameters from the corresponding concentration time curves is often imprecise. This drawback can be overcome using the developed reference-based linear curve fitting approach. Here, the main idea is to extract a patient-individual hemodynamic reference curve directly from the given time-resolved dataset. The extracted reference curve is fitted to each concentration time curve and then used for parameter estimation. Finally, a novel 4D blood flow visualization technique was developed, which enables a direct combined analysis and visualization of the cerebrovascular system and the corresponding blood flow situation. Therefore, the 3D and 4D MRA image sequences of a patient are registered such that the extracted hemodynamic information can be displayed dynamically over time on the vessel surface model.

An evaluation of the cerebrovascular segmentation framework using manual segmentations as ground truth showed that this approach is capable of segmenting small as well as malformed vessels with high precision within the range of inter-observer differences, and significantly better than typical state-of-art methods. Furthermore, a comparison to commonly applied hemodynamic models using Monte-Carlo simulations and clinical datasets revealed that the proposed reference-based linear curve fitting model leads to reduced errors regarding the time-to-peak parameter over a wide range of temporal resolutions. Finally, an evaluation of the 4D blood flow visualization using datasets of patients with arteriovenous malformations showed that this visualization leads to a feasible representation of the cerebrovascular anatomy and blood flow, which allows an intuitive and fast diagnosis.

The developed methods have been already successfully applied for several clinical studies in addition to the 4D blood flow visualization. Within this context, the hemodynamic situation in the presence of anatomical rupture risk factors of arteriovenous malformations was analyzed and a computer-aided segmentation and angiographic characterization of this vascular pathology was developed. Further examples for clinical applications described in the second part of this thesis comprise the improved measurement of aneurysms, quantitative analysis of aneurysm coil treatment stability, as well as tissue-at-risk quantification and identification of patients within 4.5 hours of symptom onset in case of an acute ischemic stroke.

In conclusion, the developed methods may help to improve the understanding, diagnosis, and treatment of cerebrovascular diseases.

Zusammenfassung

Zerebrovaskuläre Erkrankungen erfordern häufig ein genaues Verständnis der Gefäßanatomie und des Blutflusses auf makro- und mikrovaskulärer Ebene, um eine bestmögliche Diagnose, Therapieentscheidung und Intervention zu gewährleisten. Dieses Wissen kann aus hochaufgelösten 3D- und zeitaufgelösten Magnetresonanztomographie-Datensätzen gewonnen werden. Aufgrund der hiermit verbundenen Datenmenge sind jedoch computergestützte Methoden zur Analyse dieser Datensätze für eine optimale und schnelle Bewertung notwendig. Aus methodischer Sicht bedarf es hierfür insbesondere einer automatischen Gefäßsegmentierung, Analyse der Hämodynamik sowie kombinierten Darstellung von Anatomie und Hämodynamik.
Das in dieser Arbeit vorgestellte mehrstufige Segmentierungsverfahren wurde speziell entwickelt, um eine genaue Extraktion aller Blutgefäße, inklusive kleiner und pathologischer Gefäße, aus hochaufgelösten 3D Magnetresonanzangiographien zu ermöglichen. Hierzu wird zunächst das Gehirngewebe mittels eines graphenbasierten Ansatzes extrahiert, um so nachfolgende Übersegmentierungen von nicht-zerebralen Strukturen zu verhindern. Im zweiten Schritt werden Intensitäts- und Vesselness-Werte mittels Fuzzy-Logik kombiniert. Der Vesselness-Parameter quantifiziert dabei die lokale Ähnlichkeit zu einer tubulären Struktur. Der resultierende Fuzzy-Parameterdatensatz wird dann im dritten Schritt dafür verwendet die Gefäße mittels einer Level-Set-Methode mit anisotropen Energiegewichten zu segmentieren. Im letzten Schritt werden eventuell vorhandene Unterbrechungen in der Gefäßsegmentierung detektiert und korrigiert. Die automatisch segmentierten Blutgefäße können zum Beispiel für eine intuitive oberflächenbasierte 3D-Visualisierung verwendet werden, welche jedoch keine Information über den Blutfluss enthält. Daher müssen zusätzlich zeitaufgelöste Magnetresonanzangiographien analysiert werden. Die direkte Bestimmung von hämodynamischen Parametern auf Basis der korrespondierenden Kontrastmittelkurven ist häufig ungenau. Aus diesem Grund wurde im Rahmen dieser Arbeit das Modell der referenzbasierten Kurvenanpassung entwickelt. Die grundlegende Idee hierbei ist es, eine hämodynamische Referenzkurve direkt aus dem Datensatz zu extrahieren, die dann zur Kurvenanpassung und nachfolgender Parameterabschätzung verwendet wird. Abschließend wurde ein neuer Ansatz zur 4D-Blutflussvisualisierung entwickelt. Dazu wird die zeitaufgelöste auf die örtlich hochaufgelöste Magnetresonanzangiographie desselben Patienten registriert, sodass die extrahierte hämodynamische Information dynamisch auf dem Oberflächenmodell des Gefäßsystems dargestellt werden kann.
Die Evaluation des vorgestellten mehrstufigen Segmentierungsansatzes unter Verwendung von manuellen Segmentierungen zeigte, dass sowohl kleine als auch pathologische Gefäße mit hoher Präzision im Bereich der Inter-Observer-Variabilität segmentiert werden können, wobei die Segmentierungsergebnisse signifikant besser sind als bei Verwendung von bislang etablierten Methoden. Ein Vergleich mit gängigen hämodynamischen Modellen unter Verwendung von Monte-Carlo Simulationen und klinischen Datensätzen konnte nachweisen, dass die vorgestellte referenzbasierte Kurvenanpassung zu deutlich geringeren Fehlern bei der Time-to-Peak Abschätzung über einen großen Bereich von zeitlichen Auflösungen führt. Darüber hinaus konnte im Rahmen einer klinischen Evaluation nachgewiesen werden, dass die 4D-Blutflussvisualisierung eine zuverlässige kombinierte Darstellung von Anatomie und Hämodynamik erlaubt, welche intuitiv und schnell begutachtet werden kann.
Abgesehen von der 4D-Blutflussvisualisierung wurden die vorgestellten Methoden bereits für eine Vielzahl von klinischen Studien eingesetzt, welche im zweiten Teil dieser Arbeit vorgestellt werden. In diesem Rahmen wurde z.B. die Hämodynamik bei Vorliegen von Risikofaktoren für eine Ruptur von arteriovenösen Malformationen untersucht sowie eine computergestützte Methode zur Segmentierung und angiographischen Charakterisierung dieser Pathologie entwickelt. Weitere vorgestellte Anwendungsbeispiele umfassen eine verbesserte Vermessung von Aneurysmen und quantitative Bewertung von Aneurysma-Coil-Therapien sowie die Definition der Penumbra des ischämischen Schlaganfalls und Identifikation von Patienten mit ischämischem Schlaganfall, bei denen eine Thrombolysetherapie möglich ist.
Zusammenfassend zeigt sich, dass die vorgestellten Methoden zu einem genaueren Verständnis und einer verbesserten Therapie von zerebralen Gefäßerkrankungen führen können.

Contents

Chapter 1

Introduction

The cerebral stroke is a major cause for death and disability in the western hemisphere [Donnan et al., 2008]. It is estimated that cerebral strokes cause 10-12% of all deaths worldwide [Bonita, 1992]. Due to the aging population, the management of strokes will become even more important than today, especially since the total costs of strokes for health care systems already amount for 2-4% [Dewey et al., 2001].
Approximately 72% of all strokes are caused by an occlusion of an artery, which is commonly called an ischemic stroke. Such an occlusion leads to a partial or complete restriction of the cerebral perfusion in the brain tissue supplied by this artery and may ultimately result in an irreversible damage of the corresponding brain cells [Thrift et al., 2001].
Roughly 20% of cerebral strokes are caused by an acute bleeding due to a rupture of a blood vessel [Thrift et al., 2001]. Similar to ischemic strokes, an acute bleeding may also result in an irreversible damage of the corresponding brain cells. In most cases, these ruptures occur at weakened vessel walls that originate from cerebrovascular pathologies such as aneurysms or arteriovenous malformations. In contrast to the ischemic stroke, these so-called hemorrhagic strokes are rather a major cause for death and disability at younger ages.
In any case, detailed knowledge about the patient-individual anatomy of the cerebrovascular system and blood flow at a macrovascular level and/or microvascular perfusion situation is required to enable an optimal diagnosis, therapy decision, intervention, and follow-up examinations.
The development of magnetic resonance imaging (MRI) techniques made it possible to obtain the required knowledge. However, typical MRI examinations of cerebrovascular diseases may easily result in up to 2500 two-dimensional images, especially in case of time-resolved (4D) image acquisition, that have to be analyzed by the clinicians. Such an examination can be very time-consuming and also error-prone, which leads to the need of computer-assisted image analysis methods.

1.1 Objectives of this Work

The main aim of this work is to present computer-aided image analysis methods that can support the clinicians for rating MRI datasets of patients with cerebrovascular diseases. From a methodical perspective, there are three main objectives that are in the focus of this thesis:

1. the automatic segmentation of cerebrovascular structures from high resolution magnetic resonance angiography (MRA) datasets,
2. the automatic analysis of time-resolved MRA or perfusion MRI datasets, and
3. the combined analysis and visualization of 3D MRA with high spatial resolution and time-resolved MRA datasets.

The second part of this work will highlight possible applications of these methods for the clinical routine as well as research purposes. Within this context, selected applications of the cerebrovascular segmentation and hemodynamic/perfusion analysis methods will be described for the diagnosis and research of three cerebrovascular diseases:

1. arteriovenous malformations,
2. aneurysms, and
3. acute ischemic strokes.

1.2 Outline of this Work

This work is structured as follows:

The following second chapter gives a brief introduction to the main principles of magnetic resonance imaging. The image sequences used in this work are then described in the second part of the chapter. More precisely, 3D and 4D MRA, perfusion- and diffusion-weighted as well as quantitative T2 and FLAIR imaging techniques are described in more detail.

The third chapter illustrates the methodical contributions of this thesis. Within this context, a novel multi-step framework for the automatic segmentation of the cerebrovascular system is presented in the first part of the chapter. This approach consists of four steps. The first pre-processing step focusses on the removal of non-brain tissue from high-resolution magnetic resonance angiographies using a graph-based brain contour extraction method. The second step deals with the combination of intensity and shape information using fuzzy logic to enhance vascular structures. This information is then used in the third step within a level-set approach with anisotropic energy weights for the automatic segmentation of cerebrovascular structures. The last step of the proposed

cerebrovascular segmentation framework aims at detecting and correcting gaps within the extracted segmentation using a shortest path algorithm and following expansion to the vessel boundaries using a level-set approach.
The focus of the second part of the chapter is the analysis of time-resolved MRA and perfusion-weighted MRI datasets. Within this context, a new method for determining the bolus arrival time of concentration time curves derived from 4D MRA or perfusion-weighted MRI datasets is presented. Afterwards, the proposed hemodynamic model is evaluated in more detail with a particular focus on determining reasonable temporal resolutions for the acquisition of time-resolved MRA datasets of different vessel structures. The last part of the chapter presents a novel method for combining 3D and 4D MRA image sequences within one intuitive 4D visualization. Finally, a study comparing the developed 4D blood flow visualization to state-of-the-art digital subtraction angiographies using 31 clinical datasets of patients with an arteriovenous malformation is presented.

The fourth chapter presents possible applications of the methods described in the third chapter for the image-based analysis of cerebrovascular diseases for clinical as well as research purposes. The first part of the chapter focusses on the relation of parameters extracted from 3D and 4D MRA image sequences to established anatomical risk factors for a rupture of arteriovenous malformations. After this, a study analyzing the steal effect, which is often associated with arteriovenous malformations, is presented. Moreover, a method for the automatic analysis of this vascular pathology, including the automatic segmentation of the nidus and identification of the corresponding feeding arteries and draining veins, is described.
The second section of the chapter describes possible applications of the cerebrovascular segmentation for the diagnosis and therapy of aneurysms. More precisely, a 3D computer-aided technique for measuring important aneurysm diameters is presented and evaluated. Furthermore, a method for quantitatively determining recurrence volumes after endovascular coiling of aneurysms by registration of longitudinal MRA datasets is presented and statistically evaluated.
The final section of the chapter highlights possible applications of the hemodynamic analysis method for the diagnosis of acute stroke patients. Within this context, a study investigating the impact of hemodynamic models on the definition of the perfusion deficit is presented. The second part of this section describes the so-called DWI-FLAIR mismatch concept, which can be used to identify acute ischemic stroke patients with unknown symptom onset, who are eligible for thrombolytic therapy. Based on this, a study investigating the relation of a positive DWI-FLAIR mismatch to the extent of the perfusion deficit is presented. Moreover, an analysis of the relation of quantitative T2 values to final infarction is described in the last part of the chapter.

Finally, an outlook regarding future work and a summary is given in the last two chapters of this thesis.

Chapter 2

Magnetic Resonance Imaging of Cerebrovascular Diseases

It was already in 1895 when Wilhelm Conrad Röntgen discovered electromagnetic waves (X-rays) with a very short wavelength, which have the ability to pass through human tissue. X-ray imaging makes use of the fact that the density properties of different tissues lead to different extents of photon attenuation as they pass through the human body. Thus, with the discovery of X-rays it became possible for the first time to visualize internal structures of the human body without the need of an open surgery.
After the discovery of X-rays, scientists all around the world started experimenting with this new radiation, which led to a rapid development of medical imaging devices. However, imaging techniques based on X-rays are associated with several drawbacks such as the exposure to ionizing radiation, which leads to an increased risk for cancer. Furthermore, despite the development of improved detector devices, the ability of these imaging devices to display soft tissues with high contrast is still limited.
These drawbacks can be overcome by magnetic resonance imaging (MRI), which utilizes the nuclear magnetic resonance (NMR) for acquisition of images. Although the nuclear magnetic resonance was already discovered in 1946 independently by Felix Bloch and Edward Purchell, it was not until 1973 when Paul Lauterbur succeeded in employing this discovery for the acquisition of a two-dimensional image of a water filled object. After this, MRI began to develop rapidly. At present, MRI is an integral imaging device without which today's clinical diagnostics would be unimaginable.
The first part of this chapter will give a brief introduction to the most important principles of magnetic resonance imaging. The MRI sequences used in this work will be described in the second part of this chapter. It should be highlighted that this chapter is only supposed to give a brief introduction to MRI and description of the image sequences used in this work. For more detailed descriptions, the interested reader may, for example, refer to standard reference works like "Magnetic Resonance Imaging" by Vlaardingerborek and den Boer [Vlaardingerbroek and Boer, 2010], which has also been used as the basis for the descriptions in this chapter, if not noted otherwise.

2.1 Basics of Magnetic Resonance Imaging

Magnetic resonance imaging is capable of acquiring tomograms of the human body. In contrast to imaging techniques that employ X-rays, MRI does not utilize ionizing radiation for image acquisition but very strong static magnetic fields together with high-frequency radio waves. Here, magnetic field strengths up to 3 Tesla (T) are approved for clinical settings. However, MRI scanners with stronger magnetic fields are also available for research settings.

2.1.1 Spin and Precession

Subatomic particles such as protons and neutrons possess a spin around their axis. Unpaired particles have a spin of 1/2, whereas the occurrence of particles exhibiting spins with opposite direction lead to the elimination of the net spin. Therefore, only nuclei that contain an uneven number of protons and/or neutrons are of use for MRI measurements. This intrinsic spin property is associated with a magnetic dipole moment causing the nucleus to behave like a very small magnet. Therefore, when placed in a magnetic field, the spins align themself in the corresponding direction of the magnetic field with a characteristic motion, which is called precession. This precession takes place with a characteristic angular frequency, which is called Larmor frequency ω. The Larmor frequency depends on the magnetic field strength B_0 and nuclei specific properties γ (the gyromagnetic ratio):

$$\omega = \gamma B_0.$$

The gyromagnetic ratio of water, which is the most important atom for MRI measurements, is 42.58 MHz / T. Examples for other atoms that are also used for MRI measurements are ^{13}C ($\gamma = 10.71$/T), ^{23}Na ($\gamma = 11.26$/T), ^{31}P ($\gamma = 17.24$/T) and ^{19}F ($\gamma = 40.05$/T). Since the human body consists of 70% water [Handels, 2009], MRI is mostly performed using hydrogen protons.
Without application of an external magnetic field, the main axes of the nuclei are distributed uniformly in space. By applying an external magnetic field, the nuclei align in the direction of this field. More precisely, some nuclei align parallel with the magnetic field and some align against it. These two states are often called parallel (spin-up) and anti-parallel (spin-down) state. However, at room temperature nuclei occupying the lower energy spin-up state slightly outnumber those in the spin-down state. The difference in number of nuclei in the two states is very small and depends not only on the temperature but also on the strength of the magnetic field. For example, using a magnetic field strength of 1T, 1,000,007 nuclei are in the spin-up state while 1,000,000 nuclei are in the spin-down state [Löwenhardt, 2001]. Since nuclei with opposite spin direction eliminate themself with respect to a measureable longitudinal magnetization, only 7 out of 2,000,007 nuclei contribute to the MR signal at this setup. However, because of the enormous amount of water protons in the human body, this is still enough to obtain sufficient MR measurements. It should be mentioned that the difference between the spin-up and spin-down state is increasing with the strength of the external

magnetic field, which leads to an increasing number of spin-up states and, therefore, to an improved signal-to-noise ratio.
For obtaining a MR image of a given object, it is placed in an external magnetic field B_0. As mentioned earlier, this external magnetic field forces the nuclei to align with the magnetic field, which creates a net magnetic moment in the direction of the magnetic field, the so-called equilibrium magnetization M_0. This thermal equilibrium state can be disturbed by applying a radio frequency (RF) pulse with a frequency that is equal to ω of the nuclei of interest (resonance condition). Such a RF pulse is an oscillating magnetic field B_1 that rotates around the direction of B_0 at Larmor frequency. Technically, such a RF pulse is generated by a powerful radio transmitter that interacts with the patient by an antenna (the RF coil). The application of such a RF pulse leads to an absorption of the electromagnetic energy by the nuclei with a Larmor frequency that is equal to the frequency of the RF pulse, which causes the net magnetic moment M_0 to flip away from B_0. The flip angle α describes the angle between the rotated net magnetization and the main direction of the magnetic field. The extent of the flip angle depends on the duration of the RF pulse, whereas this change in the direction of M_0 is caused by the additional precession of the net magnetization around B_1.
Several RF pulses, which are sent repeatedly, are required for the acquisition of MR images, whereas the time between two RF pulses is commonly called repetition time (TR). After each RF pulse, the magnetization precesses around B_0, which generates a measurable signal with a frequency equal to ω. The time between the last RF pulse excitement and signal readout is commonly referred to as echo time (TE).

2.1.2 Gradients and k-space

Within a homogenous magnetic field, each nucleus possesses the same resonant frequency. Therefore, no spatial information is available to relate a measureable signal following an applied RF signal to a specific location. To obtain spatial knowledge about the location of RF signals, the resonant frequency needs to be spatially adapted. Technically, this can be realized by superimposing small, linearly increasing magnetic fields on the homogenous main magnetic field B_0. These so-called gradient fields render the possibility that the nuclei of interest can be locally excited using RF pulses with different corresponding Larmor frequencies. Therefore, three gradient coils are typically used, whereas each coil encodes one of the three main spatial directions (x, y and z).
Using the example of a transversal image acquisition, the spatial encoding can be performed by first applying a linearly increasing gradient field in the patient's cranio-caudal direction, which corresponds to the direction of the main magnetic field, during the RF excitement (G_z-gradient). The application of the G_z-gradient leads to different Larmor frequencies in each slice, which can therefore be excited separately using corresponding RF pulses. However, no spatial information about the x- or y-coordinate of a measured signal is available at this point. This problem can be solved in terms of phase and frequency discrimination. The phase encoding can be realized by applying a second gradient field between RF excitement and signal readout (e.g. G_y-gradient). As a result, the spins begin to precess at different Larmor frequencies along the corresponding gradient

direction and obtain a distinct phase value. In analogy to this, the frequency encoding can be achieved by applying a third gradient field during the signal readout (e.g. G_x-gradient), which is perpendicular to the gradient used for phase encoding. Thus, the spins exhibit a unique precession frequency based on their spatial location that can be measured.
The measurement of a 2D slice corresponds to the 2D Fourier-transformed function of the corresponding image in the spatial domain. The raw data obtained by the MR measurements are recorded in a matrix, which is called k-space. Each row of the k-space corresponds to one phase discrimination and each column corresponds to one frequency discrimination. The center of the k-space is mainly responsible for the coarse structure and contrast of the anatomical image. The outer parts of the k-space mainly contribute to the level of finer details and, therefore, to the spatial resolution. Finally, the k-space can be used to reconstruct the anatomical image in the spatial domain, for example, using a fast Fourier-transform.

2.1.3 T1 and T2 Relaxation

After the RF pulse is switched off, the magnetization precesses around B_0, which induces a current in a coil that can be amplified and measured. The strength of this MR signal is known to decrease with time as the magnetization returns to equilibrium (relaxation). This decrease can be ascribed to the fact that all spins precess in phase directly after the RF pulse and accumulate to a signal maximum. However, the spins loose their phase coherence over time due to two independent relaxation processes, which result in a decrease of the measured signal.
After the RF pulse is switched off, the spins relax back to the equilibrium magnetization. By returning to equilibrium, the previously absorbed energy is emitted as heat to the surrounding (spin-lattice interaction). This process is often called longitudinal relaxation or T1 relaxation. The T1 relaxation time is defined as the time that is required until 63.2% of the original longitudinal magnetization has recovered. The T1 relaxation time depends on the magnetic field strength and tissue properties like viscosity and temperature since small fast moving molecules exhibit a rather low probability for interaction.
The second process, which takes place after the RF pulse is switched off, is the so-called transversal relaxation or T2 relaxation. Due to the RF pulse, the spins originally precess in phase. However, interaction between close-by nuclei (spin-spin interaction) may result in a transfer of excitation energy between the nuclei, which leads to a dephasing. The T2 relaxation time is defined as the time that is required until 37% of the original transversal magnetization is reached again. The T2 relaxation time is always shorter than the corresponding T1 relaxation time of the same tissue. Furthermore, the T2 relaxation time measured is also shorter than what can be theoretically explained by the spin-spin relaxation. This observation can be explained by magnetic field inhomogeneities and different tissue properties, such as diffusion. The time effectively measured for the transversal relaxation is therefore called T2* relaxation time.
Variations of the TE, TR and flip angle parameter can be used to enhance one of the

relaxation contrasts (T1 or T2-weighted MRI). In general, a short TR leads to a strong T1 weighting while a long TR results in a low T1 weighting. In contrast to this, a short TE leads to a low T2 weighting while a long TE leads to a strong T2 weighting. A short TR requires smaller flip angles to prevent saturation effects.

2.2 MRI Sequences for Diagnosis of Cerebrovascular Diseases

2.2.1 Time-of-Flight Angiography

The time-of-flight (TOF) angiography is a frequently used magnetic resonance angiography (MRA) technique in the clinical routine to obtain knowledge about the individual cerebrovascular system [Suri et al., 2002a]. The TOF image sequence offers a good blood-to-background contrast such that it can be used for a detailed cerebrovascular segmentation (see section 3.1), which leads to benefits regarding the diagnosis of cerebrovascular diseases (see chapter 4).
The basic idea of the TOF image sequence is to achieve a steady-state magnetization saturation of the stationary tissue. Using this principle, unsaturated blood that flows into the imaging plane is displayed by high intensities while the saturated stationary tissue is represented by low intensities. The signals of at least ten RF pulses are rejected until a TOF image is measured to ensure that the stationary tissue has reached the steady-state.
TOF images can be acquired using three different techniques: sequential 2D slice, single slab and multi-slab acquisition [Davis et al., 1993]. The sequential 2D slice acquisition excites only one slice per image acquisition. This acquisition technique leads to the best blood-to-background contrast but is usually too time-consuming for clinical purposes. In contrast to this, the whole imaging volume is excited at once using the single slab technique. This technique is considerably faster than the sequential 2D slice acquisition but also results in a worse blood-to-background contrast. The multi-slab acquisition is a trade-off between the two aforementioned acquisition techniques. Using this technique, the whole imaging volume is separated into several blocks of thin 3D volumes that are called slabs. The main idea of this technique is to excite one slab per time. Since these blocks are smaller than the whole volume, this technique enables a reasonable blood-to-background contrast together with an acceptable acquisition time. However, slab-to-slab amplitude variations have to be expected with this technique since the slab excitation is never perfectly rectangular with infinitely steep slopes at the slab corners. Therefore, the single slabs are usually measured with an overlap of 20-30% [Kholmovski et al., 2002], which leads to an increase of the acquisition time and requirement of post-processing methods. Apart from the acquisition technique, the signal strength of the flowing blood depends on several variables such as the TR, the flip angle, the blood flow velocity as well as its direction. The highest signals can be obtained if the slabs are oriented perpendicular to the direction of the blood flow, which avoids that flowing blood becomes also saturated. However, this is obviously not the case for all vessels when imaging the

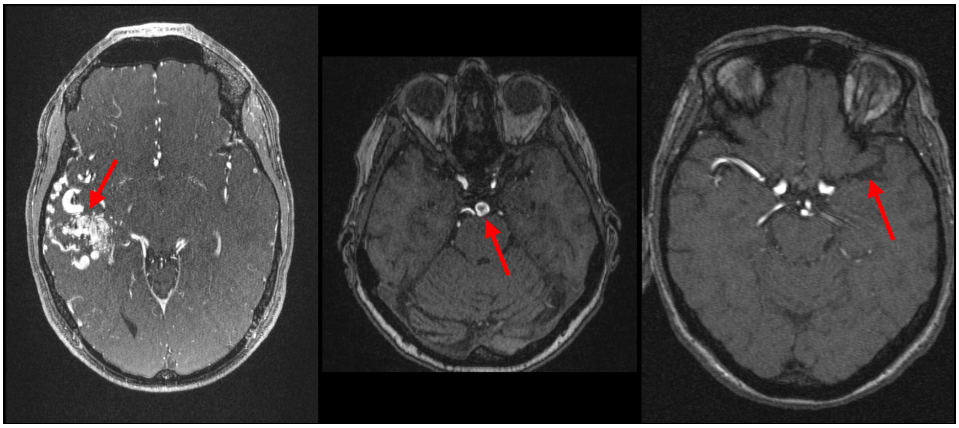

Figure 2.1: Selected slices from Time-of-Flight MRA datasets from patients with an arteriovenous malformation (left), an aneurysm (center), and an occluded artery (right).

whole brain. In general, TOF imaging can be performed with or without application of contrast agent. The application of contrast agent is in particular helpful in case all vessel structures, especially venous vessel, are of diagnostic interest. Nevertheless, turbulent flow may still cause a reduction or even an elimination of the MR signal.

2.2.2 Contrast-Enhanced Angiography

As mentioned in the last section, TOF imaging is sensitive to the direction of the blood flow as well as turbulent flow conditions. The application of contrast agent may reduce these artifacts to certain extents but will not eliminate them completely. This limitation is especially important in case of aneurysms with special flow conditions (concentric flow within the saccular bulges) that may be problematic for TOF image sequences (see Fig. 2.2). In such cases, the contrast-enhanced (CE) MR angiography may be one promising alternative for clinical purposes. A second benefit of the CE MRA is the acquisition time, which is considerably faster than that of the TOF MRA.
The CE MRA utilizes the shortening of the T1 relaxation time of blood after application of gadolinium-based contrast agents. In general, CE MRA acquisition techniques employ a T1 contrast enhancing gradient echo sequence. Due to the usage of contrast agent, the acquisition time of the CE MRA is limited by the time that is required for the first arterial contrast agent bolus passage, since venous vessels are not of interest for most diagnostic questions and may hinder an optimal diagnosis. Due to this temporal requirement, the best possible spatial resolution of the CE MRA is typically lower as compared to that of TOF image sequences. A second problem that arises from the usage of contrast agent is that it is important to know when to start the actual image acquisition. In general, the acquisition should start at the time when the contrast agent is reaching the volume of interest. This information can, for example, be obtained by applying a small contrast agent dose prior to the actual image acquisition. A fast dynamic single-slice scan can then be used to determine the time, which is required by the contrast agent to reach the volume of interest after its administration. In general, the contrast agent injection

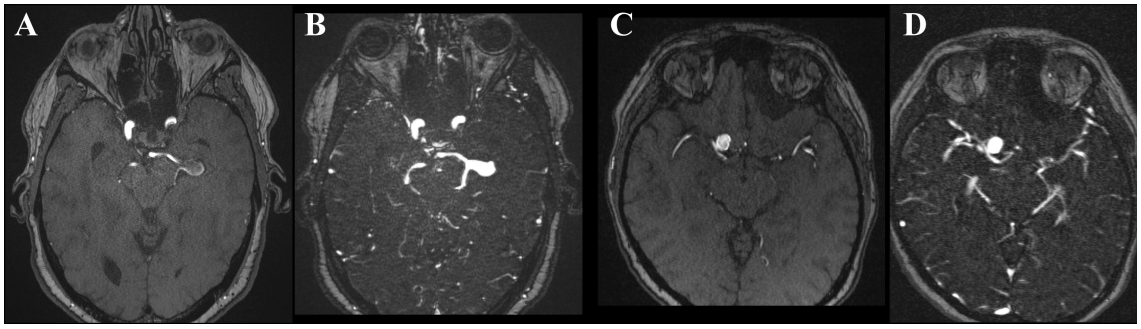

Figure 2.2: Two examples of corresponding slices from Time-of-Flight (A,C) and contrast-enhanced MRA datasets (B,D) from patients with an aneurysm.

time should be equal to the scanning time. Due to these reasons, the CE MRA image acquisition time is considerably shorter compared to the TOF MRA acquisition time, which may easily require up to 8 minutes depending on the imaging parameters and chosen spatial resolution. Apart from this, high flip angles $\alpha > 20°$ are typically used for the CE MRA to increase the blood-to-background contrast.

2.2.3 Time-Resolved Angiography

The two previously described MR angiography techniques have in common that a cerebrovascular system can be displayed with high spatial resolution, which enables an analysis of the angioarchitecture. Both techniques have also in common that no temporal information about the distribution of contrast agent, if given, is available in the resulting image sequences. However, this is also an important information for certain diagnostic questions, such as the definition of feeding arteries and draining veins of an arteriovenous malformation (see chapter 4.1.3).
Time-resolved MRA techniques require an acquisition of 3D datasets with high temporal and a reasonable spatial resolution. For this reason, one special focus in the beginning of the development of time-resolved MRA techniques was the improvement of the gradient coils to allow an acquisition with stronger gradients and faster switching times. However, further improvements of gradient coils are restricted by physical limitations. Therefore, other techniques were necessary to enable a reduction of the acquisition time such that a reasonable spatial and temporal resolution can be obtained.
Further improvements regarding this point were achieved by multi-channel coils that lead to the possibility of faster parallel imaging. The main idea of parallel imaging is to reduce the dataset in the phase encoding direction by combining the signal of multiple coils.
The breakthrough in time-resolved MRA imaging was accomplished by additionally applying principles of k-space sampling [Fink et al., 2005a, Fink et al., 2005b]. The main idea of the k-space sampling technique is to sample the center of the k-space, which mainly contributes to the image contrast, more often than the peripheral segments. The high frequency signals in the outer k-space are then interpolated. However, this leads

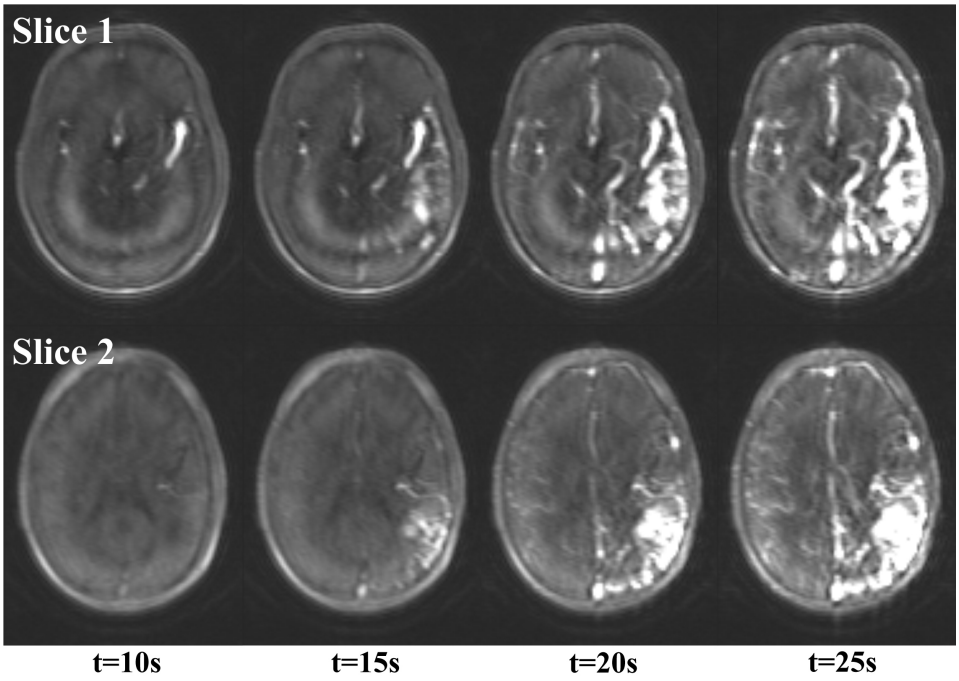

Figure 2.3: Two selected slices from a time-resolved MRA dataset at different time points from a patient with an arteriovenous malformation.

to the problem that typical time-resolved MRA datasets do not exhibit a high degree of anatomical detail. Typical time-resolved MRA techniques differ with respect to the implementation, e.g. number of k-space regions and sampling strategy.
The combination of improved gradients together with parallel imaging and k-space sampling techniques has led to a possible image acquisition with a sub-second temporal resolution and reasonable spatial resolution. Thus, an analysis of the contrast agent distribution over time becomes possible (see Fig. 2.3) using typical hemodynamic analysis methods as presented in section 3.2. Similar to the acquisition of CE MRA datasets, gadolinium based contrast agents are typically used for this purpose together with fast T1 contrast enhancing acquisition techniques such as FLASH (fast low angle shot magnetic resonance imaging).

2.2.4 Arterial Spin Labeling

Arterial spin labeling (ASL) techniques were originally developed as an alternative to perfusion-weighted MRI (see next section) for determining the cerebral blood flow [Yang, 2002]. The main benefit of these techniques is that no contrast agent is required for this purpose. However, these ASL principles were recently also applied for acquisition of time-resolved MRA image sequences without contrast agent.
The main idea of ASL imaging is to successively acquire two datasets. The first dataset is acquired after upstream (in the major arteries) selective inversion of the spins using RF pulses. The second dataset is then acquired without a previous inversion. All spins

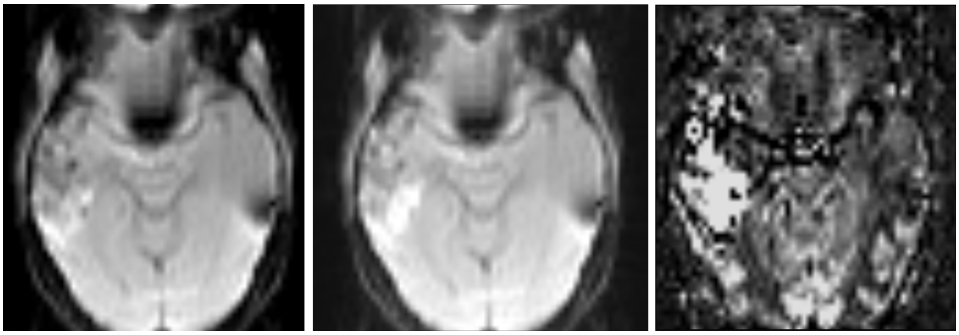

Figure 2.4: Selected slice from a pulsed arterial spin labeling dataset from a patient with an arteriovenous malformation: Control sequence acquired without inversion pulse (left), corresponding slice acquired after inversion pulse (center), and resulting pASL dataset (right).

that remain in the acquisition volume are saturated in both acquisitions and should exhibit identical signals. In contrast to this, inflowing blood is only exposed to the upstream selective inversion pulse. Therefore, the RF pulses are used as an intrinsic contrast agent.
Originally, long delays between inversion and image acquisition were used for ASL imaging such that the tagged blood is able to pass into the brain tissue prior to signal readout and image acquisition. Thus, a determination of the cerebral blood flow is possible by subtraction of the two image sequences acquired with and without inversion (see Fig 2.4).
ASL methods for determining the cerebral blood flow can be roughly separated into continuous (cASL) and pulsed (pASL) arterial spin labeling techniques [Wu et al., 2007], whereas techniques combining both approaches have also been presented. The cASL technique employs long RF pulses of 1-2 seconds. In contrast to this, pASL techniques make use of instantaneous RF pulses. Theoretically, cASL enables the acquisition of images at higher signal-to-noise ratios but it is also associated to a higher specific absorption rate (SAR) for the patient.
Apart from perfusion imaging, ASL principles can also be used for an acquisition of time-resolved MRA datasets without contrast agent [Bi et al., 2010]. Here, the time between inversion and image acquisition is alternated within a reasonable range such that the dynamic distribution of labeled blood can be displayed at a temporal resolution as low as 50 ms and concurrent high spatial resolution. Furthermore, ASL techniques can also be used for blood flow territory mapping by applying the inversion pulse only to one artery at time [Helle et al., 2010].
However, the difference between the two images acquired with and without inversion is in the range of 1%, such that several acquisitions and a following averaging is necessary to reduce the contribution of noise artifacts. Therefore, the acquisition of arterial spin labeling datasets requires several minutes.
While the standard ASL methods for determining the cerebral blood flow are already used in clinical practice, the ASL-based acquisition of time-resolved MRA datasets is still subject of recent research. Time-resolved MRA acquisition using ASL techniques seems especially promising in case of contrast agent contraindications. The concurrent

high spatial and temporal resolution is a further benefit of this technique. However, one limiting factor is the T1 relaxation time of blood. Therefore, this technique lacks of a sufficient display of the blood flow in venous structures.

2.2.5 Perfusion-Weighted Imaging

Perfusion-weighted MRI (PWI) is an alternative to the ASL-based determination of the cerebral blood flow. In addition to this, PWI allows the extraction of further perfusion parameters such as the cerebral blood volume and mean transit time. PWI is, for example, frequently used for the diagnosis of acute stroke patients.
There are two main techniques for the acquisition of perfusion-weighted MRI datasets: dynamic contrast enhanced (DCE) and dynamic susceptibility contrast (DSC) imaging [Sourbron, 2010]. Both techniques require a previous application of contrast agent. However, the two techniques differ with respect to the acquisition technique. Similar to time-resolved MRA acquisition, DCE methods utilize T1 contrast enhancing imaging techniques. In contrast to this, DSC techniques do not rely on the T1 relaxation time but utilize susceptibility effects arising from application of paramagnetic contrast agents. These susceptibility effects result in a T2* shortening of the proton spin relaxation times as the contrast agent bolus travels through the vessels and brain tissue. Therefore, T2*-weighted imaging sequences, such as gradient echo planar imaging (EPI), are commonly applied for acquisition of DSC image sequences. It has been shown that the applied bolus is proportional to $\triangle R2^*$ ($R2^* = 1/T2^*$). The measured signal curve $S(t)$ can therefore be transformed to a concentration time curve $c(t)$ using the following relationship:

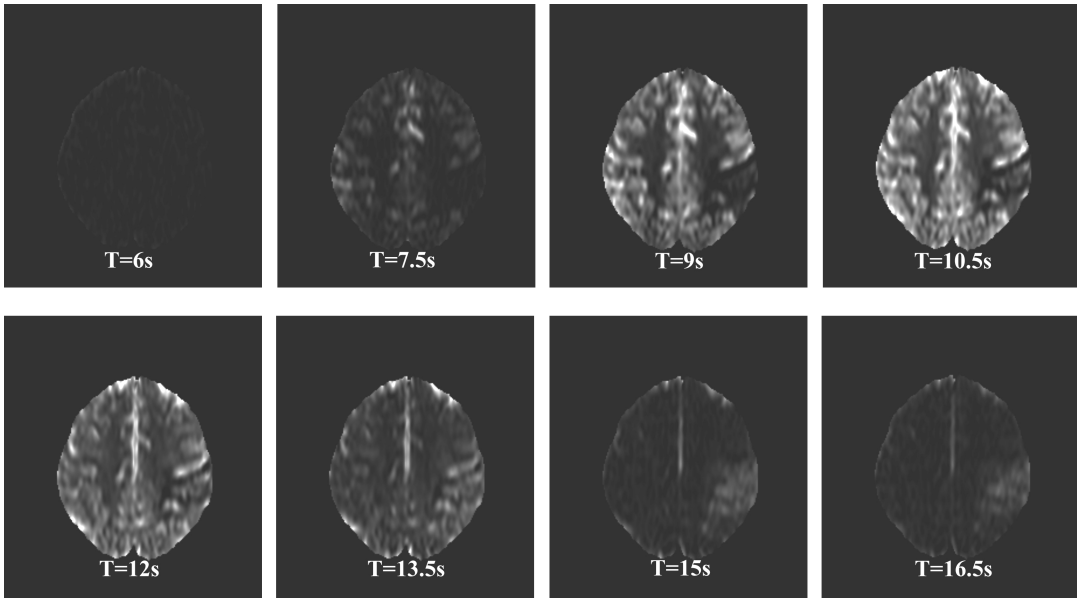

Figure 2.5: Selected slice from a perfusion-weighted MRI dataset at different time points from a patient with an ischemic stroke.

$$c(t) = \frac{-1}{TE} \ln\left(\frac{S(t)}{S(0)}\right),$$

where $S(0)$ describes the baseline signal. After transformation of the signal curves, hemodynamic models that are, for example, described in section 3.2 can be applied for quantitative bolus arrival time determination, which is an important parameter for acute ischemic stroke analysis (see section 4.3.1). T1 weighting is not affected by extravasation effects such that additional parameters like the vascular permeability can be calculated based on the concentration time curves derived from DCE PWI. However, as these parameters are not of high interest for acute stroke patients and T2* effects are considerably stronger, DSC perfusion imaging is the technique most frequently used for diagnosis of acute stroke patients [Sourbron, 2010].

2.2.6 Diffusion-Weighted Imaging

Diffusion-weighted MRI (DWI) is another commonly applied imaging technique for the diagnosis of acute stroke patients. The main idea of this technique is to measure the Brownian motion of molecules using MR principles. Diffusion-weighted imaging makes use of the fact that molecular diffusion causes a MR signal loss, which can be associated with random thermal motion of water molecules [Hahn, 1950]. In the presence of a gradient field, the Brownian motion of spins results in a phase shift of the transversal magnetization and, thus, in an exponential attenuation of the signal. This attenuation depends on the diffusion coefficient of the analyzed tissue and the applied gradient strength. Therefore, very strong so-called diffusion gradients are used for acquisition of DWI datasets to enhance this diffusion effect [Stejskal and Tanner, 1965]. These diffusion gradients are technically realized using bipolar gradients, whereas the so-called b-value controls the degree of MR signal attenuation in terms of a diffusion weighting. High b-values lead to higher diffusion contrasts but also to a worse signal-to-noise ratio. The acquisition of multiple DWI datasets with different b-values, e.g. $b = 0s^2/mm$ and $b = 1000s^2/mm$, allows calculating the apparent diffusion coefficient (ADC) parameter image by making use of the following equation [Dietrich et al., 2010]:

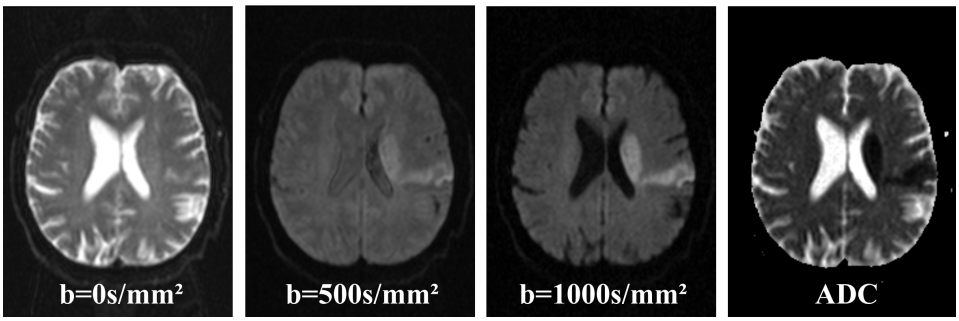

Figure 2.6: Selected slice from a diffusion-weighted MRI dataset acquired with three different b-values and resulting apparent diffusion coefficient (ADC) dataset from a patient with an acute ischemic stroke.

$$S = S_0 \cdot \exp\left(-b \cdot ADC\right),$$

where S_0 describes the baseline signal.
Most MR imaging sequences can be combined with diffusion gradients. However, EPI sequences are commonly used for DWI of the human brain. DWI is especially helpful for the diagnosis of acute stroke patients since it can display ischemic brain tissue with decreased diffusion within minutes from onset.

2.2.7 Fluid-Attenuated Inversion-Recovery Imaging

T2-weighted image sequences are especially helpful to differentiate normal from pathological tissue. This observation can be ascribed to the fact that several cerebral diseases lead to lesions that are associated with an increased water accumulation. Therefore, T2-weighted imaging may serve as a potential image-based biomarker for an estimation of the lesion age in the acute phase of an ischemic stroke [Siemonsen et al., 2009]. However, the association to water content has one important drawback, which arises from the unbound water in the brain, namely the cerebrospinal fluid (CSF). More precisely, it is often difficult to differentiate between a lesion with bound tissue water and unbound CSF in T2-weighted image sequences, especially in case of periventricular lesions.
One possibility to overcome this problem is fluid-attenuated inversion-recovery (FLAIR) MR imaging. Basically, FLAIR is a T2-weighted image sequence, whereas an additional 180° inversion pulse is used to null the signal of CSF [Brant-Zawadzki et al., 1996]. Generally, the signals of all tissues can be nulled using an inversion pulse. However, if selecting a very long inversion time (TI), mainly CSF is affected by such an inversion pulse because the T1 relaxation time of unbound water is very long (approximately 4 seconds). Therefore, all other brain tissues are theoretically relaxed at this time point and exhibit the usual contrast while the inversion pulse only eliminates the signals emitted by spins belonging to CSF (see Fig. 2.7).

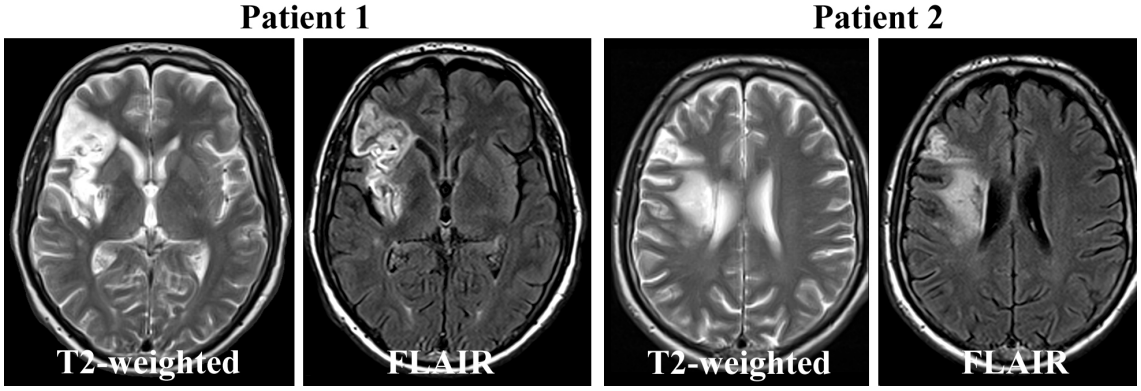

Figure 2.7: Corresponding slices from a T2-weighted and fluid-attenuated inversion-recovery (FLAIR) dataset from two patients with an acute ischemic stroke.

2.2.8 Quantitative T2 Imaging

As mentioned in the previous subsection, T2-weighted image sequences are especially helpful to differentiate normal from pathological tissue. However, the signal intensities in T2-weighted image sequences depend to a large extent on the image sequence and parameters used for image acquisition. For this reason, different T2-weighted images may not be comparable in quantitative terms. Apart from this, it is of interest for several diseases to obtain a quantitative characterization of the normal and pathological brain tissue. These two requirements can be fulfilled by quantitative T2 (qT2) imaging.
The aim of qT2 imaging is to determine the T2 relaxation time for the tissue of interest. However, the T2 relaxation time cannot be measured directly but can only be calculated from a multi-echo T2-weighted image sequence (see Fig. 2.8). Here, the main idea is to acquire at least two T2-weighted datasets with identical parameters except for the echo time TE, which is varied between the different acquisitions (multi-echo acquisition) [Liney et al., 1996]. The acquisition of T2-weighted images can, for example, be performed using a fast spin-echo sequence. After acquisition, quantitative T2 maps can be calculated from the multi-echo image sequence on a voxel-wise basis by fitting the exponential function:

$$S(t) = S_0 \exp\left(\frac{-t}{T2}\right),$$

to the measured signals of the multiple echoes, where S_0 denotes the baseline signal.

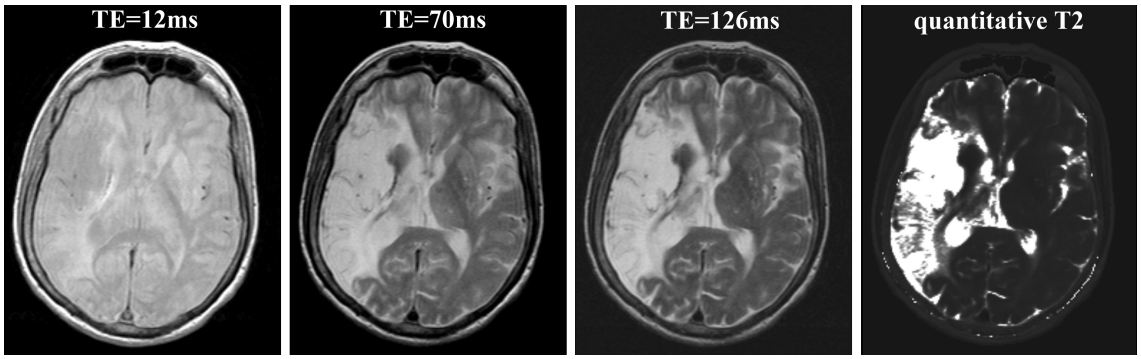

Figure 2.8: Selected slice from a triple-echo T2-weighted image sequence from a patient with an acute ischemic stroke and calculated quantitative T2 dataset (right).

Chapter 3

Model-Based Analysis of Cerebrovascular Diseases Combining 3D and 4D MRA Datasets

Computer-aided image analysis methods can support the clinicians rating MRI datasets of patients with cerebrovascular diseases. From a methodical point of view, there are three main objectives, which have to be dealt with to enable such a computer-aided diagnosis support: the automatic cerebrovascular segmentation from high resolution 3D MRA datasets, the automatic analysis of time-resolved MRA or perfusion-weighted MRI datasets, and the combined analysis and visualization of 3D MRA with high spatial resolution and time-resolved MRA datasets.
This chapter presents the methods, which were developed to accomplish these three objectives. All methods described in this chapter are integrated in the software tool AnToNIa (Analysis Tool for Neuro Imaging Data), which has been developed within the context of this thesis. This software tool offers an intuitive graphical user interface (see Fig. 3.1) and is currently used by the Department of Neuroradiology and the Department of Neurology at the University Medical Center Hamburg-Eppendorf for various clinical and research questions (see chapter 4).

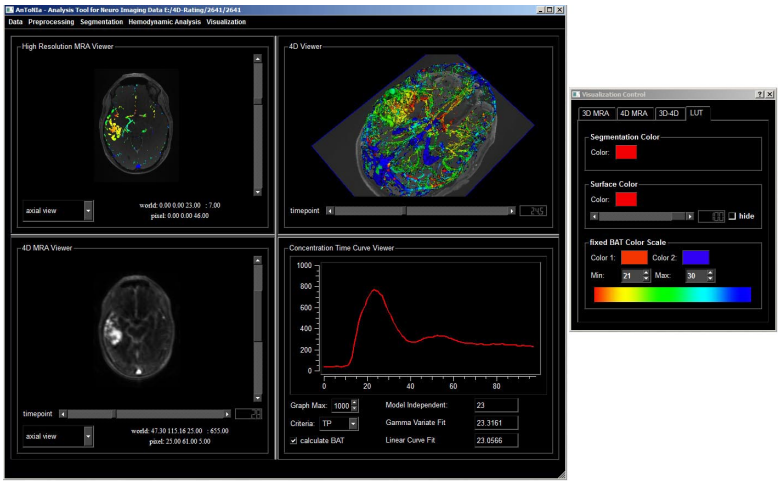

Figure 3.1: Screenshot of AnToNIa (Analysis Tool for Neuro Imaging Data).

3.1 Cerebrovascular Segmentation

The acquisition of angiographic datasets with high spatial resolution enables clinicians to obtain a detailed knowledge about the patient's vascular anatomy. Based on these image sequences it is, for example, possible to plan interventions or analyze the outcome of a treatment. However, one problem that arises with the acquisition of high resolution angiographic datasets is the amount of data that has to be interactively analyzed in clinical practice. Several single vessels have to be tracked in the orthogonal views to obtain a detailed picture of the vascular anatomy. 3D visualizations of the cerebrovascular system could considerably reduce the time needed for interactive screening. Direct volume rendering is not sufficient for this purpose as small vessels, which are often represented by low intensities due to partial volume effects, may not be visible using this visualization technique. Therefore, surface-based or masked volume rendering visualization techniques seem to be better suited for this task. In both cases, a previous segmentation of vascular structures is required for the improved 3D visualization of the cerebrovascular system. In addition to improved visualization possibilities, cerebrovascular segmentations come along with further benefits such as improved registration results of longitudinal angiographic datasets (see section 4.2.2) or possible computational fluid dynamics simulations of the blood flow, e.g. using finite element methods [Cebral et al., 2011, Kakalis et al., 2008, Orlowski et al., 2008].
The segmentation of vascular structures is not only important for cerebrovascular diseases but also for various other organs, such as the liver. Therefore, the segmentation of vascular structures has been in the focus of research for several years resulting in a variety of different approaches. Excellent overviews of current vessel segmentation techniques are, for example, given in [Kirbas and Quek, 2002], [Lesage et al., 2009] and [Suri et al., 2002b].
Current vessel segmentation approaches mainly differ with respect to the integration and extent of a-priori knowledge. This a-priori knowledge may, for example, comprise information about typical vessel shapes or gray value distributions. Generally, the usage of strong shape priors enables a precise segmentation of small vessels that are represented by low intensities and are, therefore, often missed by solely intensity-based segmentation methods. However, one drawback of shape-based vessel segmentation techniques is an insufficient delineation of pathological vessels, which may exhibit considerable variations from a typical vessel shape. Therefore, the results of typical vascular segmentation schemes are usually a trade-off between a sufficient delineation of small or malformed vessels. Anyhow, small as well as pathological vessels may be of high diagnostic interest, especially in case of complex vascular malformations, such that a sufficient segmentation of all vessel structures is required.

The following part of this chapter presents a novel multi-step vessel segmentation procedure, which was developed to enable a segmentation of all vessels at high precision, including small as well as malformed cerebrovascular structures. This multi-step segmentation procedure consists of four steps (see Fig. 3.2): brain tissue segmentation (1), fuzzy-based vessel enhancement (2), extraction of cerebrovascular structures using a level-set method with anisotropic energy weights (3), and detection and correction of gaps in the vessel segmentation (4).

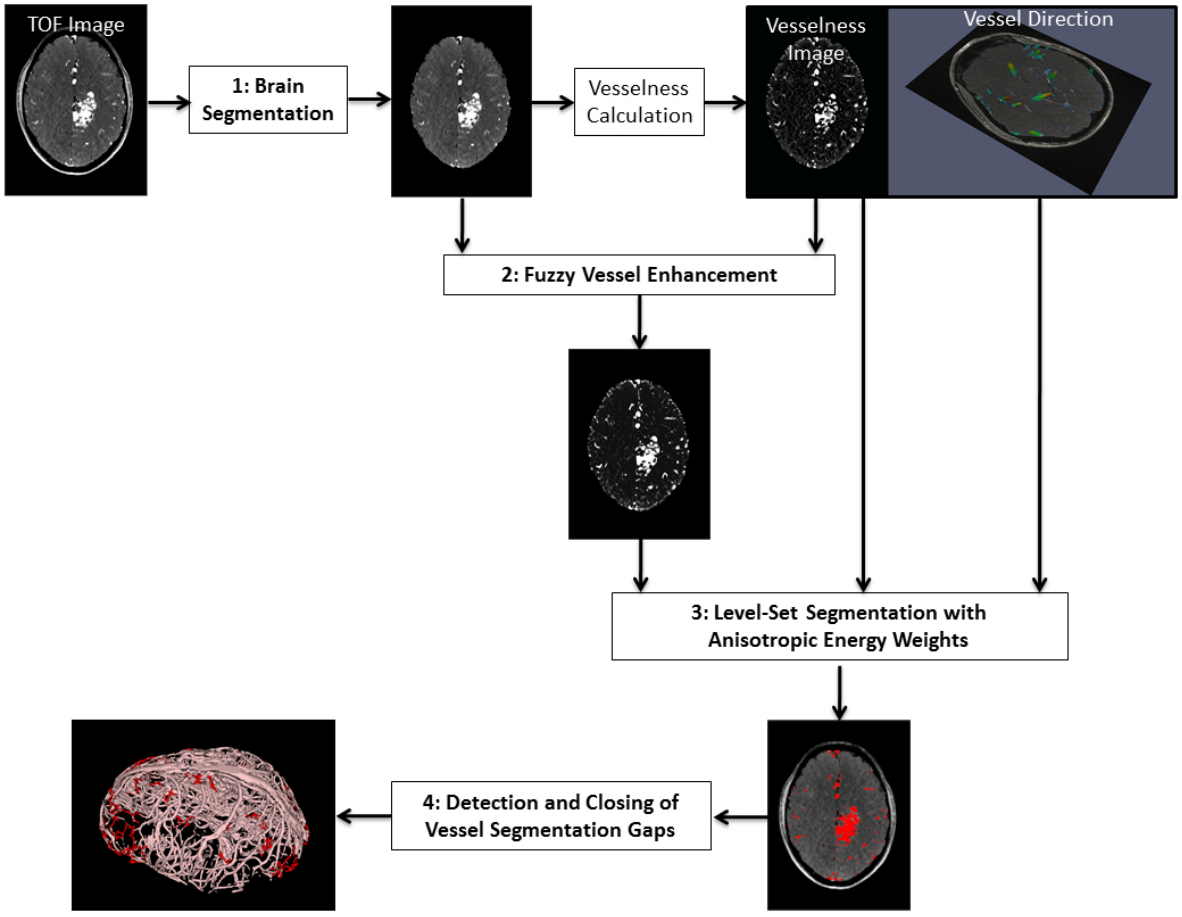

Figure 3.2: Illustration of the single steps of the proposed cerebrovascular segmentation framework.

3.1.1 Brain Segmentation

One general problem for the automatic cerebrovascular segmentation from high-resolution 3D MRA datasets is that several non-vascular structures, such as eyes or skin, are represented by an intensity distribution, which is similar to that of vascular structures. Even a MR image acquisition with fat suppression may not lead to a sufficient intensity reduction of all non-vascular structures. These high-intensity non-vascular tissues pose

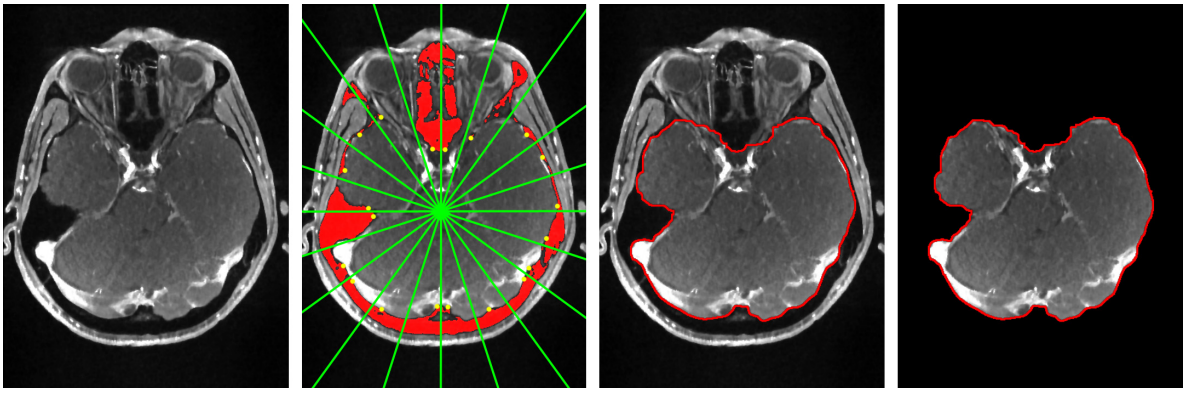

Figure 3.3: Illustration of the single steps of the proposed brain segmentation method. From left to right: Selected slice from a TOF dataset, extracted supporting points, graph-based connection of supporting points, and masked TOF dataset.

a major problem for cerebrovascular segmentation methods as they may cause considerable over-segmentations in terms of a leakage of the segmentation into these structures. Thus, a prior exclusion of these tissues is required to enable an improved cerebrovascular segmentation.
Several brain segmentation approaches, which are often called skull stripping methods, have been proposed in the past, whereas some of these methods are also included in freely available software tools [Fennema-Notestine et al., 2006]. However, these methods were developed with a primary focus on the precise brain tissue extraction from standard T1- or T2-weighted MR images. Therefore, these methods are not optimized for extracting the brain tissue from 3D MRA image sequences, which exhibit special characteristics that differ considerably from those of standard T1- or T2-weighted MR datasets such as high contrasted vessels at the border of the brain.
To overcome this shortage, a new graph-based method for the extraction of brain tissue from 3D MRA datasets was developed in this work [Forkert et al., 2009].
The first step of this graph-based brain segmentation method is the delineation of the low intensity tissues surrounding the brain, which correspond mostly to nasal regions and bone structures. These low intensity structures are extracted using a region growing approach, whereas the required threshold is estimated from the corresponding image histogram by fitting a mixture of two distributions: one Rayleigh distribution for modeling the lower intensity tissues and background, and a Gaussian distribution for modeling the remaining high intensity tissues. This segmentation is used for a slice-wise extraction of supporting points at the border of the brain (see Fig. 3.3). Afterwards, the extracted supporting points are automatically connected using a graph-based method, which utilizes the basic principles of the live-wire approach [Barrett and Mortensen, 1997]. The cost function used for the graph-based connection in this work consists of three cost terms, which are combined to a weighted sum. More precisely, the gradient magnitude, gradient direction and Deriche edge value [Deriche, 1987] are used as cost terms. After graph-based connection of the supporting points in each slice, a 3D binary segmentation

is generated from the single contours. However, this brain segmentation may not be sufficient at regions where the edge information at the border of the brain is too weak for a successful contour extraction. These regions with suboptimal segmentation results need to be corrected in a post-processing step as important vessel structures may be excluded otherwise. For this purpose, these suboptimal segmentation results are automatically detected in a first step by making use of the assumption that the brain contours of two neighboring slices should not exhibit strong differences. After automatic detection of regions with suboptimal segmentation results, a correction of the binary segmentation is performed for each identified region using a non-linear registration method. Therefore, the sub-region exhibiting a sufficient segmentation is registered to the corresponding region in the neighboring slice, which does not exhibit a sufficient segmentation result. The insufficient segmentation region can then be corrected by adapting the sufficient segmentation using the calculated non-linear transformation and a nearest-neighbor interpolation.
The results of the proposed brain segmentation method were evaluated using 18 time-of-flight (TOF) MRA datasets (see section 2.2.1) of patients with an arteriovenous malformation. Interactively delineated brain segmentations from medical experts were available for each dataset and used as ground truth for the evaluation. Furthermore, each dataset was also segmented using three established and freely available brain segmentation methods for comparison purposes. The automatically extracted brain segmentations were compared to the corresponding manual brain segmentations using the Dice coefficient and the Hausdorff distance. Dice coefficients close to 1.0 indicate a good consensus while values close to 0 indicate a bad consensus. In contrast to the Dice coefficient, Hausdorff values close to 0 indicate a good consensus, while higher values indicate a worse consensus. Overall, the results of this evaluation revealed that the proposed method is capable of segmenting the brain tissue in TOF MRA datasets with a mean Dice coefficient of 0.989 and mean Hausdorff distance of 10.2 mm, which is even in the range of the inter-observer agreement (mean Dice coefficient: 0.991, mean Hausdorff distance: 9.6 mm). Compared to these results, the three other automatic brain segmentation methods lead to worse segmentation methods (mean Dice coefficients ranging from 0.980 to 0.907 and mean Hausdorff distances ranging from 22.55 to 77.1 mm). A further analysis showed that the segmentations of the proposed brain extraction method include an average of 99.56% of all cerebrovascular vessels, which is also better compared to the other automatic segmentation results (ranging from 69.29% to 93.38%). It should be highlighted that the other three methods were originally developed for the extraction of brain tissue from standard T1- or T2-weighted MR image sequences and not from TOF datasets.
In conclusion, the results of the evaluation suggest that the proposed brain segmentation method enables an improved extraction of the brain tissue from time-of-flight MRA datasets and is therefore especially helpful to improve the automatic segmentation or direct volume rendering of the cerebral vascular system from TOF image sequences.
A more detailed description of the proposed segmentation method and corresponding results is given in the appendix A.1.

3.1.2 Fuzzy Vessel Enhancement

The exclusion of non-brain tissue from the TOF MRA datasets can considerably improve automatic cerebrovascular segmentation results in terms of preventing leakage into these structures. However, an accurate segmentation of vascular structures remains still challenging. Vessel segmentation methods, which only utilize intensity information, are usually capable of segmenting malformed vessels but suffer from an insufficient delineation of small vessels that are represented by low intensities. In contrast to this, shape-based vessel segmentation methods enable an improved small vessel delineation but may fail to segment vascular malformations, which are not represented by a typical vessel shape. Therefore, a previous non-linear combination of intensity and shape information may enable improved segmentation results, which is the main objective of the second step of the proposed segmentation procedure.
The goal of enhancing vascular structures is achieved in this work by voxel-wisely combining intensity and shape information using fuzzy-logic [Forkert et al., 2011b]. For this purpose, the vesselness filter as proposed by Sato et al. [Sato et al., 1998] is used in a first step to obtain the required shape information from the 3D MRA dataset. The vesselness filter quantifies the likeliness of each voxel to belong to a bright tubular-shaped structure by analyzing the eigenvalues of the corresponding Hessian matrix. A bright tubular structure should exhibit one eigenvalue close to 0 and two large negative eigenvalues. Therefore, the eigenvalues of the Hessian matrix can be used to calculate the vesselness measure for each voxel. After calculation of the vesselness image, two values are available for each voxel: the TOF intensity and the vesselness measure. These two values are combined to one value using fuzzy logic based on an analytically designed rule base. The main benefit of fuzzy decision is the possibility of a non-linear combination and use of uncertain knowledge [Mamdani and Assilian, 1975]. The rule base required for the fuzzy combination was defined analytically using one TOF dataset of a patient with a medium-sized arteriovenous malformation and a corresponding manual segmentation of the cerebrovascular system. The main idea of this rule base is to weight the response of the vesselness filter stronger in case of low TOF intensities, whereas the TOF intensity is weighted stronger for the combination in case of low vesselness values (see Fig. 3.4).
The proposed fuzzy vessel enhancement approach was evaluated based on six TOF MRA datasets, which were preprocessed using the aforementioned brain segmentation method. Each dataset was segmented by one medical expert. The corresponding fuzzy parameter datasets were calculated for each image sequence and segmented using optimal global thresholding. The resulting segmentations were compared to the manual gold standard segmentations using the Tanimoto coefficient. The Tanimoto coefficient is an overlap-measure, which is related to the Dice coefficient. Identical to the Dice coefficient, Tanimoto coefficients close to 1.0 indicate a good consensus, while values close to 0 indicate a bad consensus. For comparison purposes, the TOF and calculated vesselness datasets of each patient were also segmented solely using optimal global thresholding. Furthermore, a naive as well as a joint Bayes classifier were trained with the same patient dataset (TOF and vesselness dataset) as used for definition of the fuzzy rule base.

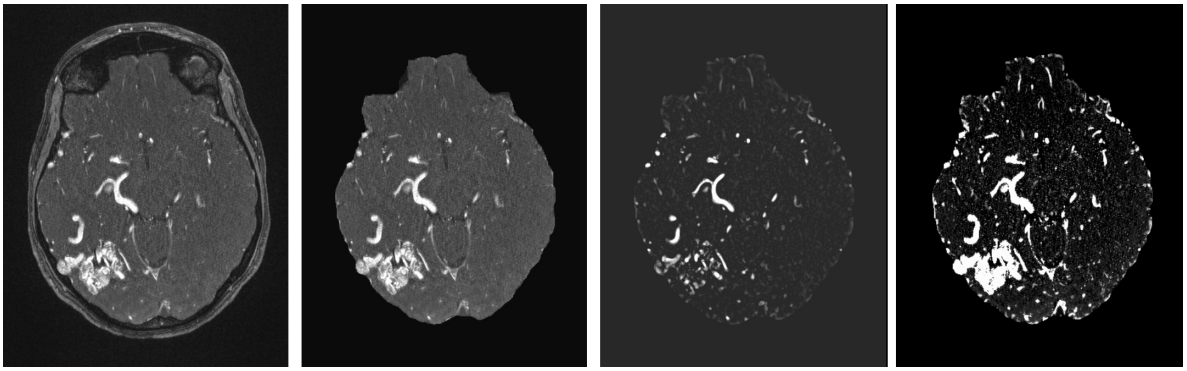

Figure 3.4: From left to right: Selected slice from a TOF dataset of a patient with an arteriovenous malformation before, and after skull stripping, corresponding vesselness parameter image, and resulting fuzzy parameter images with enhanced display of small and malformed vessels.

The trained classifiers were then used for a voxel-wise classification of the remaining six datasets, which were used for segmentation evaluation. Thus, five segmentation results were available for each dataset: optimal TOF intensity thresholding, optimal vesselness thresholding, naive Bayes classification, joint Bayes classification, and optimal thresholding of the fuzzy parameter dataset. The evaluation revealed that global optimal thresholding of the fuzzy parameter image leads to best segmentation results with a mean Tanimoto coefficient of 0.581. Compared to this, solely global thresholding the TOF image sequences or vesselness parameter datasets lead to worse mean Tanimoto coefficients (0.527 and 0.502). The combination of TOF intensities and vesselness measures using a naive Bayes classifier resulted in a mean Tanimoto coefficient of 0.45, which is even lower than the Tanimoto coefficients resulting from single-channel global thresholding. Compared to this finding, a quantitative improvement of the Tanimoto coefficient was found for the combination of the two channels using the joint Bayes classifier (mean Tanimoto coefficient: 0.545). However, global thresholding of the fuzzy parameter dataset lead to the best Tanimoto coefficients in all cases.
The main assumption for the evaluation was that higher Tanimoto coefficients also indicate an improved display of vessel structures in terms of an improved class separation of non-vascular and vascular structures. Therefore, it can be concluded that the proposed fuzzy enhancement method leads to an improved display of vascular structures compared to solely using the TOF or vesselness datasets. Furthermore, the results suggest that the non-linear fuzzy combination also leads to an improved enhancement of vessel structure compared to the fusion using Bayes classifiers.
A more detailed description of the proposed fuzzy enhancement of vascular structures and corresponding results is given in the appendix A.2. Apart from this, the segmentation results from the fuzzy-enhanced datasets are also evaluated using more datasets and manual segmentations in the evaluation of the next segmentation step.

3.1.3 Cerebrovascular Segmentation using Level-Sets with Anisotropic Energy Weights

Despite the improved display of cerebrovascular structures in the fuzzy parameter datasets, an automatic segmentation is still challenging. Lower thresholds lead to an improved small vessel detection but also to an increasing amount of false-positives caused by noise artifacts. Therefore, the main objective of the third segmentation step is to enable the concurrent sufficient delineation of small and malformed vessels while preventing noise related over-segmentations.
This goal was achieved in this work using a variational level-set approach with anisotropic energy weights [Forkert et al., 2012d]. Level-set segmentation schemes have been used for the segmentation of various structures and organs since they have been found topologically flexible and fast for solving complex image segmentation problems. The basic principle of level-set segmentation methods is to deform an initial contour or surface by internal and external forces. The internal energy term is used to keep the boundary smooth while the region-based external energy term drives the contour towards certain image properties. Despite all benefits, level-set segmentation approaches often fail to segment thin structures like vessels, especially if these structures are represented by high surface curvatures and weak edge and intensity values. This observation can be ascribed to the fact that the internal energy is typically stronger than the external energy in such a case, which may even lead to a deletion of small vessel structures from the initial segmentation.
The variational level-set approach developed in this work has been extended in a way that the weight of the internal energy is locally adapted by the vessel direction information, which can also be obtained from the vesselness filter (see Fig. 3.5). Here, the main idea is to weight the internal energy lower if the gradient direction of the level-set is similar to the direction of the eigenvector extracted by the vesselness filter. In this case, only minor or even no smoothing is performed, such that the level-set evolution into small vessels is not hindered by the internal energy weight. In case the eigenvector and the gradient of the level-set are not similar, the segmentation is smoothed as usual, which is supposed to remove and prevent leakages resulting from noise artifacts. Furthermore, an additional vesselness force has been integrated in the level-set formulation, which actively drives the contour along the vessels.
The proposed level-set segmentation method was evaluated using ten TOF datasets. The vascular system was semi-automatically segmented in each dataset by two observers for ground-truth comparison as well as for an analysis of inter-observer differences. In addition to the automatic segmentation using the described level-set method with anisotropic energy weights, four other automatically extracted segmentations were also compared to the manual segmentations for evaluation purposes. More precisely, the intensity-based Z-buffer algorithm [Chapman et al., 2004], the intensity-based stochastic segmentation method [Hassouna et al., 2006], the thresholded fuzzy parameter image (see previous section) and the curve evolution method [Lorigo et al., 2001] were used for this purpose. The curve evolution method is another established level-set approach for the extraction of cerebrovascular structures, which does not utilize anisotropic energy weights. For

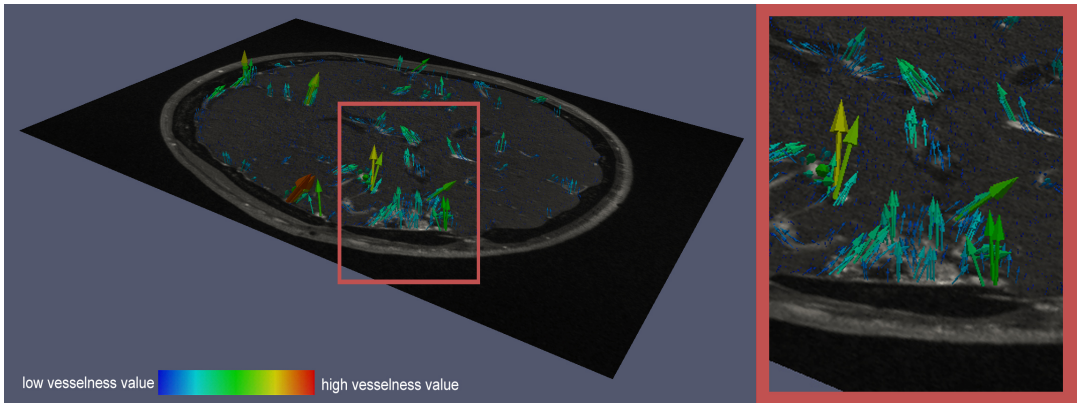

Figure 3.5: Slice from a TOF image sequence and 3D visualization of the first eigenvectors calculated by the vesselness filter.

achieving comparable results, the curve evolution method was also applied to the fuzzy images and corresponding segmentations for initialization. The automatically extracted cerebrovascular segmentations were compared to the manual segmentations using the Dice coefficient as an overlap measure. Furthermore, the number of segmented voxels that belong to vessel structures with a diameter below 1 mm was counted for each segmentation result. In general, the results of this evaluation revealed that the segmentation results obtained from the fuzzy parameter images are better compared to those achieved by the two solely intensity-based segmentation methods (mean Dice coefficients: 0.55 and 0.725). Furthermore, the results showed that both level-set segmentation methods are capable of improving the initial segmentation, which was extracted by global thresholding of the fuzzy parameter image (mean Dice coefficient: 0.762). However, comparing both level-set segmentation approaches demonstrated that the integration of the anisotropic energy weights leads to significantly better vessel segmentation results (mean Dice coefficient: 0.806) compared to the curve evolution method (mean Dice coefficient: 0.783). The segmentation results of the level-set method with anisotropic energy weights are even slightly better than the achieved inter-observer agreement (mean Dice coefficient: 0.791). These quantitative results were also confirmed visually as well as with the second evaluation metric counting the number of voxels belonging to vessel structures with a diameter below 1 mm. Here, the results revealed that the proposed method is capable of delineating an average of 86,660 voxels per datasets, which were determined to belong to such small vessel structures. This result is slightly worse than the performance of the human observers (mean: 90,928 voxels per dataset) but better compared to all other tested automatic segmentation methods.
Overall, the results of this evaluation showed that the presented method enables a precise segmentation of all cerebrovascular structures, including small as well as malformed vessels (see Fig. 3.6). Moreover, the quantitative evaluation has shown that the segmentation results are even in the range of the inter-observer agreement.
A more detailed description of the proposed level-set segmentation method with anisotropic energy weights and corresponding results is given in the appendix A.3.

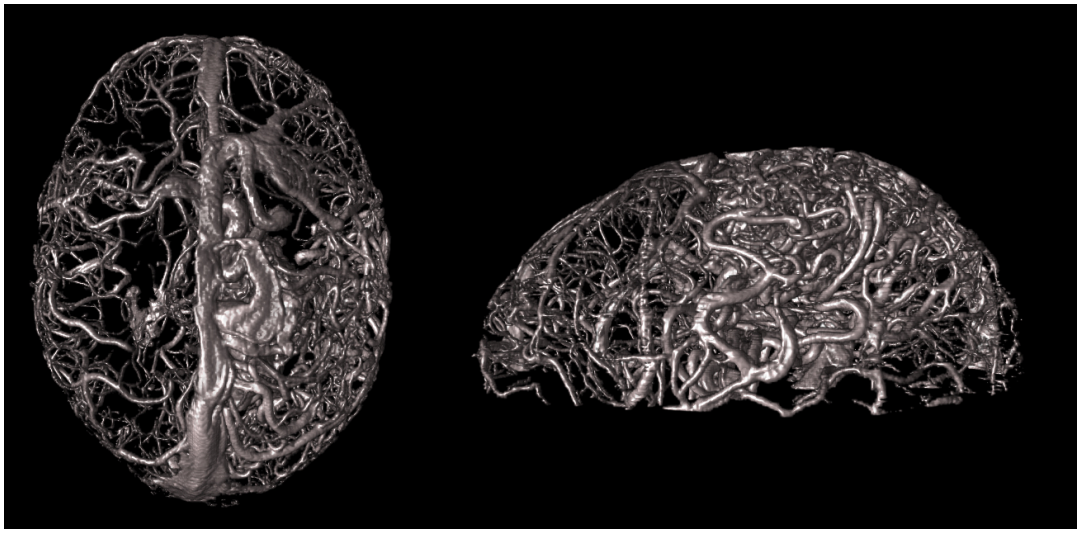

Figure 3.6: 3D visualization of the automatically segmented cerebrovascular system of a patient with an arteriovenous malformation using the level-set method with anisotropic energy weights (axial and sagittal view).

3.1.4 Correction of Gaps in Cerebrovascular Segmentations

Despite the ability of the level-set segmentation method with anisotropic energy weights to segment small vessels with higher accuracy, gaps in the final segmentation can still be observed. These gaps occur mostly at small vessels, which exhibit very low intensities in some parts. For example, small vessels are very important for planning of neurosurgeries in case of arteriovenous malformations or identification of a vessel-free path required for deep brain stimulations. Therefore, the last step of the proposed segmentation procedure aims at detecting and correcting gaps in cerebrovascular segmentations.
This objective was achieved in this work using a 3D graph-based gap closing approach [Forkert et al., 2012c]. Therefore, the 3D centerline of the cerebrovascular segmentation is calculated first using the 3D thinning method proposed by Lee and Kashyap [Lee and Kashyap, 1994]. The centerline representation allows identifying vascular endpoints in the segmentation using a simple neighborhood analysis. More precisely, a vascular endpoint is defined in the 3D centerline representation by a centerline voxel, which possesses only one other centerline voxel in its direct neighborhood. In a following step, possible connections to other voxels of the 3D centerline representation are identified for each vascular endpoint using Dijkstra's algorithm [Dijkstra, 1959]. For this purpose, the vesselness measure was used as the basis for the required cost term. Prior to graph construction, the vesselness parameter image is masked with the inverted vessel segmentation, as already segmented vessel voxels are only of minor interest for the graph-based analysis. The final cost image is calculated by inverting the masked vesselness image, which is used to construct a weighted graph. Dijkstra's algorithm is then applied to detect the shortest paths from a vessel endpoint to all other vertices that correspond to voxels that are part of the 3D centerline representation of the cerebrovas-

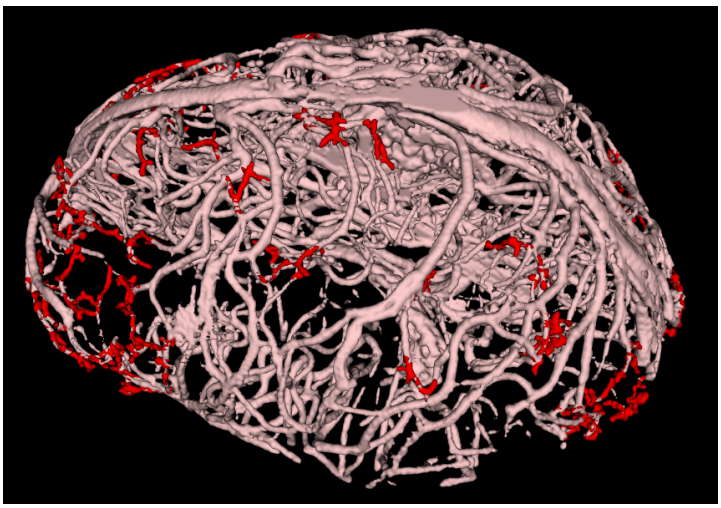

Figure 3.7: 3D visualization of a automatically extracted cerebrovascular segmentation (white) with detected and corrected gaps (red).

cular segmentation. Afterwards, a consistency check is performed to exclude unreasonable paths from the results of the Dijkstra algorithm. Finally, a variational level-set approach [Schmidt-Richberg et al., 2009] is used to expand the remaining paths to the vessel boundaries, which are combined with the initial cerebrovascular segmentation.
The proposed method for the detection and correction of gaps in cerebrovascular segmentations was evaluated using ten TOF MRA datasets. For quantitative analysis, ten gaps were artificially inserted in the corresponding manual segmentations of each dataset. Five of these gaps were inserted at straight vessels and the remaining five gaps were inserted at bifurcations. The proposed method was capable of detecting and correcting 83% of the artificially inserted gaps. No significant difference was found between straight or bifurcation gaps. In a second evaluation, the proposed method was applied to the automatic segmentations extracted from the ten datasets using the described level-set segmentation approach with anisotropic weights (see Fig. 3.7). The visual rating of the detected and corrected gaps by one experienced observer revealed that the proposed method detects an average of 35 new connections per dataset, whereas 92.7% were visually judged as correct.
In summary, the proposed method is capable of further improving cerebrovascular segmentations in terms of reducing gaps.
A more detailed description of the proposed graph-based gap closing method and corresponding results is given in the appendix A.4.

3.2 Cerebral Hemodynamics and Perfusion Analysis

The focus of the previous section was the automatic segmentation of cerebrovascular structures from high-resolution magnetic resonance angiographies. The surface-based 3D visualization of the segmented cerebrovascular system allows an intuitive rating of the individual vasculature of a patient at a high degree of detail. This is, for example, especially helpful in case of vascular malformations but also for identification of the occlusion location in case of an acute ischemic stroke.
However, for certain clinical questions the exclusive anatomical analysis of the cerebrovascular system is not adequate for clinical decision making and additional information about the blood flow and/or tissue perfusion is required. In such a case, time-resolved (4D) MRI is typically performed in addition to 3D MRA image acquisition. As described in section 2.2, different MR techniques are available for time-resolved imaging of the cerebral hemodynamics or perfusion. While 4D MRA techniques can be used to display the blood flow at a macrovascular level (see section 2.2.3), perfusion-weighted MRI (see section 2.2.5) is a commonly applied imaging technique for questions regarding the cerebral tissue perfusion. Both techniques have in common that a contrast agent bolus is applied prior to imaging. The temporal distribution of the given contrast agent can then be measured using MRI principles.
These 4D imaging techniques typically result in a massive amount of 2D images that have to be analyzed by medical experts. Similar to the rating of high resolution angiographic datasets, this can be very time-consuming, which motivates the usage of computer-aided analysis methods. Apart from this, a quantitative analysis of these 4D MRI sequences is often desired in clinical and research settings.
The main idea of hemodynamic analysis methods is to extract the concentration time curves, which represent the density of the applied contrast agent at each measured time point, from the 4D image sequences on a voxel-wise basis. In a following step, the parameters of interest are estimated based on the extracted concentration time curves. Thus, the 4D image sequence is reduced to a 3D parameter map. Several parameters can be estimated based on concentration time curves. One parameter of general interest for the analysis of concentration time curves derived from 4D MRA as well as PWI datasets is the bolus arrival time. Several criteria have been proposed for bolus arrival time definition (see Fig. 3.8). Frequently used criteria comprise the arrival time (AT) and time-to-leading-half-peak (TLHP). Anyhow, the most popular and most often used criterion for hemodynamic analysis studies is the time-to-peak (TTP) parameter.

3.2.1 Reference-Based Linear Curve Fitting Method

Typical concentration time curves are not only affected by noise and contrast agent bolus recirculation but are also only represented by discrete sample points (see Fig. 3.8). Due to these reasons, the direct estimation of the bolus arrival time (and other parameters) is often error-prone. Numerous parametric models have been proposed in the past, which are fitted to the discrete concentration time curves prior to parameter estimation to

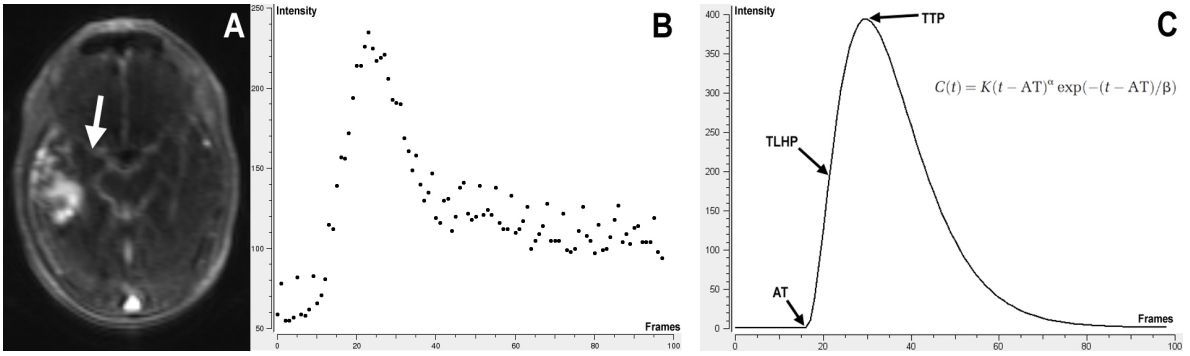

Figure 3.8: Selected slice from a 4D MRA dataset (A), discrete concentration time curve (B) for the artery marked by the arrow, and examples for different bolus arrival time criteria (AT = Arrival Time, TLHP = Time to Leading Half Peak, TTP = Time to Peak) displayed using an ideal gamma variate model curve (C).

overcome these drawbacks. Examples for previously published parametric models comprise the gamma variate model [Thompson et al., 1964], the local density random walk model [Bogaard et al., 1986] and the modified log-normal model [Linton et al., 1995]. However, these models make strong assumptions regarding the shape of typical concentration time curves, which might not be fulfilled for any pathological situation.
The reference-based linear curve fitting model [Forkert et al., 2011a], which was developed within the context of this work, was designed to estimate the bolus arrival time from a given concentration time curve without the need of making explicit assumptions about typical shapes of indicator dilution curves. The main idea of this approach is to extract a hemodynamic reference curve directly from the time-resolved dataset. Therefore, n concentration time curves are randomly selected from the time-resolved MR dataset. An analysis of the standard deviation of the curve values is used to exclude curves, which do not exhibit a sufficient signal peak and corresponding signal drop, from this selection. A patient-individual hemodynamic reference curve is then calculated from the randomly extracted curves using curve fitting techniques. A B-spline approximation is used to enable the evaluation of curve values between the discrete sample points. After this, a patient-specific hemodynamic reference curve can be calculated by averaging of the fitted n concentration time curves. This hemodynamic reference curve usually exhibits a smooth shape, such that the reference bolus arrival time, e.g. the time-to-peak, can be defined unambiguously. This generated patient-individual hemodynamic reference curve is fitted to each discrete concentration time curve of the same 4D MR dataset for estimating the corresponding bolus arrival time (see Fig. 3.9). More precisely, the resulting parameters from this curve fitting are used to transform the defined reference bolus arrival time to each analyzed curve. The main benefit of this approach is that no assumption about typical shapes of concentration time curves is made, since this information is implicitly modeled in the reference curve.
The proposed hemodynamic model was evaluated using Monte-Carlo simulations. Therefore, a neuroradiologist defined seven different cerebrovascular structures of diagnostic

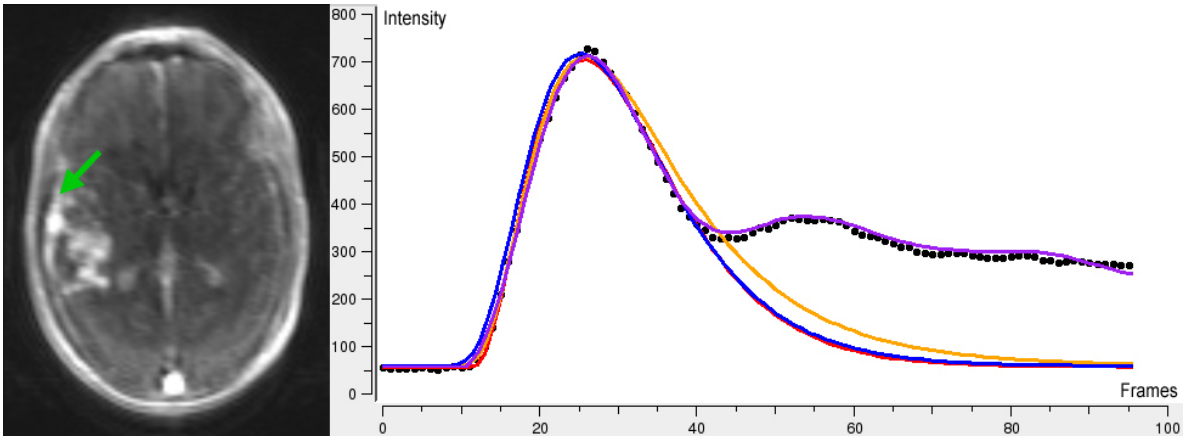

Figure 3.9: Examples for parametric hemodynamic models fitted to a discrete concentration time curve (black dotted) obtained from a 4D MRA image sequence (left): simplified Gamma Variate Model (red), Local Density Random Walk Model (blue), modified Log Normal Model (orange), and reference-based linear curve fit model (purple).

interest, including arteries as well as veins, in a 4D MRA dataset as well as six tissue structures, including arteries, stroke and healthy brain tissue, in a PWI dataset. The discrete concentration time curves were extracted for each defined vascular structure or tissue of interest and a combination of two gamma variate functions was interactively fitted to each curve. The gamma variate model is currently the most often used hemodynamic model in indicator dilution studies. This approximation allowed defining the ground truth bolus arrival times, which were used for evaluation purposes. For simulation of new concentration time curves, the fitted curve functions were randomly shifted in time-dimension, discretized with the original temporal resolution (4D MRA: 0.5 s and PWI: 1.5 s) and Gaussian noise was added (signal-to-noise ratio SNR: 20, 50, 500). These simulated discrete curves were then employed for estimating the bolus arrival times using the described reference-based linear curve fitting method. Furthermore, five other established hemodynamic models were also used for bolus arrival time estimation for comparison purposes (the gamma variate model, the local density random walk model, the modified log-normal model, the LL-model and LQ-model).
The results of the evaluation based on the Monte-Carlo simulation showed that the best results can be obtained using the time-to-peak criterion for bolus arrival time estimation. More precisely, the results demonstrated that the proposed model is capable of improving the time-to-peak estimation precision at lower SNRs by up to 59% for 4D MRA datasets and up to 24% for perfusion-weighted datasets compared to the other tested models. In contrast to this finding, the gamma variate function lead to the highest precision for the signal-to-noise ratio of 500. However, a SNR of 500 is rather a theoretical value that is unlikely to be found in real datasets. Apart from this, the application of the reference-based linear curve fitting model leads to a considerable speed-up of the computation time of at least 33% in comparison to the other parametric models.
In summary, the proposed reference-based linear curve fitting model leads to an improved

time-to-peak estimation precision compared to established hemodynamic models.
A more detailed description of the proposed reference-based linear curve fitting approach and corresponding results of the evaluation using the Monte-Carlo simulation is given in the appendix B.1.

3.2.2 Temporal Resolution Requirements for Different Vessel Structures

The Monte-Carlo simulation applied for evaluation of the reference-based linear curve fitting model was performed using three different signal-to-noise ratios but only with a fixed temporal resolution of 0.5 seconds for the simulated 4D MRA concentration time curves. This temporal resolution was selected as it is equal to the temporal resolution of the 4D MRA datasets, which were used as the basis for the simulation. Due to technical reasons, 4D MRA imaging cannot be performed with concurrent high spatial and high temporal resolution. Therefore, 4D MRA imaging is a trade-off between the spatial and temporal resolution. A high spatial resolution enables an improved display of vessels, especially that of small vessels. In contrast to this, a high temporal resolution may be beneficial for the hemodynamic analysis. However, not much is known about the influence of the temporal resolution to the error of the bolus arrival time estimation, which can be used for the blood flow analysis. Thus, it is essentially unknown, which 4D MRA temporal resolution is really required for a reasonable hemodynamic analysis. A detailed knowledge about this relation may enable an acquisition of 4D MRA image sequences with a case-optimal temporal resolution, which may also allow an acquisition of 4D MRA datasets with higher spatial resolution.
Therefore, a more detailed analysis of the bolus arrival time estimation precision of the different models using the aforementioned Monte-Carlo simulation as well as real clinical datasets was performed with a special focus on determining the optimal temporal resolution for different vascular structures [Forkert et al., 2012b]. This analysis, which is described in the following, was performed exclusively for the time-to-peak criterion, since the previous results showed that this criterion leads to the best bolus arrival time estimations. Here, the same 4D MRA Monte Carlo simulation setup as used for the first analysis was also employed for this evaluation. More precisely, a signal-to-noise ratio of 60 was used while the discretization was performed using temporal resolutions ranging from 0.1 to 5.0 seconds. Furthermore, a second analysis using real clinical 4D MRA datasets was performed for a comparison of the simulation results to those obtained from real datasets. Overall, 226 concentration time curves of diagnostic interest were extracted from 20 time-resolved MRA datasets of patients with an arteriovenous malformation for this purpose. The temporal resolution of the extracted concentration time curve was artificially decreased and the time-to-peak was estimated and compared to those obtained at original temporal resolution. The results of this clinical evaluation were further stratified for the different vessel structures (arteries, veins and arteriovenous malformation vessel structures).
Overall, the results of this more detailed evaluation support the findings of the first exper-

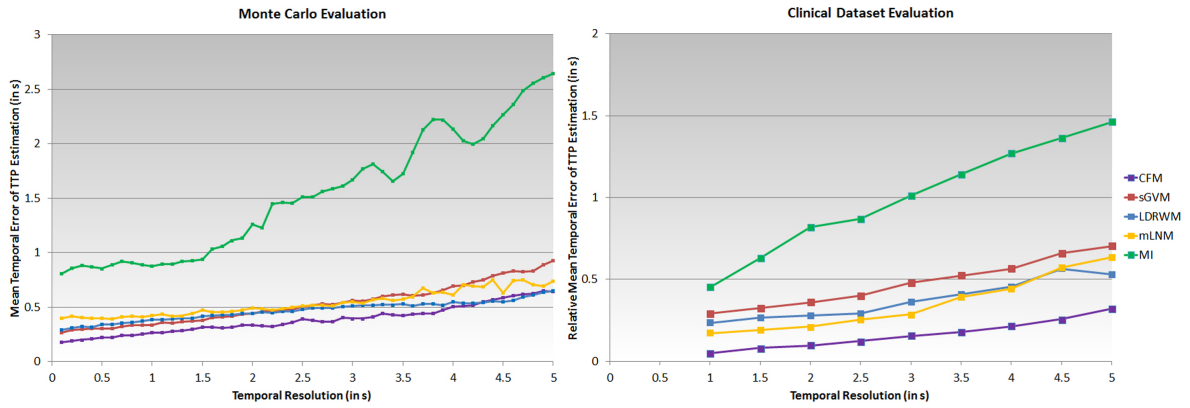

Figure 3.10: Mean time-to-peak estimation errors obtained from the Monte Carlo and clinical evaluation using the reference-based linear curve fit model (CFM), the simplified gamma variate model (sGVM), the local density random walk model (LDRWM), the modified log-normal model (mLNM), and model-independent (MI) time-to-peak estimation.

iments. To begin with, the findings of the evaluation using the clinical datasets suggest that the Monte-Carlo simulation represents a realistic setup for the evaluation of hemodynamic models as a close resemblance was found between the corresponding results of the different models. Moreover, the results revealed that the proposed reference-based linear curve fitting method leads to the best bolus arrival time estimations for 4D MRA temporal resolutions between 0.1 and 4 seconds, while the local-density random walk model performs better for temporal resolutions between 4 and 5 seconds (see Fig. 3.10). The stratification of the results from the clinical dataset evaluation revealed that arteries require a higher sampling rate to achieve bolus arrival time estimation accuracies comparable to those for veins and arteriovenous malformation vessel structures. More precisely, a temporal resolution of 1.5 seconds for arteries and 2.5 seconds for venous and arteriovenous malformation vessel structures appears to be reasonable for clinical applications.

In summary, the results of this study show that the proposed reference-based linear curve fitting model leads to better time-to-peak estimations for temporal resolutions between 0.1 and 4 seconds than the other hemodynamic models evaluated. Moreover, the results of this study suggest that a temporal resolution of 1.5 seconds is sufficient for time-resolved MRA acquisition if all vessel structures are of diagnostic interest, while a temporal resolution of 2.5 seconds seems reasonable if mainly venous vessel structures are of clinical interest.

A more detailed description of this evaluation using Monte-Carlo simulations and clinical datasets as well as corresponding results is given in the appendix B.2.

3.3 4D Blood Flow Visualization

The hemodynamic analysis enables a quantitative evaluation of time-resolved angiographic datasets, which can be used to investigate the patient-individual cerebral blood flow. This analysis can, for example, be performed by estimating the time-to-peak value for selected vascular structures of interest. Moreover, this procedure can also be applied to estimate the time-to-peak value for each voxel of the 4D MRA image sequence such that the 4D dataset is reduced to a 3D parameter dataset (e.g. time-to-peak map), which enables a global evaluation of the blood flow. In contrast to this, the automatic cerebrovascular segmentation procedure allows displaying the case-specific vascular anatomy at high detail using 3D surface models. Anyhow, a direct combined analysis and visualization of the cerebrovascular system and the corresponding blood flow situation is still not possible at this stage. Therefore, the clinicians are still challenged to examine the two results separately, whereas the imaginary combination of both is very challenging and time-consuming as it requires a profound experience and imagination. Thus, a combined visualization of the anatomy together with the hemodynamic setting may reveal several benefits for the clinical routine such as a faster and intuitive rating of a patient dataset or less human errors. Such an intuitive blood flow visualization combining 3D and 4D MRA datasets has not been presented nor evaluated in the past.

3.3.1 4D Blood Flow Visualization Combining 3D and 4D MRA Datasets

To overcome this shortage of a sufficient combined analysis and visualization of 3D and 4D MRA image sequences, a novel 4D blood flow visualization technique has been developed within the context of this thesis [Forkert et al., 2012a]. The main challenge for the combined analysis and visualization of the patient-individual vascular anatomy and blood flow situation is the registration of the 3D and 4D MRA image sequences. The registration is mainly required since the two image sequences exhibit different spatial resolutions. Furthermore, different fields-of-view used for acquisition or a change of the patient position within the scanner between the two acquisitions may also occur. Therefore, a direct combination of the two image sequences is not possible. The fusion of the hemodynamic information obtained from the 4D MRA image sequence with the 3D MRA dataset of a patient requires a previous rigid registration of both image sequences. For this purpose, the 4D MRA image sequence is first reduced to a 3D temporal maximum intensity projection (MIP). The temporal MIP is calculated by voxel-wisely extracting the concentration time curve from the 4D MRA image sequence and determining the corresponding maximal signal intensity. The resulting dataset exhibits an advanced representation of the vessel structures, which is not affected by different arrival times of the contrast agent bolus. The calculated temporal MIP is used for the calculation of the optimal rigid transformation to the 3D MRA image sequence by maximizing the mutual information [Wells et al., 1996], which allows transforming the time-to-peak parameter map to the 3D MRA image sequence. More precisely, a linear interpolation is used for

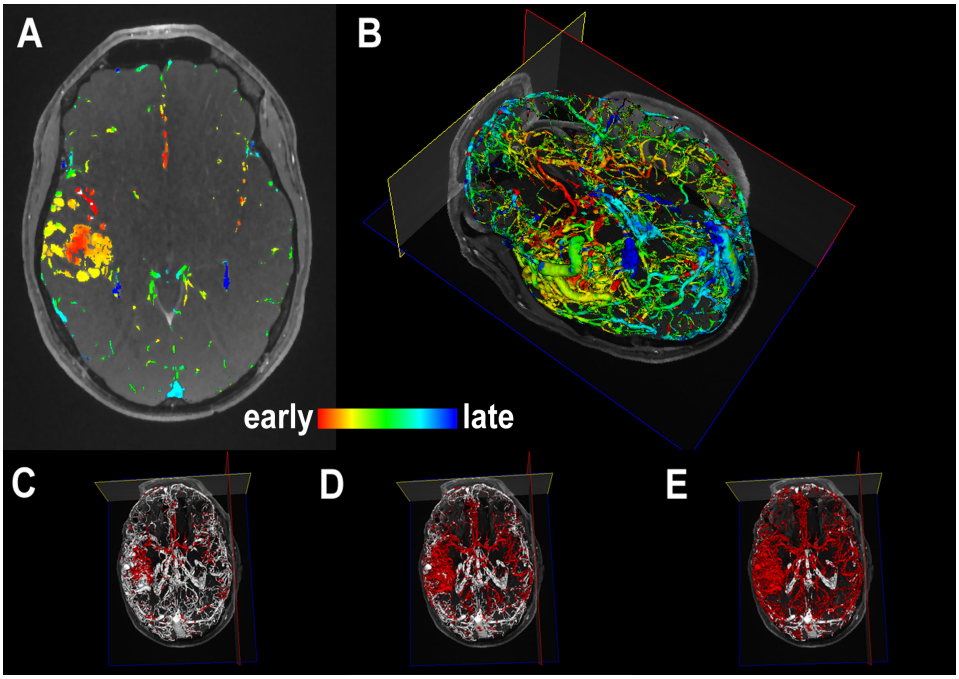

Figure 3.11: Color-coded static visualization of the cerebral blood flow superimposed on a selected slice from a 3D MRA dataset (A) and on the 3D surface model (B), and the corresponding 4D blood flow visualization at three selected time points (C-E).

the calculation of the rigid registration, while a nearest-neighbor interpolation is used for the transformation of the time-to-peak parameter map. This ensures that the time-to-peak parameter values are not smoothed between vascular and non-vascular structures. After registration, the time-to-peak estimations can be displayed slice-wise in a color-coded fashion superimposed on the 3D MRA image sequences, which is especially helpful to obtain hemodynamic information from the inside of vascular malformations (see Fig. 3.11). However, the transformed hemodynamic information cannot be displayed directly on the 3D surface model generated from a cerebrovascular segmentation since only the blood flow at the vessel border would be visible in this case. For this reason, the 3D centerline representation of the cerebrovascular system is used for a projection of the time-to-peak values in the center of a vessel to the border. After this, the hemodynamic information can be displayed color-coded or dynamically over time on the 3D cerebrovascular surface model (see Fig. 3.11).
The methodical limitations of the proposed visualization method were evaluated using synthetic software phantoms [Säring et al., 2010]. These software phantoms enable generating synthetic 3D and 4D MRA image sequences that contain straight vessels with different diameters and distances to each other. Furthermore, a ground-truth time-to-peak map with a spatial resolution equal to the synthetic 3D MRA dataset is also generated, which can be used for comparison with the registered time-to-peak map obtained from the synthetic 4D MRA image sequence. Overall, 10 software phantoms were generated for this evaluation. Each software phantom consisted of six vessels with

decreasing diameters (between 6 and 1 mm). The ten software phantoms differed with respect to the distance between the six vessels (ranging from 10 to 1 mm). The evaluation of this 4D blood flow visualization using the generated software phantoms showed that the vessel diameter has a strong impact on the precision of the blood flow reconstruction. In contrast to this finding, the distance between vessels seems to have no considerable influence on the blood flow reconstruction. More precisely, the results of the software phantom evaluation revealed that the proposed method is capable of properly representing the blood flow for vessels with a diameter larger than 2 mm, for which a mean temporal difference of 0.27 seconds or lower compared to the ground-truth time-to-peak parameter values was achieved.
It may be concluded that the main bottleneck of the proposed 4D blood flow visualization is the spatial resolution of the 4D MRA image sequence, as the blood flow can only be properly reconstructed for vessels with a diameter exceeding the corresponding spatial resolution. Apart from this, the presented method enables an intuitive rating of the anatomy and blood flow from any view angle in only one representation.
A more detailed description of this 4D blood flow visualization method and corresponding results is given in the appendix C.1.

3.3.2 Clinical Evaluation of the 4D Blood Flow Visualization

The evaluation of the 4D blood flow visualization described above was performed with a primary focus on analyzing the methodical limitations of this method. The most important result of this evaluation was that the spatial resolution of the underlying 4D MRA image sequence is the main limiting factor for a proper high resolution blood flow reconstruction. More precisely, the blood flow could only be sufficiently reconstructed for vessel structures with a diameter larger than 2 mm, which can be ascribed to the in-slice spatial resolution of the used 4D MRA image sequences. However, the proposed method has not been evaluated in depth with respect to clinical applications.
Therefore, a detailed clinical evaluation of the 4D blood flow visualization was exemplarily performed for patients with an arteriovenous malformation (AVM) [Illies et al., 2013]. AVMs are characterized by a direct connection of arteries to dilated and tortuous veins without interposing capillaries, which are replaced by multiple arteriovenous fistulas (see section 4.1). Today, the digital subtraction angiography (DSA) is still considered the gold-standard imaging technique for rating of AVMs, despite several drawbacks. Among others, these drawbacks comprise complications, which arise from the invasive catheter-based procedure, exposure of the patients and clinicians to ionizing radiation and loss of 3D information due to the 2D projection. However, DSA image sequences offer an improved spatial (projected to 2D) and temporal resolution compared to clinically approved 4D MRA imaging techniques. The clinical evaluation of the 4D blood flow visualization was performed using datasets of 31 AVM patients. DSA image sequences as well as 3D and 4D MRA datasets were available for each patient. The 3D and 4D MRA datasets were used for the generation of the 4D blood flow visualization using the aforementioned methods. The resulting 4D blood flow visualizations were compared to the corresponding DSA image sequences. More precisely, the DSA image sequences were rated by one

observer using the Spetzler-Martin grading scale [Spetzler and Martin, 1986]. This scale is frequently used for estimating the risk of an AVM surgery. More precisely, an AVM is graded based on the parameters nidus size (<3 cm: 1 point, 3-6 cm: 2 points and >6 cm: 3 points), venous drainage (superficial: 0 points, deep: 1 point) and region (non-eloquent: 0 points, eloquent: 1 point). The three sub-scores are added to the global score, whereas higher scores indicate a higher surgery risk. The same grading scale was also used for rating the corresponding 4D blood flow visualization, which was independently performed by two other observers.
The global Spetzler-Martin grading scores were determined equally in 27 out of the 31 cases by the two raters, who used the 4D blood flow visualizations. More precisely, the two raters achieved total agreement regarding the brain eloquence parameter and also agreed in 30 out of the 31 cases regarding the nidus size grading. However, the two observers did not agree regarding a deep drainage in 3 of the 31 cases. All of these disagreements could be ascribed to small vessels with a diameter less than 2 mm. Comparing the Spetzler-Martin grading scores derived from rating DSA image sequences to those determined by the 4D visualizations revealed an agreement in 26 cases for the first observer and in 28 cases for the second observer of the 4D visualizations. Again, most differences regarding the Spetzler-Martin score could be attributed to the draining vein parameter, whereas more AVMs were determined to drain into the deep system by rating the 4D visualizations. However, instead of being incorrect, this observation may actually represent the real case, as the two observers judged the 4D blood flow visualization to enable an improved depiction of draining veins, which may not be visible in the 2D projections of a DSA image sequence.
Overall, the clinical evaluation revealed a good inter-rater reliability and accordance of the 4D blood flow visualization with state-of-the-art DSA rating. Nevertheless, the methodical limitation of the 4D blood flow visualization regarding very small vessel structures was also confirmed in this clinical evaluation. At this point, this visualization technique may be considered a valuable rating opportunity in addition to state-of-the-art digital subtraction angiographies. It should be emphasized that the 4D MRA image sequences used for this clinical evaluation were acquired with a temporal resolution of 0.5 seconds. As highlighted in section 3.2.2, a temporal resolution of 1.5 seconds would have been sufficient for the hemodynamic analysis. The acquisition of 4D MRA image sequences has been recently adjusted at the University Medical-Center Hamburg Eppendorf according to this finding. Hence, it was possible to increase the spatial resolution of these datasets considerably, whereas new study results using these datasets are not available yet. With this improvement or with the development of new 4D MRA imaging techniques, it may be possible to replace the DSA completely in near future. Apart from this, the clinical evaluation of the 4D blood flow visualization also revealed that each AVM nidus can be classified into one of three different flow patterns, which may represent an additional benefit of this method.
A more detailed description of this clinical evaluation and corresponding results is given in the appendix C.2.

Chapter 4

Clinical Applications of the Developed Methods for Diagnosis and Research of Cerebrovascular Diseases

The main motivation of the previous chapter was to describe and highlight the main methodical contributions of this work regarding the automatic segmentation of cerebrovascular structures from 3D MRA datasets, the hemodynamic analysis based on 4D MRA or perfusion-weighted MRI datasets, as well as the combined analysis and visualization fusing the high-resolution 3D and time-resolved MRA datasets by utilizing the results of the automatic cerebrovascular segmentation and hemodynamic analysis.
One possible clinical application of these methods has already been presented within the context of the clinical evaluation of the 4D blood flow visualization. In particular, this was the clinical rating of patients with an arteriovenous malformation using the 4D blood flow visualization. However, this dynamic blood flow visualization of patients with a cerebrovascular disease is not the only clinical application for which the described methods can be used. More precisely, the developed hemodynamic analysis or automatic vessel segmentation methods have also been successfully applied for various other image-based research projects regarding three cerebrovascular diseases: brain arteriovenous malformations, cerebral aneurysms and acute ischemic strokes.
The aim of this chapter is to present the study designs and main findings of the clinical research projects, which were conducted regarding these cerebrovascular diseases using the developed methods that are implemented in the software tool AnToNIa. Furthermore, a brief medical background is given for each mentioned cerebrovascular disease with a special focus on the conducted research projects prior to describing the methods, study designs, and corresponding results.

4.1 Model-Based Analysis of Arteriovenous Malformations

Brain arteriovenous malformations (AVMs) are cerebrovascular malformations with a reported incidence rate of 1.34 per 100,000 persons per year in unselected populations [Stapf et al., 2003]. AVMs are characterized by a direct connection of arteries to dilated and tortuous veins without interposing capillaries. These capillaries are replaced by multiple arteriovenous fistulas [Choi and Mohr, 2005], whereas this complex conglomerate is often called the nidus of an AVM.
It is typically assumed that the missing capillaries lead to high blood flow velocities due to the low-resistance condition [Anbarasu and Gould, 2002]. This high blood flow velocity has been related to two main effects that are typically associated with AVMs.
First, a dilation of the draining veins is often observed in patients with AVMs. This fact can be ascribed to the missing arterioles and capillaries. One of the main functions of the capillaries, apart from the metabolism, is the regulation of the blood pressure between arteries and veins. In general, the blood pressure in veins is considerably lower compared to arteries. The normal construction of veins does not allow resisting an arterial pressure condition over long time. The high arterial pressure may, therefore, lead to a dilation of veins by vascular remodeling, which may ultimately result in a rupture due to weakened vessel walls. Such an intracerebral hemorrhage is the major and most severe symptom of an AVM. Other unspecific symptoms of an AVM range from epileptic seizures, headaches and focal-neurological deficits [Fleetwood and Steinberg, 2002]. The incidence for an AVM-related hemorrhage is typically estimated between 2 and 4% per annum [Kondziolka et al., 1995], while the life-time risk for an AVM-related seizure is typically estimated at 50% [Lantz and Meyers, 2008]. The risk for an AVM-related vessel rupture has been associated to several patient-individual factors, such as the location of a present AVM, the venous drainage pattern or associated aneurysms [Stapf et al., 2006]. However, previous studies revealed that the patient-individual risk for an anew hemorrhage increases up to 18% after the occurrence of a bleeding [Mast et al., 1997]. Apart from this, not much is known how these different risk factors influence the patient-individual hemorrhage risk or the hemodynamic situation, which in turn may be related to the hemorrhage risk.
The second effect, which has often been associated with the high-flow condition in AVMs, is the so-called steal effect. The concept of the steal effect presumes that the increased blood flow through a low-resistance vascular bed leads to a flow diversion away from the adjacent brain tissue areas [Costantino and Vinters, 1986]. Therefore, it has been hypothesized that the brain tissue in the vicinity of an AVM that is supplied by healthy vessels is hypoperfused. The existence of the steal phenomenon has been associated to several neurological symptoms in AVM patients such as transient neurological deficits [Guo et al., 2004].
The main aim of an AVM therapy is the prevention of a hemorrhage. Treatment strategies comprise the neurosurgical resection, endovascular embolization, and radiosurgery [Ogilvy et al., 2001]. However, in many cases a combination of these techniques is ap-

plied for therapy. In any case, exact knowledge about the patient-individual anatomy of the cerebrovascular system and its blood flow condition is required for optimal planning of the treatment. Within this context, it is especially important to define the feeding arteries and draining veins of an AVM.
AVM rupture risk estimation is a crucial step of clinical decision making in AVM patients. This is especially the case since not all AVMs lead to a rupture and any invasive therapy can bear extensive risks for the patient. Ideally, treatment should only focus on patients with an AVM, which is likely to rupture. However, a precise patient-individual rupture prognosis is not feasible with the current knowledge and available parameters.

4.1.1 Association of Hemodynamics with AVM Rupture Risk Factors

As highlighted in the introduction of this section, several morphological factors have been identified in previous studies, which are supposed to increase the risk for an AVM related hemorrhage. Among others, a previous intracranial hemorrhage, a deep nidus location, an infratentorial nidus location, a deep drainage, an associated aneurysm, a small nidus size, a draining venous stenosis, and one or two/three draining veins have been related to an increased AVM rupture risk. However, a large prospective study revealed that a previous hemorrhagic presentation, a deep nidus location, and an exclusive deep drainage are the strongest predictors for an AVM related hemorrhage [Stapf et al., 2006]. So far, not much is known if and how these morphological rupture risk factors influence the cerebral hemodynamic situation. Therefore, two research studies were performed within the context of this work to investigate this relation in more detail.

The aim of the first study was to analyze a possible influence of risk factors for an AVM-related hemorrhage on the time-of-flight intensity signal distribution within the AVM nidus [Forkert et al., 2013a]. TOF intensity signals are related to the blood flow velocity and contrast agent, if given (see section 2.2.1). More precisely, turbulent or concentric blood flow may lead to a spatially restricted decrease of the TOF signal magnitude, while contrast agent trapped inside the nidus may lead to a local signal increase. Therefore, TOF signal intensities can be used for an indirect and simple analysis of the intranidal blood flow.
Overall, datasets of 50 patients with an arteriovenous malformation were available for this study. After preprocessing of the TOF MRA datasets, the cerebrovascular system was segmented in each TOF image sequence using the developed segmentation procedure (see section 3.1). The resulting cerebrovascular segmentations were used as the basis for an interactive definition of the AVM nidus in each dataset. Each AVM nidus segmentation was then employed for an extraction of the corresponding histogram of the TOF signal intensities within the AVM nidus. Finally, the extracted histograms were analyzed by calculating the skewness, kurtosis, mean and median TOF intensity, and full-width-half-maximum parameter. For statistical analysis, the 50 patients were grouped into two classes. More precisely, patients were classified to the high rupture

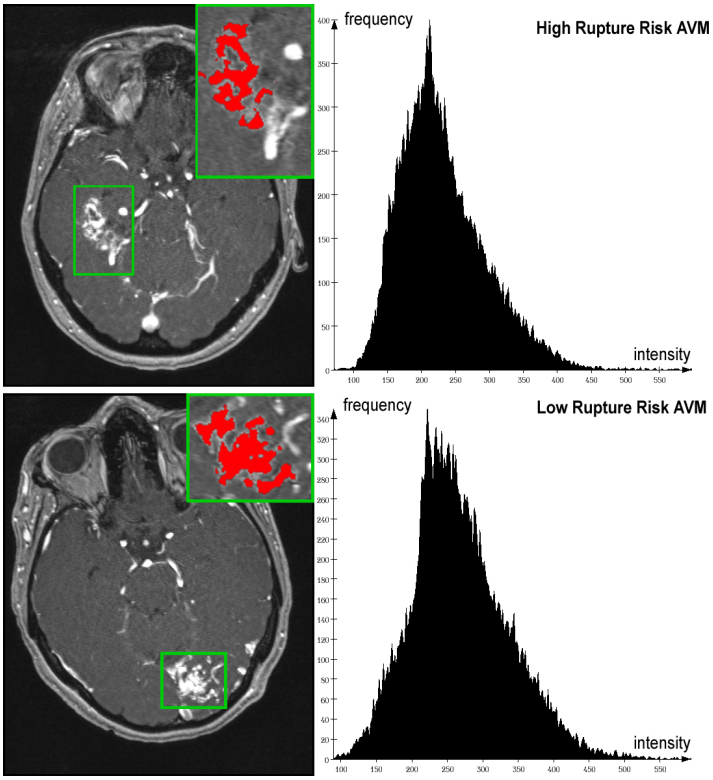

Figure 4.1: Selected slices from TOF datasets of patients with presumably high (top) and low rupture risk (bottom) with magnified delineated AVM nidus (green boxes) and corresponding histograms.

risk (HRR) group in case of a deep nidus location, presence of an exclusive deep venous drainage, previous rupture events or a combination thereof. The remaining patients were classified into the low rupture risk (LRR) group. Parameter-wise t-tests of the histogram parameters were performed to test for significant differences between the groups. Overall, 21 patients were classified to the HRR and 29 patients to the LRR group. The statistical analysis revealed significant differences between these two groups regarding the skewness parameter (p=0.0005). More precisely, the TOF intensity distribution of the HRR AVMs exhibited higher skewness values, which could, for example, be explained by a higher intranidal flow heterogeneity caused by turbulent flow conditions (see Fig. 4.1).
In conclusion, the results of this study imply that the intranidal flow plays an important role in the emergence of an AVM related hemorrhage.
The study design as well as the corresponding results are described in more detail in the appendix D.1.

Although the described first study revealed different intranidal blood flow situations between AVM with a presumably high rupture risk and those with a presumably low rupture risk, two limitations of this study have to be highlighted. First, the TOF in-

tensity distribution is only an indirect measure of the intranidal blood flow situation, such that it is unsolved if the contrast agent or the actual flow properties represents the cause for the identified differences. Second, it remains unclear from this study to which extent the three used risk factors contribute to these findings.
Therefore, the aim of the second study was to independently analyze the association of cerebral hemodynamics with each morphological rupture risk factor in more detail using 4D MRA image sequences [Illies et al., 2012]. Overall, 72 patients were available for this continuing study. Each patient dataset was rated regarding the presence of the following morphological rupture risk factors: a previous intracranial hemorrhage, a deep nidus location, an infratentorial nidus location, a deep drainage, an associated aneurysm, a small nidus size, a draining venous stenosis, and one or two/three draining veins. In a following step, a neuroradiologist defined the main feeders and draining veins of each AVM in the 4D MRA image sequences as well as the corresponding vessels in the contralateral hemisphere. The corresponding concentration time curves for each defined vessel structure were extracted from the 4D MRA image sequences and used for estimating the time-to-peak parameter employing the developed reference-based linear curve fitting approach (see section 3.2.1). Finally, the relative AVM nidus transit time was calculated for each patient based on the estimated time-to-peak values. A multiple normal regression analysis was performed for identifying the risk factors, which are associated to altered blood flow transit times through the AVM nidus. More precisely, the multiple normal regression model was fitted to the data with stepwise selection of all risk factors as regressors.
The statistical analysis revealed that a previous hemorrhage is the only AVM rupture risk property, which leads to a measureable and significant alteration of the intranidal blood flow. More precisely, a previous hemorrhage increases the intranidal blood flow transit time by 2.4 seconds (95% CI: 1.2 - 3.6 s, $p<0.001$).
In conclusion, a previous AVM rupture is the only property that has been associated to an increased rupture risk, which leads to a significant and permanent alteration of the hemodynamic situation.
The design of this second study as well as the corresponding results are described in more detail in the appendix D.2.

4.1.2 Analysis of the Steal Effect

As highlighted in the introduction of this section, the high-flow condition of AVMs has not only been associated with the remodeling of AVM draining veins but also with the so-called steal effect. The concept of the steal effect assumes that the low-resistance condition of AVM structures leads to a flow diversion away from the adjacent brain parts leading to a spatially restricted hypoperfusion. So far, only a few studies have been presented analyzing the steal effect with different imaging modalities and contradictory outcomes (e.g. [Takeuchi et al., 1994, Guo et al., 2004]).
Therefore, a new study investigating the steal effect was performed within the context of this work using pulsed arterial spin labeling (pASL) MR image sequences (see section 2.2.4) for quantification of the cerebral blood flow [Fiehler et al., 2009]. Overall, 20

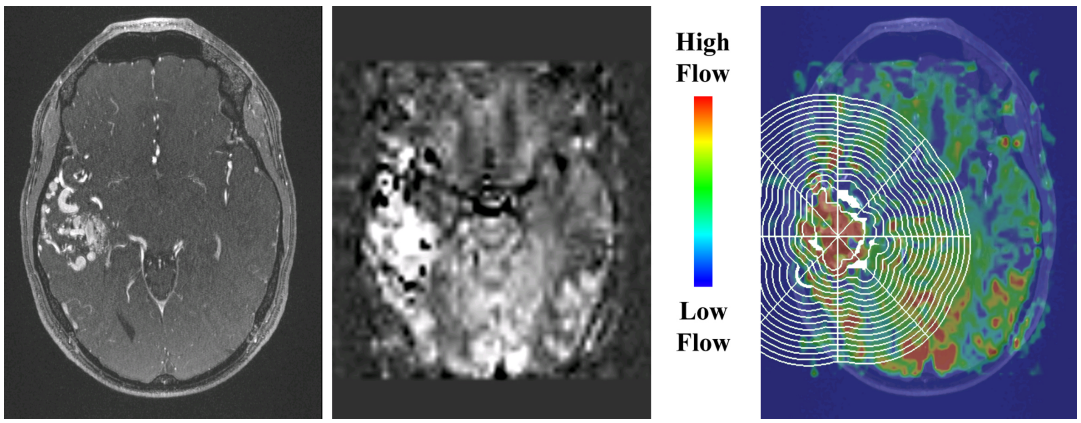

Figure 4.2: Selected slice from a TOF MRA image sequence (left), corresponding slice from the registered pASL image sequence (center), and color-coded overlay of the perfusion values and generated segment model used for analysis of the steal effect (right).

datasets of patients with an arteriovenous malformation were available for this study. Among others, 3D time-of-flight MRA, 4D MRA and 3D pASL image sequences were acquired for each patient in this study group. Briefly described, the cerebrovascular system was extracted from each TOF dataset and used for a manual definition of the AVM nidus. This nidus segmentation was then used for automatically computing a 3D shell model by morphological dilatation of the defined AVM nidus. This 3D shell model was further subdivided into 16 segments (see Fig. 4.2) such that single segments could be excluded from the statistical analysis. Furthermore, the 4D MRA image sequence was used for calculation of a relative bolus arrival time parameter map using the reference-based linear curve fitting approach (see section 3.2.1). The pASL as well as the calculated bolus arrival time parameter map were registered to the TOF image sequence to enable a combined analysis of all datasets. The generated 3D shell model was used to calculate the mean perfusion values for each shell and corresponding segments based on the registered pASL image sequence, whereas voxels part of the cerebrovascular segmentation were excluded from this average calculation. After this, a mean perfusion value was available for each segment and shell with increasing distance to the nidus. A reduction of more than 20% of the mean perfusion values in comparison to the baseline level was assumed to indicate a perinidal dip (hypoperfusion caused by the steal effect). Using the described method, a quantitative global perinidal perfusion dip was identified in five patients (ranging from 37% to 78%), whereas 17 patients exhibited at least a minor locally restricted hypoperfusion. Furthermore, a negative correlation of the territorial perfusion with the relative bolus arrival time ($R = -0.402$, $P = 0.015$) was found. However, no correlation with clinical symptoms could be identified.
In conclusion, the results of this study suggest that most AVMs cause a global or at least a locally restricted perfusion impairment. However, more datasets need to be analyzed for an in-depth evaluation of possible correlations to clinical symptoms.
The design of this AVM steal effect study as well as corresponding results are described in more detail in the appendix D.3

4.1.3 Computer-Aided Angiographic Characterization of Arteriovenous Malformations

Based on the examples for clinical applications of the developed methods for the image-based analysis of arteriovenous malformations given above, it is obvious that the segmentation of the AVM nidus as well as the definition of its feeders and draining veins is most relevant for research settings. Apart from this, a definition of the AVM nidus and angiographic characterization of the vessels in the close vicinity is also important for planning of an AVM therapy. However, the manual definition of these structures may be very time-consuming as well as error-prone. Thus, a computer-aided segmentation of the AVM nidus and following analysis of nearby vascular structures may improve and speed-up clinical decision making, therapy planning, and image-based research projects of arteriovenous malformations.
Therefore, a novel method for the computer-aided segmentation of the AVM nidus and hemodynamic characterization of its feeding arteries and draining veins was developed in this work [Forkert et al., 2013b]. The angiographic characterization of vessel structures requires a previous segmentation of the AVM nidus. For this purpose, the cerebrovascular system is segmented in a first step from a given 3D TOF MRA dataset using the segmentation procedure described in section 3.1. This cerebrovascular segmentation is then employed for an estimation of the vessel diameters using a 3D centerline extraction method [Lee and Kashyap, 1994] followed by a 3D distance mapping approach [Danielsson, 1980]. Furthermore, the vesselness and blobness filters [Sato et al., 1998] are used to enhance bright tubular and blob-like structures in the 3D TOF MRA image sequence. After this, four feature values are available for each voxel of the cerebrovascular segmentation (TOF intensity, vessel diameter, blobness value and vesselness value). These values are used for a classification of each voxel of the cerebrovascular segmentation into the nidus or non-nidus vascular structure group using a support vector machine (SVM) [Joachims, 1999]. The result of this classification is a prediction parameter dataset, in which each vessel voxel is assigned a new value representing the distance to the separating SVM hyperplane. Voxels that are part of the AVM nidus are represented by high positive values in this parameter dataset, which enables a nidus segmentation using 3D volume growing. Due to the fact that the resulting nidus segmentation underestimates the real nidus volume, morphological dilatation is performed in a post-processing step. After segmentation of the nidus, an angiographic characterization of the vessels in the close vicinity of the nidus becomes possible by additionally analyzing 4D MRA image sequences. More precisely, the time-to-peak (TTP) parameter map is calculated first using the reference-based linear curve fitting approach (see section 3.2.1) and registered to the TOF MRA dataset using the method described in section 3.3.1. After this, the mean TTP of the segmented AVM nidus can be calculated and used for definition of feeding arteries and draining veins. Therefore, the TTP of each voxel of the remaining non-nidus vessel structures within the volume-of-interest is compared to the mean AVM nidus TTP. If the TTP of a voxel is shortened compared to the mean nidus TTP, the voxel is classified as a feeding artery. Otherwise it is classified as a draining vein. After post-processing for reduction of outliers, the angiographic characterization

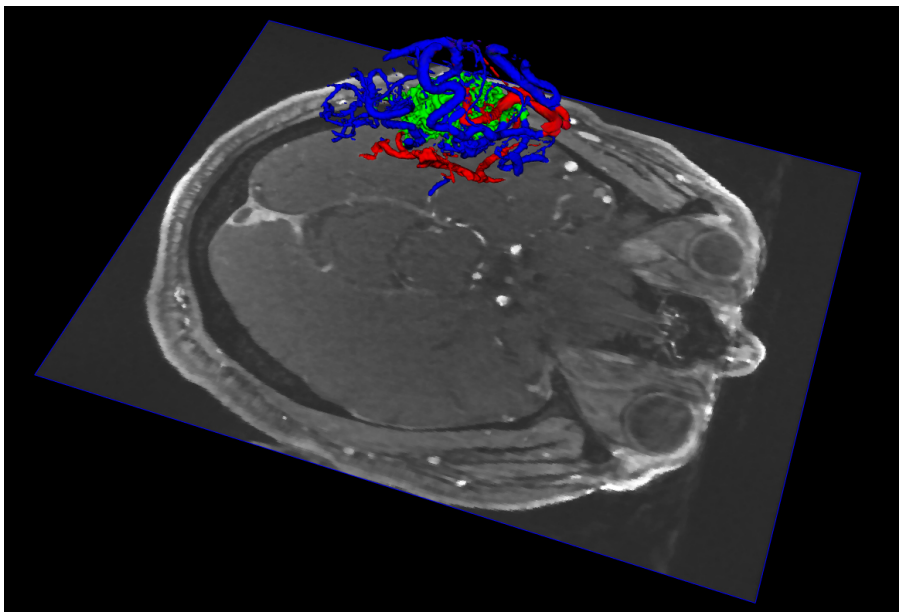

Figure 4.3: Visualization of the angiographic vessel characterization of a patient with an arteriovenous malformation with segmented nidus (green), feeding arteries (red), and draining veins (blue).

can be displayed color-coded in 3D (see Fig. 4.3).
The proposed method was evaluated based on 15 datasets of patients with an arteriovenous malformation. Each dataset consisted of a 3D TOF MRA dataset and a 4D MRA image sequence. The AVM nidus was segmented in each TOF MRA dataset by two observers using an interactive drawing tool and the automatically extracted cerebrovascular segmentation as basis. Leave-one-out cross validation was performed for evaluation of the semi-automatically extracted nidus segmentations. More precisely, all datasets were used for the voxel-wise training of the support vector machine except for the actual dataset to be evaluated. The Dice similarity metric was used for quantitative comparisons of the manual and semi-automatically extracted nidus segmentations. Overall, a mean Dice coefficient of 0.830 (ranging from 0.683 to 0.976) was calculated for the inter-observer agreement. Compared to this, the computer-aided method led to nidus segmentation results with a mean Dice coefficient of 0.835 (ranging from 0.731 to 0.968). The outcome of the automatic angiographic characterization was visually evaluated for each patient dataset, whereas the results of this characterization were judged feasible for all patients.
In summary, the proposed method enables a fast and reproducible computer-aided segmentation of the AVM nidus, whereas the subsequent automatic angiographic characterization seems especially helpful for planning of neurosurgeries and endovascular treatments.
A more detailed description of this computer-aided AVM analysis method and results of the corresponding evaluation are given in the appendix D.4.

4.2 Model-Based Analysis of Aneurysms

Cerebral aneurysms occur usually at weak points in the wall of an artery, which bulge outward and fill with blood. This bulge is called aneurysm. Such an aneurysm may ultimately rupture, which results in a spilling of blood into the surrounding subarachnoid space or brain tissue. Based on a review of 68 studies consisting of 83 study populations, the prevalence of aneurysms was estimated as high as 3.2% in a population without comorbidity [Vlak et al., 2011].
Several factors have been associated with the formation and growth of aneurysms in the past, whereas the true reasons for the pathogenesis and etiology of aneurysms are still not well understood. Among others, factors that have been associated with aneurysm evolution comprise a congenital weakness of the vessel wall, atherosclerosis and hemodynamic factors such as an increased arterial blood pressure and altered intravascular flow conditions [Forsting and Wanke, 2008]. It is generally accepted that aneurysm growth leads to a decrease of the vessel wall strength. Similar to arteriovenous malformations, this weakening may end up in a rupture and intracranial hemorrhage. Based on a review of 9 studies, which included 3907 patients, the overall annual risk for an aneurysm-related hemorrhage was determined at 1.9% [Rinkel et al., 1998]. However, the annual risk for a rupture is increasing with age. Similar to AVMs, a previous hemorrhage increases the risk for rebleeding to 30-50% within the first three months if the aneurysm remains untreated [Beck et al., 2006].
The main goal of aneurysm therapy is to prevent bleeding or rebleeding. This can be achieved by isolating the aneurysm from the systematic blood flow circulation, which subsequently leads to a reduction of the stress that acts on the weakened vessel wall. There are two main strategies for treatment of aneurysms: the endovascular approach using detachable-coils and the neurosurgical approach with craniotomy and clipping [Molyneux et al., 2005, Fiehler, 2012].
Clipping is a neurosurgical procedure in which a skull trepanation under general anesthesia is performed. After this, the aneurysm is approached in the subarachnoid space under microscopic guidance. Once the aneurysm has been located and reached, a small titanium clip is placed along the neck of the aneurysm.
Both procedures bare specific risks for the patient. However, a randomized comparison of endovascular and surgical management of ruptured aneurysms has shown significantly improved clinical outcome in patients treated with coils [Molyneux et al., 2005]. Therefore, most aneurysms are nowadays treated endovascular. Here, the main idea is to advance a catheter from the patient's femoral artery up to the location of the aneurysm in the head under fluoroscopy. Once the aneurysm is reached by the catheter, a thin platinum wire is released inside the aneurysm. As more wire is released into the aneurysm, it curls up and thus fills the aneurysm. Although this intervention could be performed without general anesthesia, most clinical centers treat under general anesthesia to reduce complications due to patient movement. The detached coil is supposed to lead to a clot development, which ultimately results in a major reduction or complete elimination of the blood flow inside the aneurysm. Coils are available in various shapes and sizes.

Multiple coil deployments are usually necessary for a successful blood flow reduction. The number and size of coils used for the procedure is typically estimated during the endovascular treatment or using previously acquired 3D angiographic datasets based on measurements of the aneurysm diameter, the diameter of its neck to the adjacent vessel and the manual "feeling" of increasing resistance while inserting the coils into the aneurysm.
A major concern of endovascular treatment is the possibility of reopening of a coiled aneurysm and the necessity of retreatment with its inherent risks and costs. Such a recurrence is characterized by an anew blood flow circulation, which occurs in most cases in the neck region of the coiled aneurysm. It is commonly assumed that these recurrences develop due to a compaction of the coil-mesh or further growth of the target aneurysm. Previous studies have shown that 6 to 33% of all aneurysms develop a recurrence with a required retreatment in 4.7 - 12.3% of all cases [Ries et al., 2007]. Apart from the increased costs of retreatments for the health care system, this also bares anew treatment and bleeding risks for the patient.
These issues have raised the question whether other materials than bare platinum coils show better performance in terms of less recurrence developments. Various modifications to standard platinum coils such as biologically active surfaces or coated coils with a swelling hydrogel [Kallmes and Fujiwara, 2002] have been developed and brought to clinical use. Every new coil is proposed to lead to an improved packing density and, thus, to less recurrence developments.

4.2.1 3D Computer-Aided Measurements of Cerebral Aneurysms

As described in the introduction of this section, measurements of the aneurysm dome and neck diameter are typically performed for estimating the number and size of coils for endovascular therapy. Several image sequences can be used in the clinical routine to perform the required diameter measurements. Among others, these imaging modalities comprise digital subtraction angiographies, which are typically acquired during the treatment procedure, or other image sequences that are acquired prior to endovascular treatment such as CT angiography, contrast-enhanced MRA or time-of-flight MRA image sequences. Apart from planning an endovascular treatment, these two diameter parameters are also frequently used as stratification variables in clinical trials. The accurate and reliable measurement of aneurysm diameters is, therefore, most important for the clinical routine as well as for clinical trials. However, inter- and intra-observer reliability of aneurysm diameter measurements in different imaging modalities may vary considerably, which could be improved by computer-aided 3D measurements.
Therefore, a computer-aided 3D aneurysm diameter measurement method was developed within the context of this work, which was then evaluated in a study investigating the inter- and intra-observer reliability of 2D and 3D aneurysm diameter measurements in three different imaging modalities [Groth et al., 2013]. Overall, 21 datasets of patients with untreated aneurysms were available for this purpose. Digital subtraction angiographies from different view angles, 3D contrast-enhanced MRA (see section 2.2.2) and 3D time-of-flight MRA datasets (see section 2.2.1) were available for each patient. Manual

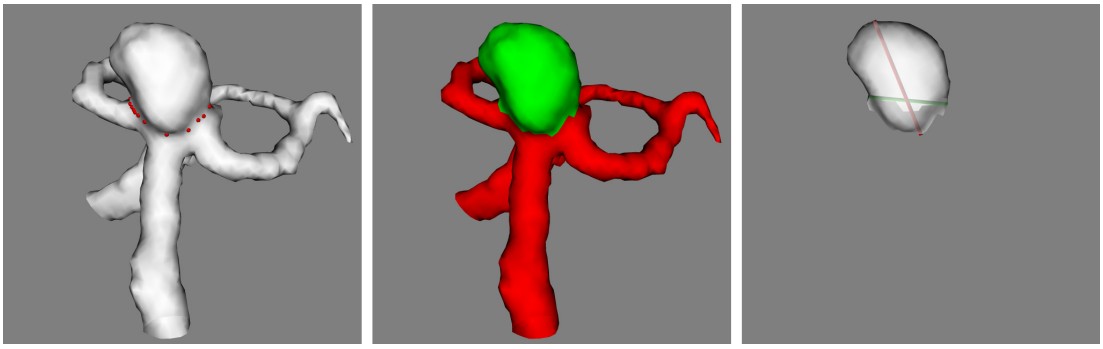

Figure 4.4: Computer-aided aneurysm measurement: Generated 3D surface model of an aneurysm (left) with interactively defined neck (red points), separated aneurysm body (center - green), and corresponding largest neck (green line) and dome (red line) diameters (right).

measurements of the aneurysm neck and dome diameters were performed in each imaging modality based on 2D projections of the datasets. 3D computer-aided aneurysm measurements were performed for the 3D contrast-enhanced MRA and 3D time-of-flight MRA datasets. Briefly described, the cerebrovascular system is automatically segmented from the 3D MRA dataset in a first step using the developed segmentation procedure (see section 3.1) and employed for generating the corresponding 3D surface model. Using this 3D vascular model, the neck of an aneurysm can be defined interactively in 3D by placing points on the 3D surface model. The maximal neck diameter can be estimated from the placed aneurysm neck points in 3D by pairwise calculating the Euclidean distance. In a following step, the placed points are used for a separation of the aneurysm body from the adjacent vessel. After this, the maximal dome diameter can be calculated from the separated aneurysm surface model by pairwise calculation of the Euclidean distance of all surface points.
All 2D and 3D measurements were performed by two observers with several years of dedicated experience in neuroradiology, whereas one observer performed the measurements twice with a temporal delay of 4 weeks between the readings. The statistical analysis of the aneurysm diameter measurements was performed using the intra-class correlation coefficient (ICC) as well as Bland-Altman analysis [Bland and Altman, 1986]. Overall, the inter- as well as intra-observer correlation coefficients for the 3D measurements using the TOF and CE MRA datasets of the aneurysm neck and dome diameters were 0.92 or higher. In contrast to this, considerably lower ICCs were found for the corresponding 2D aneurysm diameter measurements (ranging from 0.28 to 0.89). This finding was further confirmed by the Bland-Altman analysis, which revealed marked higher 95% limits of agreement for the 2D measurements. Overall, the 3D measurements resulted in larger diameters compared to the 2D measurements, which seems reasonable as the maximal diameters were calculated in 3D. This was also confirmed by 3D measurements of a physical phantom dataset displaying five contrast-media-filled tubes with known diameters (5, 10, 13, 16 and 20 mm). The results of this phantom dataset evaluation revealed errors of the 3D measurements ranging from 0.02 to 0.5 mm, which is in the range of voxel accuracy.

In summary, the results of this study suggest that the 3D measurement of the aneurysm neck and dome diameter leads to a reproducible parameter extraction, which may be used in the clinical routine and as an objective surrogate end-point for clinical trials. The developed 3D aneurysm measurement method as well as the corresponding evaluation and results are described in more detail in the appendix E.1.

4.2.2 Image-Based Aneurysm Recurrence Quantification

The formation of aneurysm blood flow recurrence volumes after endovascular treatment is a major drawback of the coil therapy procedure. Such an occurrence may imply a retreatment, which is associated to further complication risks for the patient as well as increased costs for the health care system. Due to these reasons, more and more new coils are currently developed, which are supposed to decrease the probability of a recurrence development. However, the clinical benefit of these new coils is questionable and large patient cohorts are required to statistically prove the superiority of one coil against another one using visual assessments of binary endpoints (e.g. recurrence yes / no). A clinical evaluation of new coils is therefore not only expensive but also time-consuming. In the worst-case scenario, several hundred patients might have been treated with a new coil, which turns out to perform worse compared to conventional coils. Replacing the binary endpoints by a continuous variable may result in a higher statistical power and, therefore, in smaller study groups required for the evaluation of new coils.
The goal of replacing the binary endpoints by a continuous variable was achieved in this work by quantitatively measuring the recurrence volume. However, this requires at least two 3D MRA datasets acquired at two time points after therapy. The first 3D MRA image sequence (baseline) should be acquired shortly after therapy while the second dataset should be acquired 6-12 month after therapy (follow-up). The quantitative assessment of a possible recurrence volume requires a rigid registration of the two datasets to correct for different spatial resolutions and patient positions within the scanner. The registration leads to a voxel-correspondence of the baseline and follow-up MRA image sequences, which enables a definition of recurrence volumes. More precisely, a recurrence volume is characterized by voxels exhibiting low intensities in the baseline MRA dataset and high intensities in the registered follow-up image sequence.

Two different methods were developed in this work for the quantification of recurrence volumes [Säring et al., 2012]. Both methods have in common that a rigid registration of the two datasets is performed. However, these two methods differ with respect to the integration of the cerebrovascular segmentation in the registration process and recurrence volume quantification.
The first developed method computes the optimal rigid transformation by minimizing the mean squared distance (MSD) of all voxels within a volume-of-interest using the interactively defined aneurysm as the center. After registration, a difference image is calculated by subtracting the baseline from the registered follow-up MRA dataset. The recurrence volume is extracted from the difference image using interactive or computer-aided volume growing techniques.

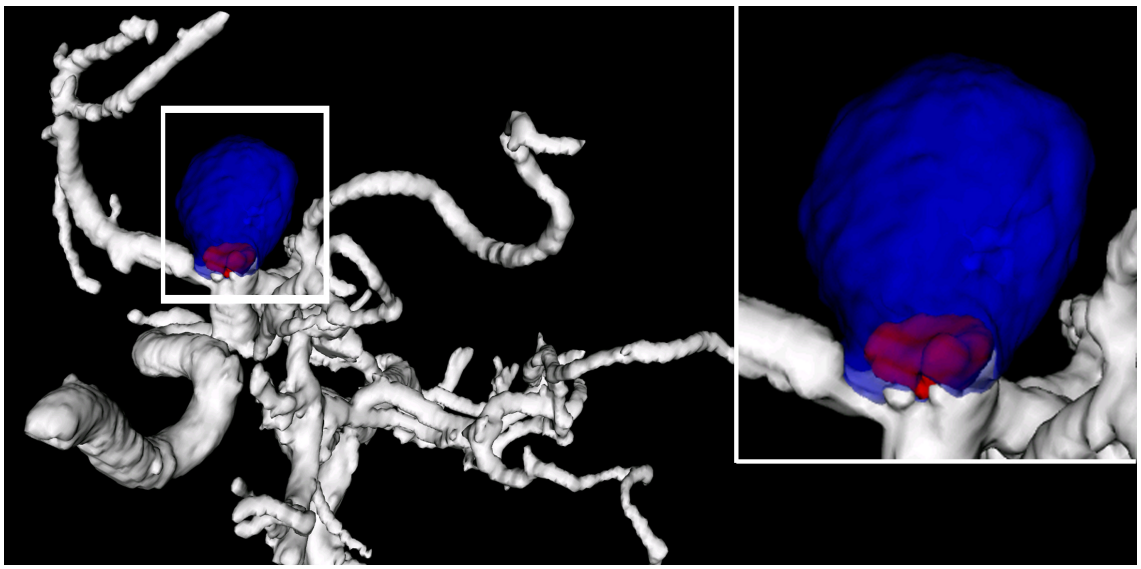

Figure 4.5: 3D surface-based visualization of cerebrovascular system with an aneurysm (transparent blue) and corresponding automatically extracted recurrence volume (red).

The second developed method also computes the optimal rigid transformation by minimizing the MSD. However, this second method employs a masked registration instead of using all voxels within the volume-of-interest. Here, only voxels that are part of the corresponding cerebrovascular segmentation contribute to the calculation of the MSD. Self-evident, this requires a previous segmentation of the cerebrovascular structures from the baseline and follow-up MRA image sequence prior to the registration, which was performed in this work using the segmentation procedure described in section 3.1. After this, the cerebrovascular segmentation of the baseline MRA dataset is subtracted from the cerebrovascular segmentation of the registered follow-up MRA dataset. The recurrence volume can then be quantified by performing a largest connected component analysis of all voxels with a positive value.
Two experiments were performed to evaluate the two developed methods. The first experiment was conducted to analyze the registration accuracy of the two approaches. Therefore, eight synthetic datasets with known transformations of the follow-up MRA image sequences were registered to the corresponding baseline MRA image sequence using the two registration approaches. After this, the calculated transformations were compared to the known ground-truth transformations. Briefly described, the results of this evaluation showed that the integration of the cerebrovascular segmentation leads to considerably better registration results compared to the unmasked registration. The second experiment was performed to evaluate the accuracy of the extracted recurrence volumes by the two methods using 10 datasets with manually defined gold-standard recurrence volumes. In general, the results of this evaluation suggest that the segmentation-based quantification leads to an improved estimation of the recurrence volumes. However, the automatically extracted recurrence volume was only sufficient in 8 of the 10 cases, such that interactive corrections may be necessary.

In summary, the first results of this study suggest that the integration of the cerebrovascular segmentation leads to improved rigid registration results and following reproducible aneurysm recurrence volume estimations.
The two developed aneurysm recurrence quantification methods as well as the corresponding results of the experiments are described in more detail in the appendix E.2.

Both methods described above enable a quantitative assessment of aneurysm recurrence volumes from longitudinal 3D MRA datasets, whereas the solely intensity-based approach requires more manual post-processing of the results. As highlighted earlier, it was hypothesized that the quantitative assessment of recurrence volumes leads to a higher statistical power compared to using only binary endpoints, which may allow evaluating new coils based on considerably smaller study groups.
This hypothesis was tested in a preliminary study using 59 datasets of patients with aneurysms that underwent coil therapy [Ries et al., 2011]. Each patient dataset consisted of at least two time-of-flight MRA datasets, which were acquired at different time points after coil therapy. The solely intensity-based method was used for definition of the aneurysm recurrence volumes since the segmentation-based method was not yet available at the early stage of this study. Therefore, more manual corrections of the extracted aneurysm recurrence volumes were required to obtain satisfying results. After aneurysm recurrence volume definition in each dataset, statistical power calculations were performed for the binary endpoint (recurrence yes/no) as well as for the continuous variable (recurrence volume in μL).
Briefly described, the statistical analysis demonstrated that the usage of the recurrence volume as a continuous variable leads to a possible reduction of the sample size from 948 to only 74 patients to evaluate new coils without loss of statistical power.
In summary, the volumetric analysis of aneurysm recurrence volumes could considerably reduce the sample sizes that are required for the evaluation of new coils. Thus, a more timely assessment of possible benefits of new coils and reduction of the associated costs becomes possible.
The design of this preliminary study and results of the statistical analysis are described in more detail in the appendix E.3.

4.3 Model-Based Analysis of Ischemic Strokes

It is estimated that one out of twenty adults will suffer from a cerebral stroke during lifetime [Feigin et al., 2009]. The ischemic stroke, which is caused by an occlusion of an artery, accounts for approximately 72% of all cerebral strokes [Thrift et al., 2001]. Such a vessel occlusion leads to a partial or even complete restriction of the blood flow supplying the brain tissue and may ultimately result in an irreversible damage of brain cells if normal blood flow is not restored within sufficient time. The blood clots or stenosis, which are responsible for an occlusion in most cases, may have developed locally due to arteriosclerotic changes of the blood vessel (thrombotic stroke) or may have been carried with the blood through the systemic circulation until being lodged at the occlusion site far away from its origin (embolic stroke). There are several factors that have been associated to an increased risk for an ischemic stroke. Among others, these factors include nicotine as well as alcohol consumption, hypercholesteremia, diabetes mellitus, atrial fibrillation, age, gender, and race. However, arterial hypertension has been identified as the most important risk factor for an ischemic stroke [Sacco et al., 1997].
One important concept for diagnosis and therapy of acute ischemic strokes is the definition of the infarct core and its ischemic penumbra [González et al., 2011]. This concept is based on the physiological observation that a blockage of a cerebral artery does not necessarily lead to an immediate irreversible injury of the whole brain tissue supplied by the occluded artery. In many cases, parts of the more peripherally located brain tissue, which is affected by the occlusion, may still be supplied by collateral connections such as the circle of Willis or leptomeningeal collaterals. This collateral circulation may compensate hypoperfusion to some extent. Therefore, the infarct core is defined as the tissue, which is irreversibly damaged and is typically located in the central region of the tissue suffering from insufficient blood supply. In contrast to the infarct core, the so-called penumbra that surrounds the infarct core suffers from hypoperfusion and brain tissue in this zone is dysfunctional and at an increased risk of necrosis. Thus, the ischemic penumbra is not yet irreversibly damaged and therefore potentially salvageable. Unfortunately, the ability of the brain to endure hypoperfusion is limited and it is typically assumed that the infarct core will gradually expand into the penumbra in a dynamic process. This observation has led to the concept of "time is brain" [Saver, 2006], which assumes that a faster recanalization of the occluded vessel leads to an improved tissue and following functional outcome.
The brain tissue in the penumbra of an acute ischemic stroke represents the main target for acute stroke therapy. To achieve recanalization and a following reperfusion, mechanical thrombectomy is one option in a selected group of patients. However, chemical thrombolysis is currently the first-choice therapy in most cases.
Pharmaceuticals used to achieve clot lysis consist of recombinant tissue plasminogen activator (rt-PA) proteins and are typically administered intra-arterial or intravenously via a peripheral blood vessel, i.e. on the upper extremities. The main function of rt-PA proteins is to convert plasminogen to plasmin, which is capable of dissolving blood clots and thus leads to a recanalization of the occluded vessels. However, the use of

rt-PA is associated with several side effects such as an increased risk for intracerebral hemorrhage. As mentioned above, the extent of potentially salvageable brain tissue generally decreases with time from symptom onset. Therefore, the application of rt-PA is only permitted within 3 - 4.5 hours (depending on regional treatment guidelines) after stroke onset [Davis and Donnan, 2009]. Apart from this, thrombolytic therapy may only lead to a successful recanalization in 6-30% of all cases, depending on the occlusion site [Shi et al., 2010].
The mechanical thrombectomy involves the introduction of a catheter into the arterial vasculature proximal to the occlusion site [Brekenfeld et al., 2008]. Once the catheter has reached the occlusion site, a mechanical thrombectomy device is used to remove the clot. One of the main benefits of the mechanical thrombectomy is the improved recanalization success in cases where systemic pharmacological therapy with rt-PA has shown to be less effective (i.e. main stem occlusion of the middle cerebral artery). Furthermore, this therapy can be also applied beyond the clinically approved time window for thrombolytic therapy. The thrombectomy is an interventional procedure that requires not only skilled physicians but also appropriate devices. The fact that these devices are not yet widespread available in all hospitals is the main criterion for exclusion of this therapy. For these reasons, the thrombolytic therapy is still the most frequently applied therapy in case of an acute stroke.

4.3.1 Influence of Hemodynamic Models on Tissue-at-Risk Quantification

Due to the increased risk of hemorrhage, thrombolytic therapy should only be administered if the potential benefits exceed the associated risks. Within this context, the concept of the infarct core and its penumbra has become very important in clinical practice as it is hypothesized that patients with larger penumbra volumes are more likely to benefit from a thrombolytic therapy [Albers et al., 2006]. In clinical practice, the assessment of the penumbra is typically achieved using magnetic resonance or computer tomography (CT) imaging. In MRI, infarcted brain tissue can be displayed and defined in diffusion-weighted MRI datasets (see section 2.2.6). Additionally, the area of hypoperfusion can be defined using perfusion-weighted MRI datasets (see section 2.2.5). The volumetric difference between the two defined lesions is typically used as a surrogate for the ischemic penumbra, which represents the tissue-at-risk and target for the therapy of an acute ischemic stroke. However, the definition of the lesion extent and severity in perfusion-weighted datasets involves the prior calculation of a parameter map, e.g. by the voxel-wise calculation of the time-to-peak parameter based on the concentration time curves (see section 3.2). Therefore, parametric models used for the hemodynamic analysis may crucially influence the resulting volume of the perfusion deficit in perfusion-weighted MR datasets and subsequent tissue-at-risk quantification. However, the influence of hemodynamic models on tissue-at-risk quantification has never been investigated in detail.

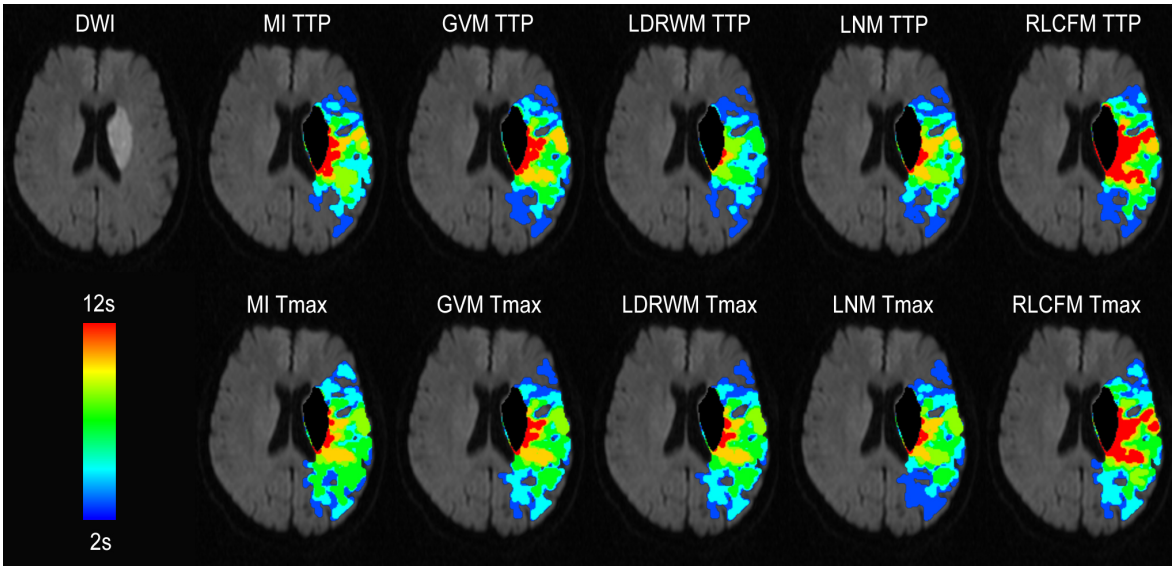

Figure 4.6: Selected slice from a DWI dataset with corresponding DWI lesion (black) and color-coded tissue-at-risk volumes for delay thresholds between 2 and 12 sec calculated using the 10 different TTP/Tmax estimation methods (MI = model independent, GVM = gamma variate model, LDWRM = local density random walk model, LNM = log-normal model, RLCFM = reference-based linear curve fit model).

Therefore, an in-depth analysis of this relation was performed within this work using datasets of 50 acute ischemic stroke patients [Forkert et al., 2013c]. Each dataset consisted of a diffusion-weighted MRI dataset with strong diffusion weighting (see section 2.2.6) for definition of the infarct core as well as a perfusion-weighted MRI dataset (see section 2.2.5) for the analysis of the cerebral perfusion. Overall, the tissue-at-risk volumes resulting from ten different time-to-peak (TTP) and time-to-max (Tmax) estimation methods were evaluated in this study. The TTP parameter is defined as the time when the concentration time curve achieves its peak. In contrast to this, the Tmax parameter is defined as the time when the residue function achieves its peak. The residue function can be calculated by deconvolution of a tissue concentration time curve with an arterial input function, which is usually selected from the contralateral middle cerebral artery. Instead of using the raw concentration time curves for TTP or Tmax estimation, previously fitted hemodynamic model curves can also be employed for this purpose. The following ten TTP/Tmax estimation techniques were used in this study: raw concentration curve TTP and Tmax, fitted gamma-variate model TTP and Tmax, fitted local density random walk model TTP and Tmax, fitted log-normal model TTP and Tmax, as well as the proposed fitted reference-based linear curve fitting model TTP and Tmax (see section 3.2.1). Moreover, temporal delay thresholds between +2 and +12 seconds compared to the contralateral hemisphere were used for definition of hypoperfused tissue (see Fig. 4.6). After definition of the hypoperfused brain tissue using the ten TTP/Tmax estimation methods and different temporal delay thresholds, an additional segmentation of the infarct core is required to quantify the volume of the

tissue-at-risk for each method and temporal delay threshold. For this purpose, the lesion infarct core volume was quantified semi-automatically in each DWI dataset. Therefore, a volume-of-interest (VOI) surrounding the lesion with a generous margin was manually defined in each affected slice in the orthogonal views. A second VOI was then placed in the unaffected tissue in the contralateral hemisphere and used for calculating the mean (μ) and standard deviation (σ) of the signal intensities in the DWI dataset. The initially defined lesion volume-of-interest was then refined by rejecting all voxels with a DWI signal intensity less than $\mu + 2\sigma$. After registration of the TTP and Tmax parameter maps to the corresponding DWI dataset, the volumetric mismatch (tissue-at-risk) between the defined infarct core lesion and corresponding hypoperfused lesion was calculated for each patient applying the ten TTP/Tmax estimation methods and different temporal delay thresholds. A random intercept regression analysis was performed to model the resulting tissue-at-risk volumes from one TTP/Tmax estimation method to another one, such that an artificial adaption of the tissue-at-risk volumes calculated using different TTP and Tmax estimation methods becomes possible.
A comparison of the resulting tissue-at-risk volumes revealed mean volumetric differences up to 40 mL and 100 mL in individual patients between the mismatch volumes calculated by the ten TTP/Tmax estimation techniques for typically used temporal delay thresholds. The application of commonly applied thresholds for definition of a relevant mismatch volume in the clinical routine (temporal delay >6 seconds, mismatch volume >10 mL and mismatch ratio >20%) would have led to different mismatch classification in up to 24% of all cases. A further evaluation revealed that the application of the correction formulas derived from random intercept regression analysis can considerably reduce these differences.
In conclusion, the results of this study suggest that the application and type of hemodynamic models have a crucial impact on the tissue-at-risk quantification, which is also relevant for the clinical practice. An adaption of the different techniques using correction formulas seems feasible to achieve comparable study results until a standard has been agreed upon.
A detailed description of this study analyzing the influence of hemodynamic models on tissue-at-risk volume quantification and corresponding results is given in the appendix F.1.

4.3.2 DWI-FLAIR Mismatch

As mentioned in the introduction of this section, the thrombolytic therapy of acute ischemic stroke patients is only permitted within 3 - 4.5 hours after acute ischemic stroke symptom onset, which is a major drawback of thrombolytic therapy. This is especially problematic in case of patients with unknown time of symptom onset. This applies, for example, in patients with so-called wake-up strokes. Approximately 25% of all strokes occur during sleep [Serena et al., 2003], which leads to the fact that these patients are not eligible for thrombolytic therapy. Due to this reason, increasing effort has been undertaken to identify potential image-based biomarkers for deciding which patients with unknown stroke symptom onset are eligible for a thrombolytic therapy. Within this context,

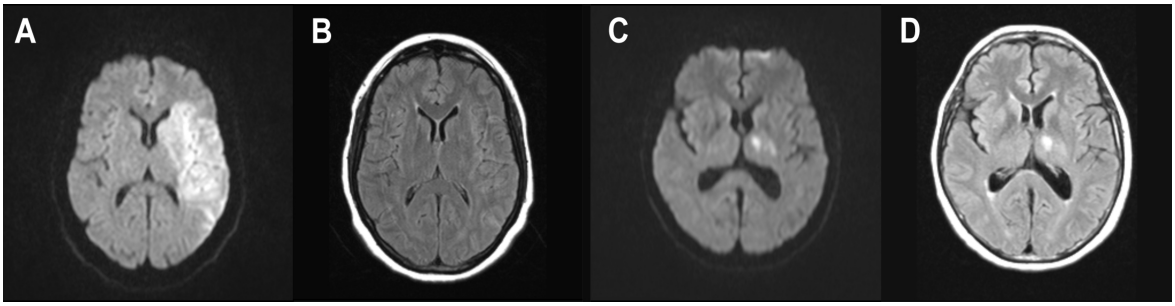

Figure 4.7: Selected slices from DWI MR datasets with strong diffusion weighting of two patients with an acute ischemic stroke (A,C) and corresponding slices from FLAIR image sequences without visible lesion (B) and with visible lesion (D).

the difference in visibility of an acute ischemic lesion between diffusion-weighted (DWI, see section 2.2.6) and fluid-attenuated inversion recovery (FLAIR) MRI (see section 2.2.7) has been suggested as one possible image-based biomarker [Thomalla et al., 2009]. This so-called DWI-FLAIR mismatch concept draws its underlying assumption from the observation that FLAIR imaging is highly sensitive to subacute ischemic strokes but not to acute lesions within the first hours after symptom onset. Therefore, it is assumed that patients exhibiting a lesion, which is visible in the DWI but not in the FLAIR image sequence, are likely to be eligible for thrombolytic therapy (see Fig. 4.7).
This hypothesis was tested within the context of this work based on a large multicenter observational study [Thomalla et al., 2011]. Overall, 543 patient datasets with known time from symptom onset to MRI acquisition from nine contributing centers were available for this study. Each dataset was rated by two experienced observers regarding the presence of a DWI-FLAIR mismatch (lesion is visible in DWI but not in FLAIR image sequence). In case of conflicting judgments, a consensus was reached with a third observer. Furthermore, the infarct core volumes were quantified semi-automatically in each DWI dataset with strong diffusion weighting using the same method as described in section 4.3.1.
Multivariate regression analysis identified a longer time to MRI, lower age, and larger DWI lesion volume as independent predictors of lesion visibility in FLAIR image sequences. Overall, the results of this study revealed that it is possible to identify acute stroke patients within 4.5 hours of stroke onset with a sensitivity of 62%, specificity of 83% and positive predictive value of 83% by applying the described DWI-FLAIR mismatch concept.
In conclusion, the results of this study suggest that the DWI-FLAIR mismatch can identify patients who are eligible for thrombolytic therapy with high specificity and moderate sensitivity.
The design of this multicenter observational study and results of the statistical analysis are described in more detail in the appendix F.2.

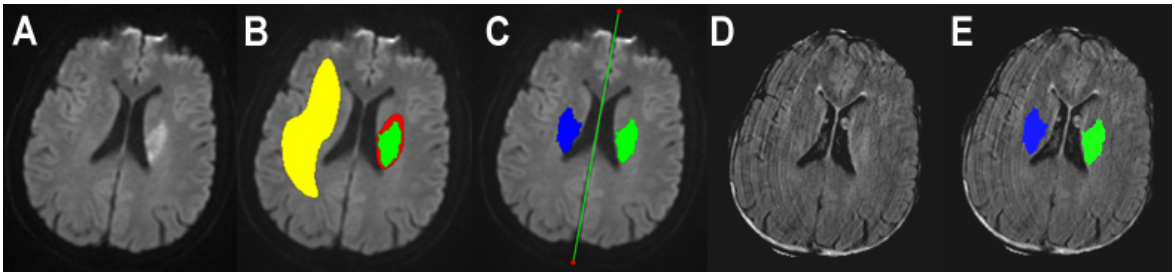

Figure 4.8: Selected slice from a DWI MR dataset with strong diffusion weighting (A), manually defined ischemic lesion (B: red) and healthy reference volume-of-interest (B: yellow) used for definition of the refined lesion segmentation (B: green), defined inter-hemispheric fissure used for mirroring of the refined lesion segmentation onto the healthy hemisphere (C: blue), corresponding slice of the registered FLAIR image sequence (D), and overlaid volume-of-interests for relative FLAIR measurements (E).

The results of the study described above demonstrated that the application of the DWI-FLAIR mismatch concept allows identifying patients eligible for thrombolytic therapy with high specificity (78%) but rather low sensitivity (62%). Furthermore, the inter-observer agreement for the visual assessment of this DWI-FLAIR mismatch was only moderate (Kappa $\kappa = 0.569$). Quantitative analyses of the DWI-FLAIR mismatch may enable an improved identification of patients eligible for thrombolytic therapy. However, FLAIR imaging does not allow direct quantitative analyses as the resulting image sequences depend to a large extent on the imaging parameters, especially the inversion time parameter (see section 2.2.7). Therefore, a quantitative assessment can only be performed in terms of relative measurements.
The possible benefit of such relative measurements were evaluated in a secondary analysis of the available database [Cheng et al., 2013]. To enable such a semi-quantitative measurement, the FLAIR dataset needs to be registered to the corresponding DWI dataset of the same patient. This was achieved in this work using a rigid transformation, maximization of the mutual information and linear interpolation. In a following step, the infarct core was semi-automatically segmented in each DWI dataset using the same method as described in section 4.3.1. In contrast to the previous study, this infarct core segmentation was not only used for a quantification of the lesion volume but also for a projection onto the contralateral hemisphere, which is required for the semi-quantitative assessment of the DWI-FLAIR mismatch (see Fig. 4.8). This was achieved by manually defining the inter-hemispheric fissure by straight lines in two axial slices as distant as possible. More precisely, a 3D plane was constructed from the two defined lines, which was then used for mirroring the lesion segmentation onto the contralateral hemisphere. After this, the mean FLAIR signal intensities were determined for the infarct core segmentation as well as for the mirrored infarct core segmentation and the corresponding FLAIR ratio was calculated from these two average FLAIR signal intensities (infarct core / mirrored infarct core segmentation).

It is obvious that this quantitative procedure reduces the problem of the observed low inter-observer agreement associated with the visual rating. However, statistical analysis revealed that the FLAIR signal intensity ratios are only moderately correlated with the time from symptom onset ($r=0.382$, $p<0.001$). Apart from this, statistical analysis also revealed that the usage of quantitative FLAIR signal intensity ratios lead to an improved specificity of 85% but also to a decreased sensitivity of 47% for the identification of patients eligible for thrombolytic therapy compared to the described visual assessment.
In summary, the results of this study raise doubts if the measurement of quantitative FLAIR signal intensities enables an improvement identification of patients who are eligible for thrombolytic therapy.
The design of this study and results of the statistical analysis are described in more detail in the appendix F.3.

As highlighted in the first part of this section and also in more detail in the appendix F.1, the acute perfusion deficit is frequently used to obtain a prediction of the final tissue outcome in acute stroke patients. However, it remains unclear if the FLAIR signal is also influenced by the situation of the cerebral perfusion. Therefore, the cerebral perfusion may also be an important independent predictor of lesion visibility in FLAIR image sequences.
This question was studied in more detail using 48 datasets of patients with an acute ischemic stroke [Cheng et al., 2012]. Each patient dataset consisted of a diffusion-weighted MRI dataset, a perfusion-weighted MRI dataset (see section 2.2.5) as well as a FLAIR image sequence. The FLAIR image sequences were rated in a first step by four observers in consensus regarding the visibility of a lesion. Relative time-to-peak parameter maps were calculated based on the corresponding PWI datasets and used for quantification of the hypoperfused brain volume using a temporal delay threshold of >4 seconds (see section 4.3.1). Furthermore, the infarct core was semi-automatically segmented in each DWI datasets using the same method as described in section 4.3.1. After registration of the time-to-peak parameter maps to the corresponding DWI datasets, the median time-to-peak value within the segmented infarct lesion was calculated for each patient.
A Mann-Whitney U test was used for group comparisons between the FLAIR-positive and FLAIR-negative infarct lesions. Briefly described, the results of this study revealed no significant differences between FLAIR-positive and FLAIR-negative infarct lesions regarding the median time-to-peak value or volume of the hypoperfused brain tissue.
Thus, it can be concluded that the lesion size and age influence the visibility of FLAIR lesions, but not the extent or severity of hypoperfusion.
The design of this study and results of the statistical analysis are described in more detail in the appendix F.4.

As described in section 2.2.7, fluid-attenuated inversion recovery (FLAIR) MRI is a T2-weighted imaging sequence. Therefore, it is sensitive to the uptake of water in brain tissue over time, which is a characteristic feature of ischemic brain infarction. However, it remains an open question if the corresponding hyperintensities seen in FLAIR and

T2-weighted images are reversible or could even be used as predictor of tissue outcome beyond the perfusion-diffusion mismatch (see section 4.3.1).
For this reason, a further study was performed, which aimed at investigating quantitative T2 values in different regions of acute ischemic strokes [Siemonsen et al., 2012]. Overall, datasets of 22 patients with an acute ischemic stroke were available for this purpose. Among others, each dataset consisted of a diffusion-weighted MR dataset obtained with three different b-values, a perfusion-weighted MR dataset and a triple-echo T2 MR image sequence (see section 2.2.8). All datasets were acquired within 6 hours after symptom onset. Furthermore, a follow-up FLAIR image sequence was available for each patient, which was acquired 5 to 9 days after symptom onset. In a first step, quantitative T2 parameter maps were calculated for each patient from the triple-echo T2 MRI dataset. Furthermore, the apparent diffusion coefficient (ADC) map was calculated for each patient based on the DWI image sequence acquired using three different b-values (see section 2.2.6). After calculation of the ADC map, the infarct core was segmented in this parameter map using thresholds techniques. Moreover, the brain tissue exhibiting hypoperfusion was segmented from the time-to-peak maps, which were calculated model-independently from the PWI datasets, applying a delay threshold of >4 seconds (see section 4.3.1). The volume of the final infarct outcome was manually delineated in each follow-up FLAIR image sequence. Finally, the PWI, DWI and follow-up FLAIR datasets were registered to the corresponding dataset of the tripe-echo T2 image sequence with the highest echo time. Thus, a transformation of all lesion segmentations to the corresponding quantitative T2 parameter dataset and following analysis of the corresponding quantitative T2 values in all defined lesions becomes possible. More precisely, three volumes-of-interest (VOIs) were generated based on the registered lesion segmentations: the acute infarct core lesion VOI, a lesion growth VOI (final infarct outcome segmentation excluding the infarct core lesion VOI) and a surviving tissue VOI (hypoperfused brain tissue segmentation excluding the two other VOIs). These three VOIs were employed for calculating the corresponding mean quantitative T2 values in each region and patient, which were then used for statistical analysis.
The results of the statistical analysis revealed no significant differences between the quantitative T2 values in the lesion growth VOI and surviving tissue VOI. Overall, the results of this study even indicate that quantitative T2 values in different brain regions, which are associated to cerebral infarction, exhibit a further increase of quantitative T2 values beyond the acute phase.
In conclusion, the results of this study suggest that T2 values are not suitable for a prediction of final infarct outcome.
The design of this study and results of the statistical analysis are described in more detail in the appendix F.5.

Chapter 5

Outlook

The main contributions of this work from a methodical perspective are the development of a novel framework for the automatic cerebrovascular segmentation from high resolution magnetic resonance angiographies (see section 3.1), a new method for estimating the bolus arrival time from concentration time curves derived from perfusion-weighted MR datasets and time-resolved magnetic resonance angiographies (see section 3.2), as well as the combined analysis of 3D and 4D MRA image sequences in terms of the presented 4D blood flow visualization (see section 3.3). All methods have been implemented in the software tool AnToNIa (Analysis Tool for Neuro Imaging Data), which has been developed within the scope of this work. This software tool offers an intuitive graphical user interface and is currently used by the Department of Neuroradiology and the Department of Neurology at the University Medical Center Hamburg-Eppendorf for various clinical and research questions (see chapter 4).

At this point, the developed dynamic blood flow visualization seems especially helpful for rating patients with an arteriovenous malformation, which usually exhibit a rather large pathological nidus with a highly complex anatomy and blood flow situation. However, it has been shown in section 3.3.1 and 3.3.2 that the spatial resolution of the underlying 4D MRA sequences remains the bottleneck for this visualization such that the blood flow can only be displayed at proper quality for vessel structures with a diameter that exceeds the spatial resolution. This limitation can be overcome to some extent by lowering the temporal resolution, which leads to an improved spatial resolution, since it was demonstrated in section 3.2.2 that a temporal resolution of 1.5 seconds is sufficient for the hemodynamic analysis. Apart from this, 4D MRA image sequences with improved spatial as well as temporal resolution, which are currently developed, may also proof valuable for this purpose. At this point, especially 4D image sequences that utilize arterial spin labeling techniques (see section 2.2.4) [Bi et al., 2010] seem promising for this purpose. However, concentration time curves derived from these 4D arterial spin labeling MRA techniques do not exhibit the typical shape of indicator dilution curves obtained from image acquisitions using common contrast agent media. Due to this reason, typical parametric models for curve fitting, e.g. the gamma variate function, cannot be applied to these curves. In this context, an application of the proposed reference-based linear curve fitting model for bolus arrival time estimation (see section 3.2.1) may proof even more valuable, as it is a major benefit of this approach that no explicit assumption about the shape of typical indicator dilution curves is made. Therefore, an application

of the presented methods for bolus arrival time estimation and subsequent 4D blood flow visualization to these new image sequences may open doors to a proper blood flow visualization of patients with cerebrovascular diseases other than arteriovenous malformations. Thus, it may even be possible to analyze and visualize the blood flow within small aneurysms and obtain a more detailed knowledge about the intranidal blood flow in case of arteriovenous malformations. Up to the present, these novel non-contrast dynamic MRA image sequences have only been evaluated visually, e.g. for arteriovenous malformations [Yu et al., 2012]. However, an analysis of this imaging technique beyond the visual rating of vascular pathologies has not been performed yet and is one focus of continuing research projects. Furthermore, the development of improved 4D flow-sensitive phase contrast (4D flow) MR image sequences may also proof beneficial for the diagnosis and general understanding of cerebrovascular malformations. Phase contrast imaging has been used for several years for clinical purposes, especially to obtain knowledge about the direction and velocity of blood flow. The main principle of phase contrast imaging is to apply oppositional aligned gradient pulses in x-, y- and z-direction. In doing so, resting spins receive no phase shift while flowing spins receive a phase shift that is proportional to the blood flow velocity. 4D flow imaging combines phase contrast with so-called CINE MRI principles. Here, the main idea is to synchronize the phase contrast image acquisition with the electrocardiogram over many heart cycles [Markl et al., 2007]. Therefore, this imaging technique renders the possibility to obtain information about the blood flow velocity and direction in terms of streamlines at the different cardiac stages. 4D flow imaging has been successfully applied and proven beneficial for patients with a stenosis [Hope et al., 2010], aneurysms [Jiang et al., 2011], and arteriovenous malformations [Hope et al., 2009]. Thus, it may be interesting to also apply this technique for two problems, which were in the focus of this work. First, using this MR acquisition technique it may be possible to obtain a deeper insight into the intranidal blood flow in case of arteriovenous malformations and to repeat the analysis investigating the association of rupture risk factors with blood flow properties described in section 4.1.1 in more detail. Second, it may be interesting to relate information about blood flow velocity and stream lines to the formation of aneurysm recurrence volumes after coil therapy (see section 4.2.2). In particular, this may be relevant since not much is known about the influence of blood flow properties to the development of aneurysm recurrence volumes. In both cases, it may be also interesting to perform blood flow simulations using computational fluid dynamics (CFD) principles. The outcome of CFD simulations is comparable to that measured by 4D flow imaging. Thus, a comparison of imaging and simulation of the cerebral blood flow is possible.

As highlighted in section 4.3, there are several important problems that arise when treating a patient with an acute ischemic stroke. Current treatment options include the application of thrombolytic therapy, the mechanical thrombectomy, as well as a combination thereof. However, both treatments are associated with complication risks for the patient. Therefore, performing no treatment is also an option, especially if the possible drawbacks outperform the expected benefits. The prediction of tissue outcome has

been a central subject in acute stroke research for several years. For this purpose, the perfusion-diffusion mismatch is typically used as a surrogate for the ischemic penumbra, which is assumed to represent the tissue likely to develop an infarction if normal blood flow is not recovered within sufficient time. However, this concept has several drawbacks, whereas one, the dependency to the hemodynamic analysis method, has been illustrated in section 4.3.1. The prediction of tissue outcome remains a challenging task. Within this context, the multiparametric prediction of tissue outcome seems a promising alternative to the usage of the simple perfusion-diffusion mismatch concept. Lu et al. [Lu et al., 2005], for example, proposed a multiparametric tissue outcome prediction model that includes information from diffusion-weighted, multi-echo T2-weighted and T1 weighted MR imaging. Similar to this, Wu et al. [Wu et al., 2001] proposed a prediction model that combines information from T2-weighted, DWI and PWI MR datasets. For this purpose, the PWI datasets were used to calculate relative perfusion parameter maps of the cerebral blood flow, cerebral blood volume and mean transit time. Using a generalized linear model, Wu et al. were able to show that this model enables a better prediction of tissue outcome compared to using only PWI or DWI datasets for this purpose. Therefore, another topic of continuing research projects is the multiparametric prediction of tissue outcome. Within this context, it is planned to set up a database of multiparametric MR datasets of acute stroke patients, who were treated with different therapies. After collection of a sufficient number of datasets, high-level classification algorithms, such as support vector machines or multilayer perceptron approaches, will be used for a voxel-wise training of tissue outcome for each treatment option. Thus, a voxel-wise prediction of tissue outcome using the trained models may be possible such that a prediction of the global tissue outcome could be obtained for each possible therapy.
Even more important than the tissue outcome itself is the associated functional outcome. Depending on the infarct location, a large stroke may be less severe than a small infarct lesion regarding the functional outcome for the patient. Therefore, it is also important to estimate the contribution of certain brain areas to functional scores like the NIHSS (National Institute for Health Stroke Score) or the mRS (modified rankin scale). This can, for example, be achieved using lesion symptom mapping in terms of a multiperturbation analysis (MPA), which is based on the Shapley value theory and relies on the axiomatic foundations from game theory [Keinan et al., 2004].
By combination of all aforementioned methods, a personalized therapy decision support for patients with an acute ischemic stroke may become possible in near future.

The main focus of the above given outlook is to support clinical research and improve the clinical diagnosis and therapy decision-making. Apart from this, it is also planned to perform further experiments regarding the methodical aspects of this work. Within this context, it is especially important to highlight that the segmentation framework for the automatic delineation of cerebrovascular structures has only been evaluated extensively using manual segmentations as gold standard. However, the interactive segmentation is very time-consuming, which can be ascribed to the difficult delineation of small ves-

sels that have to be tracked over several slices in the orthogonal views. The fact that small vessels are affected by partial volume effects to a large extent makes the correct interactive segmentation even more difficult. This is also one possible explanation for the moderate to good inter-observer agreement that has been quantified with a Dice coefficient between 0.732 and 0.837 (see section 3.1.3). It has been shown that the proposed segmentation framework is capable of extracting cerebrovascular structures within the range of the inter-observer agreement. It would be interesting to evaluate if this segmentation technique is even capable of delineating more vascular structures and at a higher precision than human observers. Therefore, it may be valuable to employ phantom datasets for a more detailed analysis of this segmentation method. Within this context, VascuSynth, a framework that allows generating synthetic software phantoms of the vasculature, has been recently proposed [Hamarneh and Jassi, 2010]. VascuSynth allows simulating volumetric images of vascular trees taking account of noise and non-homogeneity effects. Concurrently, a corresponding ground truth segmentation is generated that can be used for evaluation of segmentation algorithms. VascuSynth does not allow simulating complex vascular pathologies like arteriovenous malformations, which are especially difficult to segment. Therefore, it may be valuable to use physical flow phantoms for an evaluation of the presented segmentation procedure. Several flow phantoms with aneurysm models are already commercially available and have, for example, been used for comparison of MRI and CFD simulations [Marquering et al., 2011]. These phantoms could also be used to compare the segmentation results to a known ground truth, e.g. the phantom capacity volume or diameter at certain locations. A basic validation of the proposed segmentation scheme based on known diameters has already been performed in this work using contrast media filled tubes with five different diameters (see section 4.2.1). In summary, this evaluation revealed that the segmentation procedure leads to errors between 0.02 and 0.5 mm regarding the extracted vessel diameters, which is within voxel accuracy. Thus, it would be interesting to validate this finding on a broader basis using real flow phantoms. Although aneurysm phantoms are frequently used for research purposes, there is no arteriovenous malformation phantom available yet. One of the main reasons for this is that the complex angioarchitecture of arteriovenous malformation is still not well understood. Within this context, it may be possible to use a real resected nidus of an arteriovenous malformation for imaging at very high resolution, such that a precise segmentation becomes possible. This segmentation could then be used for construction of a physical flow phantom, e.g. by rapid prototyping. Apart from the evaluation of the segmentation procedure, physical flow phantoms could also be used for further validations of the bolus arrival time determination method described in section 3.2.1 and the following 4D visualization (see section 3.3.1) as MR-capable pumps with adjustable pump velocities could be attached to the phantoms.

In conclusion, the proposed framework for the cerebrovascular segmentation and the presented reference-based linear curve fitting model for hemodynamic analysis lay the foundation for numerous continuing research projects that will hopefully lead to an improved understanding and clinical management of cerebrovascular diseases.

Chapter 6

Summary

The cerebral stroke is a major cause for death and disability in the western hemisphere. It is estimated that one out of twenty adults will suffer from a cerebral stroke during lifetime and it is expected that the aging population will further increase the incidence of cerebral strokes. Thus, the optimal care of patients with a cerebrovascular disease will become even more important than it is already the case today.

Approximately 72% of all stroke incidences can be ascribed to ischemic strokes that are caused by an occlusion of an artery, which leads to a reduced or complete restriction of cerebral perfusion in the supplied brain tissue. In contrast to this, roughly 20% of all cerebral strokes are caused by an acute bleeding due to a rupture of a vessel. In the majority of cases, these ruptures originate from cerebrovascular pathologies such as aneurysms or arteriovenous malformations, which cause a weakening of the affected vessel walls. Both, a present acute ischemic stroke as well as a diagnosed cerebrovascular malformation, require a detailed knowledge about the vascular anatomy for an optimal diagnosis, therapy decision, and intervention. Furthermore, an in-depth understanding of the blood flow at a macrovascular level and/or microvascular perfusion level may add further benefits for the clinical practice for several questions.

A detailed knowledge regarding these points can be obtained using magnetic resonance imaging (MRI). However, a typical dataset that consists of high resolution 3D as well as time-resolved (4D) image sequences is associated with a massive amount of data that has to be analyzed by the physicians. Such an examination may not only be very time-consuming but also error-prone. Thus, advanced computer-assisted image analysis methods may not only lead to improved diagnoses but also to a reduction of the time that is required for this.

From a methodical perspective there are three main problems that have to be dealt with and which have been in focus of this work: the automatic segmentation of cerebrovascular structures, the hemodynamic analysis of time-resolved MR datasets, and the combined analysis and visualization of vascular structures together with the corresponding hemodynamic situation.

Numerous methods for the automatic cerebrovascular segmentation from high-resolution image sequences have been proposed in the past. However, typical segmentation ap-

proaches usually result in a trade-off regarding a sufficient delineation of small and malformed vessels. The multi-step segmentation framework proposed in this work was developed to overcome this limitation. Therefore, the brain tissue is segmented from the high resolution 3D magnetic resonance angiography (MRA) dataset in a first step using a graph-based approach. The main motivation of this step was to prevent leakage of the segmentation to non-brain tissue in the subsequent processing steps. After this, a non-linear combination of intensity and shape information using fuzzy logic is performed in the second step. Here, the required shape information is obtained from the vesselness filter, which enhances tubular structures. The result of this combination is a new parameter image in which small as well as malformed vessels are enhanced. The cerebrovascular system is then extracted from this parameter image in the third step using a level-set segmentation approach. The smoothing associated with the internal energy weight of level-set approaches usually leads to the problem that the level-set evolution into small thin vessels is hindered. This problem was solved in this work by developing a level-set model, which has been extended in a way that it uses information about the local 3D course of a vessel to adjust the weight of the internal energy. Even with this adaption, gaps may occur in the resulting segmentation. These gaps are reduced in the last step of the proposed segmentation framework. For this purpose, vessel endpoints are identified in the cerebrovascular segmentation, which are then connected to already segmented vessels using a shortest-path algorithm. An evaluation of this segmentation framework using manual segmentations as ground truth demonstrated that this approach is capable of segmenting small as well as malformed vessel with high precision. Furthermore, the results of this evaluation showed that this segmentation framework leads to significantly better segmentation results than four other tested state-of-art methods. Moreover, the segmentation results are within the range of inter-observer differences.

The automatic segmentation of the cerebrovascular system can, for example, be used for a surface-based visualization, which enables an intuitive screening of the anatomy. However, no information about the blood flow is available at this point. Therefore, time-resolved magnetic resonance angiographies were analyzed in addition to the high resolution 3D MRA datasets. Several parameters have been proposed in the past that can be calculated based on concentration time curves derived from 4D MR angiographies. One parameter of general interest for the analysis of the blood flow at macrovascular level as well as for microvascular perfusion is the time-to-peak (TTP) parameter. Since typical concentration time curves are affected by noise, bolus recirculation and are only represented by discrete sample points, the direct estimation of this parameter is rather imprecise. Therefore, several parametric models have been presented, which are fitted to the concentration time curves prior to TTP estimation. However, these models make strong assumptions about typical shapes of indicator dilution curves, which may be violated in case of cerebrovascular diseases. This drawback can be overcome using the developed reference-based linear curve fitting model. Here, the main idea is to extract a patient-individual hemodynamic reference curve directly from the given time-resolved dataset, which is then used for curve fitting and subsequent parameter estimation. A

comparison to state-of-the-art methods using Monte-Carlo simulations as well as clinical datasets revealed that this technique leads to reduced errors regarding the time-to-peak estimation over a wide range of temporal resolutions.

The hemodynamic analysis enables a quantitative evaluation of time-resolved angiographic datasets. However, a direct combined analysis and visualization of the cerebrovascular system together with the corresponding blood flow situation is still not possible at this stage. Therefore, a novel 4D blood flow visualization technique was developed within the scope of this work, which overcomes this limitation. The main idea of this approach is to register 3D and 4D MRA image sequences of a patient such that the time-to-peak parameter can be displayed dynamically over time on the surface model of the cerebrovascular system. An evaluation of this method using datasets of patients with arteriovenous malformations revealed that the 4D blood flow visualization leads to a reliable combined representation of the angioarchitecture and blood flow situation, which allows an intuitive and fast diagnosis.

The developed methods have already been successfully employed for several research studies regarding arteriovenous malformations, aneurysms, and ischemic strokes in addition to the developed 4D blood flow visualization. A selection of the conducted research studies employing the automatic cerebrovascular segmentation and hemodynamic analysis was described in the second part of this work.

Using the developed methods, it was discovered that a previous hemorrhage is the only risk factor for a rupture of an arteriovenous malformation that is associated to significant and persistent blood flow alterations. It was also shown that arteriovenous malformations lead to a territorial as well as a microvascular perfusion disturbance in the adjacent brain tissue. Furthermore, a novel computer-aided segmentation and angiographic characterization of this vascular pathology was developed by integrating the results of the cerebrovascular segmentation framework and hemodynamic analysis. The resulting angiographic characterization was judged to be essentially helpful for therapy planning of this malformation.

The neck and dome diameters of an aneurysm are important variables for endavascular coil therapy. Employing the multi-step segmentation framework, it was possible to develop a 3D measurement method for quantifying these diameters, whereas the results showed that this 3D measurement method leads to highly reliable and reproducible diameter estimates. Furthermore, it was shown that the cerebrovascular segmentation can also be used for quantifying aneurysm recurrence volumes after endovascular coil treatment. Such a quantitative definition of recurrence volumes allows a more timely and economical evaluation of new coil materials since the required patient sample size can be considerably reduced without loosing statistical power as compared to the usage of binary endpoints.

6 Summary

The quantification of the perfusion-diffusion mismatch is an important parameter to identify patients with an acute ischemic stroke who are likely to benefit from a thrombolytic therapy. However, it was discovered that the application of different hemodynamic models for the perfusion analysis lead to high variations regarding this volumetric mismatch, which has to be taken into account for clinical decision making when analyzing perfusion-weighted MRI datasets. Due to treatment guidelines, acute ischemic stroke patients with unknown time from symptom onset are currently precluded from thrombolytic therapy. Within a large multi-center study it was shown that it is possible to identify acute stroke patients within a time window of 4.5 hours since stroke onset with a sensitivity of 62% and specificity of 83% using the described DWI-FLAIR mismatch concept. It was further demonstrated that the DWI-FLAIR mismatch is not influenced by the microvascular perfusion situation and that the associated elevated T2-values cannot be used for predicting the final tissue outcome.

In conclusion, the proposed framework for the segmentation of cerebrovascular structures and the presented reference-based linear curve fitting model for hemodynamic analysis have already proven useful for clinical applications and lay the foundation for numerous continuing research projects, which may ultimately lead to an improved understanding and clinical management of cerebrovascular diseases.

Bibliography

[Albers et al., 2006] Albers, G., Thijs, V., Wechsler, L., Kemp, S., Schlaug, G., Skalabrin, E., Bammer, R., Kakuda, W., Lansberg, M., Shuaib, A., Coplin, W., Hamilton, S., Moseley, M., and Marks, M. (2006). **Magnetic resonance imaging profiles predict clinical response to early reperfusion: The diffusion and perfusion imaging evaluation for understanding stroke evolution (DEFUSE) study**. *Annals of Neurology*, 60(5):508–517.

[Anbarasu and Gould, 2002] Anbarasu, A. and Gould, D. (2002). **Diagnosis of an intracranial arteriovenous malformation using extracranial carotid doppler sonography**. *Journal of Clinical Ultrasound*, 30(4):249–252.

[Barrett and Mortensen, 1997] Barrett, W. and Mortensen, E. (1997). **Interactive live-wire boundary extraction**. *Medical Image Analysis*, 1(4):331–341.

[Beck et al., 2006] Beck, J., Raabe, A., Szelenyi, A., Berkefeld, J., Gerlach, R., Setzer, M., and Seifert, V. (2006). **Sentinel headache and the risk of rebleeding after aneurysmal subarachnoid hemorrhage**. *Stroke*, 37(11):2733–2737.

[Bi et al., 2010] Bi, X., Weale, P., Schmitt, P., Zuehlsdorff, S., and Jerecic, R. (2010). **Non-contrast-enhanced four-dimensional (4D) intracranial MR angiography: A feasibility study.** *Magnetic Resonance in Medicine*, 63(3):835–841.

[Bland and Altman, 1986] Bland, J. and Altman, D. (1986). **Statistical methods for assessing agreement between two methods of clinical measurement**. *Lancet*, 8(1):307–310.

[Bogaard et al., 1986] Bogaard, J., Jansen, J., von Reth, E., Versprille, A., and Wise, M. (1986). **Random walk type models for indicator-dilution studies: Comparison of a local density random walk and a first passage times distribution**. *Cardiovascular Research*, 20(1):789–96.

[Bonita, 1992] Bonita, R. (1992). **Epidemiology of stroke**. *Lancet*, 339:342–344.

[Brant-Zawadzki et al., 1996] Brant-Zawadzki, M., Atkinson, D., Detrick, M., Bradley, W., and Scidmore, G. (1996). **Fluid-attenuated inversion recovery (FLAIR) for assessment of cerebral infarction. Initial clinical experience in 50 patients**. *Stroke*, 27(7):1187–1191.

[Brekenfeld et al., 2008] Brekenfeld, C., Schroth, G., El-Koussy, M., Nedeltchev, K., Reinert, M., Slotboom, J., and Gralla, J. (2008). **Mechanical thromboembolectomy for acute ischemic stroke: Comparison of the catch thrombectomy device and the Merci Retriever in vivo**. *Stroke*, 39(4):1213–1219.

[Cebral et al., 2011] Cebral, J., Mut, F., Weir, J., and Putman, C. (2011). **Association of hemodynamic characteristics and cerebral aneurysm rupture**. *American Journal of Neuroradiology*, 32(2):264–270.

[Chapman et al., 2004] Chapman, B., Stapelton, J., and Parker, D. (2004). **Intracranial vessel segmentation from Time-of-Flight MRA using pre-processing of the MIP Z-buffer: Accuracy of the ZBS algorithm**. *Medical Image Analysis*, 8(2):113–126.

[Cheng et al., 2012] Cheng, B., Rosenkranz, M., Krützelmann, A., Fiehler, J., Forkert, N., Gerloff, C., and Thomalla, G. (2012). **The extent of perfusion deficit does not relate to the visibility of acute ischemic lesions on fluid-attenuated inversion recovery imaging**. *Journal of Neuroimaging*, 23(2):215–218.

[Cheng et al., 2013] Cheng, B., Brinkmann, M., Forkert, N., Treszl, A., Ebinger, M., Köhrmann, M., Wu, O., Kang, D.-W., Liebeskind, D., Tourdias, T., Singer, O., Christensen, S., Luby, M., Warach, S., Fiehler, J., Fiebach, J., Gerloff, C., and Thomalla, G. (2013). **Quantitative measurements of relative fluid-attenuated inversion recovery (FLAIR) signal intensities in acute stroke for the prediction of time from symptom onset**. *Journal of Cerebral Blood Flow and Metabolism*, 33(1):76–84.

[Choi and Mohr, 2005] Choi, J. and Mohr, J. (2005). **Brain arteriovenous malformations in adults**. *Lancet Neurology*, 4(5):299–308.

[Costantino and Vinters, 1986] Costantino, A. and Vinters, H. (1986). **A pathologic correlate of the 'Steal' phenomenon in a patient with cerebral arteriovenous malformation**. *Stroke*, 17(1):103–106.

[Danielsson, 1980] Danielsson, P.-E. (1980). **Euclidean distance mapping**. *Computer Graphics and Image Processing*, 14:227–248.

[Davis and Donnan, 2009] Davis, S. and Donnan, G. (2009). **4.5 hours: The new time window for tissue plasminogen activator in stroke**. *Stroke*, 40(6):2266–2267.

[Davis et al., 1993] Davis, W., Warnock, S., Harnsberger, H., Parker, D., and Chen, C. (1993). **Intracranial MRA: Single volume vs. multiple thin slab 3D Time-of-Flight acquisition**. *Journal of Computer Assisted Tomography*, 17(1):15–21.

[Deriche, 1987] Deriche, R. (1987). **Using canny's criteria to derive a recursively implemented optimal edge detector**. *International Journal of Computer Vision*, 1(2):167–187.

[Dewey et al., 2001] Dewey, H., Thrift, A., Mihalopoulos, C., Carter, R., Macdonell, R., McNeil, J., and Donnan, G. (2001). **Cost of stroke in Australia from a societal perspective: Results from the north east melbourne stroke incidence study (NEMESIS)**. *Stroke*, 32(10):2409–2416.

[Dietrich et al., 2010] Dietrich, O., Biffar, A., Baur-Melnyk, A., and Reiser, M. (2010). **Technical aspects of MR diffusion imaging of the body**. *European Journal of Radiology*, 76(3):314–322.

[Dijkstra, 1959] Dijkstra, E. (1959). **A note on two problems in connexion with graphs**. *Numerische Mathematik*, 1:269–271.

[Donnan et al., 2008] Donnan, G., Fisher, M., Macleod, M., and Davis, S. (2008). **Stroke**. *Lancet*, 371:1612–1623.

[Feigin et al., 2009] Feigin, V., Lawes, C., Barker-Collo, D. B. S., and Parag, V. (2009). **Worldwide stroke incidence and early case fatality reported in 56 population-based studies: A systematic review**. *Lancet Neurology*, 8(4):355–69.

[Fennema-Notestine et al., 2006] Fennema-Notestine, C., Ozyurt, B., Clark, C., Morris, S., Bischoff-Grethe, A., Bondi, M., Jernigan, T., Fischl, B., Segonne, F., Shattuck, D., Leahy, R., Rex, D., Toga, A., Zou, K., Morphometry BIRN, and Brown, G. (2006). **Quantitative evaluation of automated skull-stripping methods applied to contemporary and legacy images: Effects of diagnosis, bias correction, and slice location**. *Human Brain Mapping*, 27(2):99–113.

[Fiehler, 2012] Fiehler, J. (2012). **Unruptured brain aneurysms: When to screen and when to treat?** *Fortschritte auf dem Gebiet der Röntgenstrahlen und der bildgebenden Verfahren*, 184(2):97–104.

[Fiehler et al., 2009] Fiehler, J., Illies, T., Piening, M., Säring, D., Forkert, N., Regelsberger, J., Grzyska, U., Handels, H., and JV, J. B. (2009). **Territorial and microvascular perfusion impairment in brain arteriovenous malformations**. *American Journal of Neuroradiology*, 30(2):356–361.

[Fink et al., 2005a] Fink, C., Ley, S., Kroeker, R., Requard, M., Kauczor, H., and Bock, M. (2005). **Time-resolved contrast-enhanced three-dimensional magnetic resonance angiography of the chest: Combination of parallel imaging with view sharing**. *Investigative Radiology*, 40(1):40–48.

[Fink et al., 2005b] Fink, C., Puderbach, M., Ley, S., Zaporozhan, J., Plathow, C., and Kauczor, H. (2005). **Time-resolved echo-shared parallel MRA of the lung: Observer preference study of image quality in comparison with non-echo-shared sequences**. *European Radiology*, 15:2070–2074.

[Fleetwood and Steinberg, 2002] Fleetwood, I. and Steinberg, G. (2002). **Arteriovenous malformations**. *Lancet*, 359(9309):863–873.

[Forkert et al., 2009] Forkert, N., Säring, D., Fiehler, J., Illies, T., Möller, D., and Handels, H. (2009). **Automatic brain segmentation in Time-of-Flight MRA images**. *Methods of Information in Medicine*, 48(5):399–407.

[Forkert et al., 2011a] Forkert, N., Fiehler, J., Ries, T., Illies, T., Möller, D., Handels, H., and Säring, D. (2011). **Reference-based linear curve fitting for bolus arrival time estimation in 4D MRA and MR perfusion-weighted image sequences**. *Magnetic Resonance in Medicine*, 65(1):289–294.

[Forkert et al., 2011b] Forkert, N., Schmidt-Richberg, A., Fiehler, J., Illies, T., Möller, D., Handels, H., and Säring, D. (2011). **Fuzzy-based vascular structure enhancement in Time-of-Flight MRA images for improved segmentation**. *Methods of Information in Medicine*, 50(1):74–83.

[Forkert et al., 2012a] Forkert, N., Fiehler, J., Illies, T., Möller, D., Handels, H., and Säring, D. (2012). **4D blood flow visualization fusing 3D and 4D MRA image sequences**. *Journal of Magnetic Resonance Imaging*, 36(2):443–553.

[Forkert et al., 2012b] Forkert, N., Illies, T., Möller, D., Handels, H., Säring, D., and Fiehler, J. (2012). **Analysis of the influence of 4D MR angiography temporal resolution on Time-to-Peak estimation error for different cerebral vessel structures**. *American Journal of Neuroradiology*, 33(11):2103–2109.

[Forkert et al., 2012c] Forkert, N., Schmidt-Richberg, A., Fiehler, J., Illies, T., Möller, D., Handels, H., and Säring, D. (2012). **Automatic correction of gaps in cerebrovascular segmentations extracted from 3D Time-of-Flight MRA datasets**. *Methods of Information in Medicine*, 51(5):415–422.

[Forkert et al., 2012d] Forkert, N., Schmidt-Richberg, A., Fiehler, J., Illies, T., Möller, D., Säring, D., Handels, H., and Ehrhardt, J. (2012). **3D cerebrovascular segmentation combining fuzzy vessel enhancement and level-sets with anisotropic energy weights**. *Magnetic Resonance Imaging*, 31(2):262–271.

[Forkert et al., 2013a] Forkert, N., Fiehler, J., Schönfeld, M., Sedlacik, J., Regelsberger, J., Handels, H., and Illies, T. (2013). **Intranidal signal distribution in post-contrast Time-of-Flight MRA is associated with rupture risk factors in arteriovenous malformations**. *Clinical Neuroradiology*, 23(2):97–101.

[Forkert et al., 2013b] Forkert, N., Illies, T., Goebell, E., Säring, D., Fiehler, J., and Handels, H. (2013). **Computer-aided nidus segmentation and angiographic characterization of arteriovenous malformations**. *International Journal of Computer Assisted Radiology and Surgery*. [Epub ahead of print].

[Forkert et al., 2013c] Forkert, N., Kaesemann, P., Treszl, A., Siemonsen, S., Cheng, B., Handels, H., Fiehler, J., and Thomalla, G. (2013). **Comparison of ten TTP and Tmax estimation techniques for MR perfusion-diffusion mismatch quantification**. *American Journal of Neuroradiology*. [Epub ahead of print].

[Forsting and Wanke, 2008] Forsting, M. and Wanke, I. (2008). **Intracranial vascular malformations and aneurysms: From diagnostic work-up to endovascular therapy**. Springer Verlag.

[González et al., 2011] González, R., Hirsch, J., Lev, M., Schaefer, P., and Schwamm, L. (2011). **Acute ischemic stroke: Imaging and intervention**. Springer.

[Groth et al., 2013] Groth, M., Forkert, N., Buhk, J.-H., Schönfeld, M., Goebell, E., and Fiehler, J. (2013). **Comparison of 3D computer-aided with manual cerebral aneurysm measurements in different imaging modalities**. *Neuroradiology*, 55(2):171–178.

[Guo et al., 2004] Guo, W., Wub, Y., Wua, H., Chungc, W., Kaof, Y., Yeha, T., Shiaud, C., Panc, D., Changh, Y., and Hsieh, J. (2004). **Toward normal perfusion after radiosurgery: Perfusion MR imaging with independent component analysis of brain arteriovenous malformations**. *American Journal of Neuroradiology*, 25:1636–1644.

[Hahn, 1950] Hahn, E. (1950). **Spin echoes**. *Physical Review*, 80(4):580–594.

[Hamarneh and Jassi, 2010] Hamarneh, G. and Jassi, P. (2010). **VascuSynth: Simulating vascular trees for generating volumetric image data with ground-truth segmentation and tree analysis**. *Computerized Medical Imaging and Graphics*, 34(8):605–616.

[Handels, 2009] Handels, H. (2009). **Medizinische Bildverarbeitung**. Vieweg Teubner.

[Hassouna et al., 2006] Hassouna, M., Farag, A., Hushek, S., and Moriarty, T. (2006). **Cerebrovascular segmentation from TOF using stochastic models**. *Medical Image Analysis*, 10(1):2–18.

[Helle et al., 2010] Helle, M., Norris, D., Rüfer, S., Alfke, K., Jansen, O., and van Osch, M. (2010). **Superselective pseudocontinuous arterial spin labeling**. *Magnetic Resonance in Medicine*, 64(3):777–786.

[Hope et al., 2009] Hope, M., Purcell, D., Hope, T., von Morze, C., Vigneron, D., Alley, M., and Dillon, W. (2009). **Complete intracranial arterial and venous blood flow evaluation with 4D flow MR imaging**. *American Journal of Neuroradiology*, 30(2):362–326.

[Hope et al., 2010] Hope, T., Hope, M., Purcell, D., von Morze, C., Vigneron, D., Alley, M., and Dillon, W. (2010). **Evaluation of intracranial stenoses and aneurysms with accelerated 4D flow**. *Magnetic Resonance Imaging*, 28(1):41–46.

[Illies et al., 2012] Illies, T., Forkert, N., Säring, D., Wenzel, K., Ries, T., Regelsberger, J., Wegscheider, K., and Fiehler, J. (2012). **Persistent hemodynamic changes in ruptured brain arteriovenous malformations**. *Stroke*, 43(11):2910–2915.

[Illies et al., 2013] Illies, T., Forkert, N., Ries, T., Regelsberger, J., and Fiehler, J. (2013). **Classification of cerebral arteriovenous malformations and intranidal flow patterns by color-encoded 4D-Hybrid-MRA**. *American Journal of Neuroradiology*, 34(1):46–53.

[Jiang et al., 2011] Jiang, J., Johnson, K., Valen-Sendstad, K., Mardal, K., Wieben, O., and Strother, C. (2011). **Flow characteristics in a canine aneurysm model: A comparison of 4D accelerated phase-contrast MR measurements and computational fluid dynamics simulations**. *Medical Physics*, 38(11):6300–6312.

[Joachims, 1999] Joachims, T. (1999). **Chapter: Making large-scale support vector machine learning practical**, *Advances in kernel methods*. MIT Press, Cambridge, MA, USA.

[Kakalis et al., 2008] Kakalis, N., Mitsos, A., Byrne, J., and Ventikos, Y. (2008). **The haemodynamics of endovascular aneurysm treatment: A computational modelling approach for estimating the influence of multiple coil deployment**. *IEEE Transactions on Medical Imaging*, 27(6):814–824.

[Kallmes and Fujiwara, 2002] Kallmes, D. and Fujiwara, N. (2002). **New expandable hydrogel-platinum coil hybrid device for aneurysm embolization**. *American Journal of Neuroradiology*, 23(9):1580–1588.

[Keinan et al., 2004] Keinan, A., Sandbank, B., Hilgetag, C., Meilijson, I., and Ruppin, E. (2004). **Fair attribution of functional contribution in artificial and biological networks**. *Neural Computation*, 16(9):1887–1915.

[Kholmovski et al., 2002] Kholmovski, E., Alexander, A., and Parker, D. (2002). **Correction of slab boundary artifact using histogramm matching**. *Journal of Magnetic Resonance Imaging*, 15:610–617.

[Kirbas and Quek, 2002] Kirbas, C. and Quek, F. (2002). **A review of vessel extraction techniques and algorithms**. *ACM Computing Surveys*, 36(6):81–121.

[Kondziolka et al., 1995] Kondziolka, D., McLaughlin, M., and Kestle, J. (1995). **Simple risk predictions for arteriovenous malformations of the brain**. *Neurosurgery*, 37(5):648–655.

[Lantz and Meyers, 2008] Lantz, E. and Meyers, P. (2008). **Neuropsychological effects of brain arteriovenous malformations**. *Neuropsychology Review*, 18:167–177.

[Lee and Kashyap, 1994] Lee, T.-C. and Kashyap, R. (1994). **Building skeleton models via 3-D medial surface/axis thinning algorithms**. *Graphical Models And Image Processing*, 56(6):462–478.

[Lesage et al., 2009] Lesage, D., Angelini, E., Bloch, I., and Funka-Lea, G. (2009). **A review of 3D vessel lumen segmentation techniques: Models, features and extraction schemes**. *Medical Image Analysis*, 13(6):819–845.

[Liney et al., 1996] Liney, G., Knowles, A., Manton, D., Turnbull, L., Blackband, S., and Horsman, A. (1996). **Comparison of conventional single echo and multi-echo sequences with a fast spin-echo sequence for quantitative T2 mapping: Application to the prostate**. *Journal of Magnetic Resonance Imaging*, 6(4):603–607.

[Linton et al., 1995] Linton, R., Linton, N., and Band, D. (1995). **A new method of analysing indicator dilution curves**. *Cardiovascular Research*, 30(6):930–938.

[Lorigo et al., 2001] Lorigo, L., Faugeras, O., Grimson, W., Keriven, R., Kikinis, R., Nabavi, A., and Westin, C. (2001). **Curves: Curve evolution for vessel segmentation**. *Medical Image Analysis*, 5(3):195–206.

[Lu et al., 2005] Lu, M., Mitsias, P., Ewing, J., Soltanian-Zadeh, H., Bagher-Ebadian, H., Zhao, Q., Oja-Tebbe, N., Patel, S., and Chopp, M. (2005). **Predicting final infarct size using acute and subacute multiparametric MRI measurements in patients with ischemic stroke**. *Journal of Magnetic Resonance Imaging*, 21(5):495–502.

[Löwenhardt, 2001] Löwenhardt, B. (2001). **Bildgebende Diagnostik**. Wissenschaftlicher Selbstverlag.

[Mamdani and Assilian, 1975] Mamdani, E. and Assilian, S. (1975). **An experiment in linguistic synthesis with a fuzzy logic controller**. *International Journal of Man-Machine Studies*, 7(1):135–147.

[Markl et al., 2007] Markl, M., Harloff, A., Bley, T., Zaitsev, M., Jung, B., Weigang, E., Langer, M., Hennig, J., and Frydrychowicz, A. (2007). **Time-resolved 3D MR velocity mapping at 3T: Improved navigator-gated assessment of vascular anatomy and blood flow**. *Journal of Magnetic Resonance Imaging*, 25(4):824–831.

[Marquering et al., 2011] Marquering, H., van Ooij, P., Streekstra, G., Schneiders, J., Majoie, C., van Bavel, E., and Nederveen, A. (2011). **Multiscale flow patterns within an intracranial aneurysm phantom**. *IEEE Transactions on Biomedical Engineering*, 58(12):3447–3450.

[Mast et al., 1997] Mast, H., Young, W., Koennecke, H., Sciacca, R., Osipov, A., Pile-Spellman, J., Hacein-Bey, L., Duong, H., Stein, B., and Mohr, J. (1997). **Risk of spontaneous haemorrhage after diagnosis of cerebral arteriovenous malformation**. *Lancet*, 350(9084):1065–1068.

[Molyneux et al., 2005] Molyneux, A., Kerr, R., Yu, L., Clarke, M., Sneade, M., Yarnold, J., and Sandercock, P. (2005). **International subarachnoid aneurysm**

trial (ISAT) of neurosurgical clipping versus endovascular coiling in 2143 patients with ruptured intracranial aneurysms: A randomised comparison of effects on survival, dependency, seizures, rebleeding, subgroups, and aneurysm occlusion. *Lancet*, 366(9488):809–817.

[Ogilvy et al., 2001] Ogilvy, C., Stieg, P., Awad, I., Brown, R., Kondziolka, D., Rosenwasser, R., Young, W., and Hademenos, C. (2001). **AHA scientific statement: Recommendations for the management of intracranial arteriovenous malformations: A statement for healthcare professionals from a special writing group of the Stroke Council, American Stroke Association**. *Stroke*, 32(6):1458–1471.

[Orlowski et al., 2008] Orlowski, P., Noble, J., Ventikos, Y., Byrne, J., and Summers, P. (2008). **Image-based simulation of brain arteriovenous malformation hemodynamics**. *5th IEEE International Symposium on Biomedical Imaging: From Nano to Macro*, pages 676–679.

[Ries et al., 2007] Ries, T., Siemonsen, S., Thomalla, G., Grzyska, U., Zeumer, H., and Fiehler, J. (2007). **Long-term follow-up of cerebral aneurysms after endovascular therapy prediction and outcome of retreatment**. *American Journal of Neuroradiology*, 28(9):1755–1761.

[Ries et al., 2011] Ries, T., Wegscheider, K., Wulff, A., Radelfahr, K., Säring, D., Forkert, N., and Fiehler, J. (2011). **Quantification of recurrence volumes after endovascular treatment of cerebral aneurysm as surrogate endpoint for treatment stability**. *Neuroradiology*, 53(8):593–598.

[Rinkel et al., 1998] Rinkel, G., Djibuti, M., Algra, A., and van Gijn, J. (1998). **Prevalence and risk of rupture of intracranial aneurysms: A systematic review**. *Stroke*, 29(1):251–256.

[Sacco et al., 1997] Sacco, R., Benjamin, E., Broderick, J., Dyken, M., Easton, J., Feinberg, W., Goldstein, L., Gorelick, P., Howard, G., Kittner, S., Manolio, T., Whisnant, J., and Wolf, P. (1997). **American Heart Association Prevention Conference. IV. prevention and rehabilitation of stroke. risk factors**. *Stroke*, 28(7):1507–17.

[Sato et al., 1998] Sato, Y., Nakajima, S., Shiraga, N., Atsumi, H., Yoshida, S., Koller, T., Gerig, G., and Kikinis, R. (1998). **Three-dimensional multi-scale line filter for segmentation and visualization of curvelinear structures in medical images**. *Medical Image Analysis*, 2(2):143–168.

[Saver, 2006] Saver, J. (2006). **Time is brain - quantified**. *Stroke*, 37(1):263–236.

[Schmidt-Richberg et al., 2009] Schmidt-Richberg, A., Handels, H., and Ehrhardt, J. (2009). **Integrated segmentation and non-linear registration for organ segmentation and motion field estimation in 4D CT data**. *Methods of Information in Medicine*, 48(4):344–349.

[Serena et al., 2003] Serena, J., Dávalos, A., Segura, T., Mostacero, E., and Castillo, J. (2003). **Stroke on awakening: Looking for a more rational management**. *Cerebrovascular Disease*, 16(2):128–133.

[Shi et al., 2010] Shi, Z., Loh, Y., Walker, G., and Duckwiler, G. (2010). **Endovascular thrombectomy for acute ischemic stroke in failed intravenous tissue plasminogen activator versus non-intravenous tissue plasminogen activator patients: Revascularization and outcomes stratified by the site of arterial occlusions**. *Stroke*, 41(6):1185–1192.

[Siemonsen et al., 2009] Siemonsen, S., Mouridsen, K., Holst, B., Ries, T., Finsterbusch, J., Thomalla, G., Ostergaard, L., and Fiehler, J. (2009). **Quantitative T2 values predict time from symptom onset in acute stroke patients**. *Stroke*, 40(5):1612–1616.

[Siemonsen et al., 2012] Siemonsen, S., Löbel, U., Sedlacik, J., Forkert, N., Mouridsen, K., Østergaard, L., Thomalla, G., and Fiehler, J. (2012). **Elevated T2-values in MRI of stroke patients shortly after symptom onset do not predict irreversible tissue infarction**. *Brain*, 135(6):1981–1989.

[Sourbron, 2010] Sourbron, S. (2010). **Technical aspects of MR perfusion**. *European Journal of Radiology*, 76(3):304–313.

[Spetzler and Martin, 1986] Spetzler, R. and Martin, N. (1986). **A proposed grading system for arteriovenous malformations**. *Journal of Neurosurgery*, 65(4):476–483.

[Säring et al., 2010] Säring, D., Forkert, N., Illies, T., Fiehler, J., and Handels, H. (2010). **Evaluation of methods for bolus arrival time determination using a four-dimensional MRA flow phantom**. *Studies in Health Technology and Informatics*, 160(2):1263–1267.

[Säring et al., 2012] Säring, D., Fiehler, J., Ries, T., and Forkert, N. (2012). **Rigid 3D-3D registration of TOF MRA integrating vessel segmentation for quantification of recurrence volumes after coiling cerebral aneurysm**. *Neuroradiology*, 54(2):171–176.

[Stapf et al., 2003] Stapf, C., Mast, H., Sciacca, R., Berenstein, A., Nelson, P., Gobin, Y., Pile-Spellman, J., and Mohr, J. (2003). **The New York Islands AVM study: Design, study progress, and initial results**. *Stroke*, 34(5):e29–33.

[Stapf et al., 2006] Stapf, C., Mast, H., Sciacca, R., Choi, J., Khaw, A., Connolly, E., Pile-Spellman, J., and Mohr, J. (2006). **Predictors of hemorrhage in patients with untreated brain arteriovenous malformation**. *Neurology*, 66(9):1350–1355.

[Stejskal and Tanner, 1965] Stejskal, E. and Tanner, J. (1965). **Spin diffusion measurements: Spin echoes in the presence of a time-dependent field gradient**. *Journal of Chemical Physics*, 42(1):288–292.

[Suri et al., 2002a] Suri, J., Liu, K., Reden, L., and Laxminarayan, S. (2002). **A review on MR vascular image processing algorithms: Acquisition and prefiltering: part I**. *IEEE Transactions on Information Technology in Biomedicine*, 6(4):324–337.

[Suri et al., 2002b] Suri, J., Liu, K., Reden, L., and Laxminarayan, S. (2002). **A review on MR vascular image processing algorithms: Skeleton versus nonskeleton approaches: part II**. *IEEE Transactions on Information Technology in Biomedicine*, 6(4):338–350.

[Takeuchi et al., 1994] Takeuchi, S., Abe, H., Nishimaki, K., Minakawa, T., Koike, T., Kameyama, S., and Tanaka, R. (1994). **Cerebral haemodynamic changes after endovascular treatment of arteriovenous malformations: Evaluation by single-photon emission ct**. *Acta Neurochirurgica*, 127(3):142–150.

[Thomalla et al., 2009] Thomalla, G., Rossbach, P., Rosenkranz, M., Siemonsen, S., Krützelmann, A., Fiehler, J., and Gerloff, C. (2009). **Negative fluid-attenuated inversion recovery imaging identifies acute ischemic stroke at 3 hours or less**. *Annals of Neurology*, 65(6):724–732.

[Thomalla et al., 2011] Thomalla, G., Cheng, B., Ebinger, M., Hao, Q., Tourdias, T., Wu, O., Kim, J., Breuer, L., Singer, O., Warach, S., Christensen, S., Treszl, A., Forkert, N., Galinovic, I., Rosenkranz, M., Engelhorn, T., Köhrmann, M., Endres, M., Khang, D.-W., Dousset, V., Sorensen, A., Liebeskind, D., Fiebach, J., Fiehler, J., and Gerloff, C. (2011). **DWI-FLAIR mismatch for the identification of patients with acute ischaemic stroke within 4.5 h of symptom onset (PRE-FLAIR): A multicentre observational study)**. *Lancet Neurology*, 10(11):978–986.

[Thompson et al., 1964] Thompson, H., Starmer, C., Whalen, R., and McIntosh, H. (1964). **Indicator transit time considered as a gamma variate**. *Circulation Research*, 14:502–515.

[Thrift et al., 2001] Thrift, A., Dewey, H., Macdonell, R., McNeil, J., and Donnan, G. (2001). **Incidence of the major stroke subtypes - initial findings from the north east Melbourne stroke incidence study (NEMESIS)**. *Stroke*, 32(8):1732–1738.

[Vlaardingerbroek and Boer, 2010] Vlaardingerbroek, M. and Boer, J. A. (2010). **Magnetic resonance imaging: theory and practice**. Springer.

[Vlak et al., 2011] Vlak, M., Algra, A., Brandenburg, R., and Rinkel, G. (2011). **Prevalence of unruptured intracranial aneurysms, with emphasis on sex, age, comorbidity, country, and time period: A systematic review and meta-analysis**. *Lancet Neurology*, 10(7):626–636.

[Wells et al., 1996] Wells, W., Viola, P., Atsumi, H., Nakajima, S., and Kikinis, R. (1996). **Multi-modal volume registration by maximization of mutual information**. *Medical Image Analysis*, 1(1):35–51.

[Wu et al., 2001] Wu, O., Koroshetz, W., Ostergaard, L., Buonanno, F., Copen, W., Gonzalez, R., Rordorf, G., Rosen, B., Schwamm, L., Weisskoff, R., and Sorensen, A. (2001). **Predicting tissue outcome in acute human cerebral ischemia using combined diffusion- and perfusion-weighted MR imaging**. *Stroke*, 32(4):933–942.

[Wu et al., 2007] Wu, W., Fernández-Seara, M., Detre, J., Wehrli, F., and Wang, J. (2007). **A theoretical and experimental investigation of the tagging efficiency of pseudocontinuous arterial spin labeling**. *Magnetic Resonance in Medicine*, 58(5):1020–1027.

[Yang, 2002] Yang, Y. (2002). **Perfusion MR imaging with pulsed arterial spin-labeling: Basic principles and applications in functional brain imaging**. *Concepts in Magnetic Resonance*, 14(5):347–357.

[Yu et al., 2012] Yu, S., Yan, L., Yao, Y., Wang, S., Yang, M., Wang, B., Zhuo, Y., Ai, L., Miao, X., Zhao, J., and Wang, D. (2012). **Noncontrast dynamic MRA in intracranial arteriovenous malformation (AVM): Comparison with Time of Flight (TOF) and digital subtraction angiography (DSA)**. *Magnetic Resonance Imaging*, 30(6):869–877.

Appendix A

Cerebrovascular Segmentation

A.1 Automatic Brain Segmentation in Time-of-Flight MRA Images

Nils D. Forkert, Dennis Säring, Jens Fiehler, Till Illies, Dietmar Möller, Heinz Handels:
Automatic brain segmentation in Time-of-Flight MRA images
Methods of Information in Medicine 48(5), 399-407, 2009.

Erratum to Automatic Brain Segmentation in Time-of-Flight MRA Images

Due to a typesetting error, the table 1 in the paper "Automatic Brain Segmentation in Time-of-Flight MRA Images" is not correct and should have appeared as given herewith:

	Mean Time requirement	Mean Dice coefficient	Mean Haussdorff distance	Mean vessel inclusion rate
Inter-Observer-Comparison	2.5 h (manual Segmentation)	0.991	9.6	98.59 %
Brain Extraction Tool	2.2 min	0.98	22.55	93.38 %
Brain Surface Extractor	6.1 min	0.922	77.1	69.29 %
3dIntracranial	1.3 min	0.907	58.37	92.44 %
Graph based without postprocessing	4.5 min	0.981	14.29	97.87 %
Graph based with postprocessing	7.2 min	0.989	10.2	99.56%

Table 1: Results of the quantitative evaluation of the automatic brain segmentation methods

A.2 Fuzzy-Based Vascular Structure Enhancement in Time-of-Flight MRA Images for Improved Segmentation

Nils D. Forkert, Alexander Schmidt-Richberg, Jens Fiehler, Till Illies, Dietmar Möller, Heinz Handels, Dennis Säring:
Fuzzy-based vascular structure enhancement in Time-of-Flight MRA images for improved segmentation
Methods of Information in Medicine, 50(1), 74-83, 2011.

A.3 3D Cerebrovascular Segmentation Combining Fuzzy Vessel Enhancement and Level-Sets with Anisotropic Energy Weights

Nils D. Forkert, Alexander Schmidt-Richberg, Jens Fiehler, Till Illies, Dietmar Möller, Dennis Säring, Heinz Handels, Jan Ehrhardt:
3D cerebrovascular segmentation combining fuzzy vessel enhancement and level-sets with anisotropic energy weights
Magnetic Resonance Imaging 31(2), 262-271, 2013.

A.4 Automatic Correction of Gaps in Cerebrovascular Segmentations Extracted from 3D Time-of-Flight MRA Datasets

Nils D. Forkert, Alexander Schmidt-Richberg, Jens Fiehler, Till Illies, Dietmar Möller, Heinz Handels, Dennis Säring:
Automatic correction of gaps in cerebrovascular segmentations extracted from 3D Time-of-Flight MRA datasets
Methods of Information in Medicine, 51(5), 415-422, 2012.

Appendix B

Cerebral Hemodynamics and Perfusion Analysis

B.1 Reference-Based Linear Curve Fitting for Bolus Arrival Time Estimation in 4D MRA and MR Perfusion-Weighted Image Sequences

Nils D. Forkert, Jens Fiehler, Thorsten Ries, Till Illies, Dietmar Möller, Heinz Handels, Dennis Säring:
Reference-based linear curve fitting for bolus arrival time estimation in 4D MRA and MR perfusion-weighted image sequences
Magnetic Resonance in Medicine, 65(1), 289-294, 2011.

B.2 Analysis of the Influence of 4D MR Angiography Temporal Resolution on Time-to-Peak Estimation Errors for Different Cerebral Vessel Structures

Nils D. Forkert, Till Illies, Dietmar Möller, Heinz Handels, Dennis Säring, Jens Fiehler:
Analysis of the influence of 4D MR angiography temporal resolution on time-to-peak estimation errors for different cerebral vessel structures
American Journal of Neuroradiology 33(11), 2103-2109, 2012.

Appendix C

4D Blood Flow Visualization

C.1 4D Blood Flow Visualization Fusing 3D and 4D MRA Image Sequences

Nils D. Forkert, Jens Fiehler, Till Illies, Dietmar Möller, Heinz Handels, Dennis Säring:
4D blood flow visualization fusing 3D and 4D MRA image sequences
Journal of Magnetic Resonance Imaging 36(2), 443–453, 2012.

C.2 Classification of Cerebral Arteriovenous Malformations and Intranidal Flow Patterns by Color-Encoded 4D-Hybrid-MRA

Till Illies, Nils D. Forkert, Thorsten Ries, Jan Regelsberger, Jens Fiehler:
Classification of cerebral arteriovenous malformations and intranidal flow patterns by color-encoded 4D-hybrid-MRA
American Journal of Neuroradiology 43(1), 46-53, 2013.

Appendix D

Model-based Analysis of Arteriovenous Malformations

D.1 Intranidal Signal Distribution in Post-Contrast Time-of-Flight MRA is Associated with Rupture Risk Factors in Arteriovenous Malformations

Nils D. Forkert, Jens Fiehler, Michael Schönfeld, Jan Sedlacik, Jan Regelsberger, Heinz Handels, Till Illies:
Intranidal signal distribution in post-contrast Time-of-Flight MRA is associated with rupture risk factors in arteriovenous malformations
Clinical Neuroradiology, 23(2), 97-101, 2013.

D.2 Persistent Hemodynamic Changes in Ruptured Brain Arteriovenous Malformations

Till Illies, Nils D. Forkert, Dennis Säring, Karolin Wenzel, Thorsten Ries, Jan Regelsberger, Karl Wegscheider, Jens Fiehler:
Persistent hemodynamic changes in ruptured brain arteriovenous malformations
Stroke, 43(11), 2910-2915, 2012.

D.3 Territorial and Microvascular Perfusion Impairment in Brain Arteriovenous Malformations

Jens Fiehler, Till Illies, Merle Piening, Dennis Säring, Nils D. Forkert, Jan Regelsberger, Ulrich Grzyska, Heinz Handels, James V. Byrne:
Territorial and microvascular perfusion impairment in brain arteriovenous malformations
American Journal of Neuroradiology, 30(2), 356-361, 2009.

D.4 Computer-Aided Nidus Segmentation and Angiographic Characterization of Arteriovenous Malformations

Nils D. Forkert, Till Illies, Einar Goebell, Jens Fiehler, Dennis Säring, Heinz Handels:
Computer-aided nidus segmentation and angiographic characterization of arteriovenous malformations
International Journal for Computer Assisted Radiology and Surgery, 2013
[Epub ahead of print].

Appendix E

Model-based Analysis of Aneurysms

E.1 Comparison of 3D Computer-Aided with Manual Cerebral Aneurysm Measurements in Different Imaging Modalities

Michael Groth, Nils D. Forkert, Jen-Hendrik Buhk, Michael Schönfeld, Einar Goebell, Jens Fiehler:
Comparison of 3D computer-aided with manual cerebral aneurysm measurements in different imaging modalities
Neuroradiology 55(2), 171-178, 2013.

E.2 Rigid 3D-3D Registration of TOF MRA Integrating Vessel Segmentation for Quantification of Recurrence Volumes after Coiling Cerebral Aneurysm

Dennis Säring, Jens Fiehler, Thorsten Ries, Nils D. Forkert:
Rigid 3D-3D registration of TOF MRA integrating vessel segmentation for quantification of recurrence volumes after coiling cerebral aneurysm
Neuroradiology 54(2), 171-176, 2012.

E.3 Quantification of Recurrence Volumes after Endovascular Treatment of Cerebral Aneurysm as Surrogate Endpoint for Treatment Stability

Thorsten Ries, Karl Wegscheider, Asmus Wulff, Kristin Radelfahr, Dennis Säring, Nils D. Forkert, Jens Fiehler:
Quantification of recurrence volumes after endovascular treatment of cerebral aneurysm as surrogate endpoint for treatment stability
Neuroradiology 53(8), 593-598, 2011.

Appendix F

Model-based Analysis of Ischemic Strokes

F.1 Comparison of Ten TTP and Tmax Estimation Techniques for MR Perfusion-Diffusion Mismatch Quantification

Nils D. Forkert, Philipp Kaesemann, András Treszl, Susanne Siemonsen, Bastian Cheng, Heinz Handels, Jens Fiehler, Götz Thomalla:
Comparison of ten TTP and Tmax estimation techniques for MR perfusion-diffusion mismatch quantification
American Journal of Neuroradiology, 2013 [Epub ahead of print]

F.2 DWI-FLAIR Mismatch for the Identification of Patients with Acute Ischaemic Stroke Within 4.5 h of Symptom Onset (PRE-FLAIR): A Multicentre Observational Study

Götz Thomalla, Bastian Cheng, Martin Ebinger, Qing Hao, Thomas Tourdias, Ona Wu, Jong S. Kim, Lorenz Breuer, Oliver C. Singer, Stephen Warach, Soren Christensen, András Treszl, Nils D. Forkert, Ivana Galinovic, Michael Rosenkranz, Tobias Engelhorn, Martin Köhrmann, Matthias Endres, Dong-Wa Kang, Vincent Dousset, A. Gregory Sorensen, David S. Liebeskind, Jochen B. Fiebach, Jens Fiehler, Christian Gerloff:
DWI-FLAIR mismatch for the identification of patients with acute ischaemic stroke within 4.5 h of symptom onset (PRE-FLAIR): A multicentre observational study
The Lancet Neurology 10(11), 978-986, 2011.

F.3 Quantitative Measurements of Relative Fluid-Attenuated Inversion Recovery (FLAIR) Signal Intensities in Acute Stroke for the Prediction of Time from Symptom Onset

Bastian Cheng, Mathias Brinkmann, Nils D. Forkert, András Treszl, Martin Ebinger, Martin Köhrmann, Ona Wu, Dong-Wha Kang, David S. Liebeskind, Thomas Tourdias, Oliver C. Singer, Soren Christensen, Marie Luby, Steven Warach, Jens Fiehler, Jochen B. Fiebach, Christian Gerloff, Götz Thomalla:

Quantitative measurements of relative fluid-attenuated inversion recovery (FLAIR) signal intensities in acute stroke for the prediction of time from symptom onset

Journal of Cerebral Blood Flow and Metabolism, 33(1), 76-84, 2013.

F.4 The Extent of Perfusion Deficit Does not Relate to the Visibility of Acute Ischemic Lesions on Fluid-Attenuated Inversion Recovery Imaging

Bastian Cheng, Michael Rosenkranz, Anna Krützelmann, Jens Fiehler, Nils D. Forkert, Christian Gerloff, Götz Thomalla:
The extent of perfusion deficit does not relate to the visibility of acute ischemic lesions on fluid-attenuated inversion recovery imaging
Journal of Neuroimaging 23(2), 215-218, 2013.

F.5 Elevated T2-Values in MRI of Stroke Patients Shortly after Symptom Onset do not Predict Irreversible Tissue infarction

Susanne Siemonsen, Ulrike Löbel, Jan Sedlacik, Nils D. Forkert, Kim Mouridsen, Leif Østergaard, Götz Thomalla, Jens Fiehler:
Elevated T2-values in MRI of stroke patients shortly after symptom onset do not predict irreversible tissue infarction
Brain 135(6), 1981-1989, 2012.